

## BIROn - Birkbeck Institutional Research Online

Wildman, M.R. and Brown, R. and Beucher, R. and Persano, C. and Stuart, F. and Gallagher, K. and Schwanethal, J. and Carter, Andrew (2016) The chronology and tectonic style of landscape evolution along the elevated Atlantic continental margin of South Africa resolved by joint apatite fission track and (U-Th-Sm)/He thermochronology. *Tectonics* 35 , ISSN 0278-7407.

Downloaded from: <https://eprints.bbk.ac.uk/id/eprint/14772/>

*Usage Guidelines:*

Please refer to usage guidelines at <https://eprints.bbk.ac.uk/policies.html>  
contact [lib-eprints@bbk.ac.uk](mailto:lib-eprints@bbk.ac.uk).

or alternatively

## RESEARCH ARTICLE

10.1002/2015TC004042

## Key Points:

- First joint apatite fission track and (U-Th)/He data for the southwest African continental margin
- Present-day topography due to kilometer-scale erosion that occurred during the Cretaceous
- Faulting onshore as well as regional uplift of the margin inferred during the Middle to Late Cretaceous

## Supporting Information:

- Texts S1–S9 and captions for Figures S2, S3, S5–S7, Table S8, and Data Set S9
- Figure S2
- Figure S3
- Figure S5a
- Figure S5b
- Figure S6
- Figure S7a
- Figure S7b
- Figure S7c
- Table S8
- Data Set S9
- Supporting information S1

## Correspondence to:

M. Wildman,  
markwildman88@hotmail.com

## Citation:

Wildman, M., R. Brown, R. Beucher, C. Persano, F. Stuart, K. Gallagher, J. Schwanethal, and A. Carter (2016), The chronology and tectonic style of landscape evolution along the elevated Atlantic continental margin of South Africa resolved by joint apatite fission track and (U-Th-Sm)/He thermochronology, *Tectonics*, 35, doi:10.1002/2015TC004042.

Received 1 OCT 2015

Accepted 7 FEB 2016

Accepted article online 10 FEB 2016

# The chronology and tectonic style of landscape evolution along the elevated Atlantic continental margin of South Africa resolved by joint apatite fission track and (U-Th-Sm)/He thermochronology

Mark Wildman<sup>1</sup>, Roderick Brown<sup>1</sup>, Romain Beucher<sup>1,2</sup>, Cristina Persano<sup>1</sup>, Fin Stuart<sup>3</sup>, Kerry Gallagher<sup>4</sup>, James Schwanethal<sup>5</sup>, and Andrew Carter<sup>6</sup>

<sup>1</sup>School of Geographical and Earth Sciences, College of Science and Engineering, University of Glasgow, Glasgow, Scotland,

<sup>2</sup>Now at Department of Earth Science, Faculty of Mathematics and Natural Sciences, University of Bergen, Bergen, Norway,

<sup>3</sup>Scottish Universities Environmental Research Centre, East Kilbride, UK, <sup>4</sup>Géosciences Rennes, Université de Rennes 1,

Campus de Beaulieu, Rennes, France, <sup>5</sup>Department of Earth Sciences, University College London, London, UK, <sup>6</sup>Department

of Earth and Planetary Sciences, Birkbeck, University of London, London, UK

**Abstract** Atlantic-type continental margins have long been considered “passive” tectonic settings throughout the entire postrift phase. Recent studies question the long-term stability of these margins and have shown that postrift uplift and reactivation of preexisting structures may be a common feature of a continental margin’s evolution. The Namaqualand sector of the western continental margin of South Africa is characterized by a ubiquitously faulted basement but lacks preservation of younger geological strata to constrain postrift tectonic fault activity. Here we present the first systematic study using joint apatite fission track and apatite (U-Th-Sm)/He thermochronology to achieve a better understanding on the chronology and tectonic style of landscape evolution across this region. Apatite fission track ages range from  $58.3 \pm 2.6$  to  $132.2 \pm 3.6$  Ma, with mean track lengths between  $10.9 \pm 0.19$  and  $14.35 \pm 0.22$   $\mu\text{m}$ , and mean (U-Th-Sm)/He sample ages range from  $55.8 \pm 31.3$  to  $120.6 \pm 31.4$  Ma. Joint inverse modeling of these data reveals two distinct episodes of cooling at approximately 150–130 Ma and 110–90 Ma with limited cooling during the Cenozoic. Estimates of denudation based on these thermal histories predict approximately 1–3 km of denudation coinciding with two major tectonic events. The first event, during the Early Cretaceous, was driven by continental rifting and the development and removal of synrift topography. The second event, during the Late Cretaceous, includes localized reactivation of basement structures as well as regional mantle-driven uplift. Relative tectonic stability prevailed during the Cenozoic, and regional denudation over this time is constrained to be less than 1 km.

## 1. Introduction

Passive continental margins, as the term explicitly implies, have been characterized by an apparent tectonic stability following their formation by intracontinental rifting and breakup [Braun and Beaumont, 1989; Lister et al., 1991; Ziegler and Cloetingh, 2004]. However, a growing body of work is questioning this view and providing better insight into the thermal and structural processes that operate during rifting and influence the long-term geomorphic development of extensional continental margins and their interior hinterlands [Péron-Pinvidic and Manatschal, 2009; Bronner et al., 2011; Paton, 2012; Dauteuil et al., 2013; Masini et al., 2013; Karl et al., 2013; Péron-Pinvidic et al., 2013; Brune et al., 2014; Huisman and Beaumont, 2014; Koopmann et al., 2014; Salomon et al., 2014].

Plate reconstructions have primarily focused on in-plane restorations of large plate blocks and have used overlaps and gaps in plate reconstructions as evidence for extensional and compressional deformation of the lithosphere, respectively [Eagles and König, 2008; Aslanian et al., 2009; Torsvik et al., 2009; Moulin et al., 2010; Aslanian and Moulin, 2013; Gaina et al., 2013; Heine et al., 2013; Pérez-Díaz and Eagles, 2014]. The nature of this lithospheric deformation has been explored by numerical modeling approaches that have revealed complex styles of rifted margin development, involving rift migration [Brune et al., 2014; Naliboff and Buiter, 2015], hyperextension [Lundin and Doré, 2011; Péron-Pinvidic et al., 2013; Redfield and Osmundsen, 2013], and/or multiphase rifting [Reston, 2005; Blaich et al., 2011; Huisman and Beaumont, 2014]. These models have predicted different styles and mechanisms for intracontinental deformation [Pérez-Gussinyé et al., 2007; Cloetingh and Burov, 2011; Kennett and Iaffaldano, 2013; Calignano et al., 2015].

Alongside geodynamical modeling of rifted margin evolution, but treated independently, a growing body of work has investigated regional and local vertical motions of the Earth's crust as a result of "dynamic" uplift or subsidence stemming from vertical stresses imposed on the base of the lithosphere by convection of the underlying mantle [Moucha *et al.*, 2008; Braun, 2010; Forte *et al.*, 2010; Flament *et al.*, 2014]. Recently, new thermomechanical modeling approaches have coupled the vertical forces acting on the base of the lithosphere, in-plane stresses from plate movements, and the deformational response of a rheologically and structurally heterogeneous lithosphere over different length scales [Guillou-Frotier *et al.*, 2012; Cloetingh *et al.*, 2013; Buiter and Torsvik, 2014; Burov and Gerya, 2014; Colli *et al.*, 2014; Koptev *et al.*, 2015]. A fundamental outcome of these modeling approaches is that plate motions, mantle flow, and vertical motions of the surface are all intrinsically linked [François *et al.*, 2013; Colli *et al.*, 2014].

Tectonic uplift, as a consequence of deformation of the lithosphere, will trigger a response in surface processes [Willett, 1999; Burbank and Anderson, 2012]. Therefore, new models of how the crust responds to intra-continental rifting and deep Earth processes will have implications for the origin and longevity of topography at high-elevation passive continental margins. This issue is particularly pertinent for the South African case, where the antiquity of the present-day first-order topography is still ardently debated. One end-member scenario argues that the South African landscape is "young," having been formed by major river incision and erosion of a flat initial topography in response to regional epeirogenic uplift during the late Cenozoic [e.g., Partridge and Maud, 1987; Burke, 1996; Burke and Gunnell, 2008; Roberts and White, 2010; Paul *et al.*, 2014; Rudge *et al.*, 2015]. Contrary to this, another end-member scenario proposes that the present-day landscape is an "old" remnant of Cretaceous topography that was produced by deep erosion of uplifted rift flanks following continental breakup, with minimal erosion during the Cenozoic [Gallagher and Brown, 1999; Bierman and Caffee, 2001; Brown *et al.*, 2002; van der Beek *et al.*, 2002; Decker *et al.*, 2013]. However, several thermochronometry studies have argued for a more eventful postrift history involving tectonic reactivation in the middle-Late Cretaceous [Raab *et al.*, 2002; Tinker *et al.*, 2008a; Kounov *et al.*, 2009; Brown *et al.*, 2014; Wildman *et al.*, 2015] or multiple phases of regional uplift/exhumation and subsidence/burial [e.g., Green *et al.*, 2013, 2015].

Due to a lack of postrift geological markers and poor age constraints on the timing of deformation on major structures, the tectonic history of the southwest African continental margin is incomplete. Recent investigations have alluded to the potential importance of postrift structural reactivation and neotectonic activity to the development of the South African margin [Viola *et al.*, 2005, 2012; Brandt *et al.*, 2003, 2005; Andreoli *et al.*, 1996, 2009; de Beer, 2012; Kounov *et al.*, 2009; Wildman *et al.*, 2015], and postrift reactivation has been advocated by investigations of other so-called "passive" continental margins [Redfield *et al.*, 2005; Cogné *et al.*, 2011; Holford *et al.*, 2014; Franco-Magalhaes *et al.*, 2014; Ksienzyk *et al.*, 2014; Leprière *et al.*, 2015]. Constraining the surface response to postrift deformation over different length scales will have major implications for conceptual geomorphic models of high-elevation continental margins that envisage regional patterns of denudation triggered by regional base level fall and augmented by long-wavelength epeirogenic/flexural uplift.

In this paper we report new quantitative constraints on the timing and magnitude of major episodes of denudation across the continental margin obtained from a dense array of joint apatite fission track (AFT) and apatite (U-Th-Sm)/He (AHe) low-temperature thermochronometry samples. The sampling strategy was to collect samples from the coastline to the elevated continental interior with high-density sampling through the high-relief escarpment zone referred to as the Namaqualand Highlands (Figure 1). Samples from the Namaqualand Highlands were collected with a specific focus on constraining brittle offsets on basement structures. This approach was employed to detect short and long-wavelength patterns of crustal cooling. By using combined AFT and AHe thermochronometry, we achieve tighter thermal history constraints than has previously been obtained by studies using either system in isolation. In particular, including AHe data helps constrain cooling in the very shallow crust (approximately 1–2 km), which has hitherto been left poorly constrained by AFT analysis. Robust thermal histories were obtained by jointly inverting the analytical data using a Bayesian transdimensional Markov Chain Monte Carlo (MCMC) approach described by Gallagher [2012]. We demonstrate that these cooling episodes relate to crustal denudation and a multistage development of the continental margin is proposed that requires significant (kilometer-scale) differential displacement on onshore brittle structures well inland (hundreds of kilometers) of the present coastline.

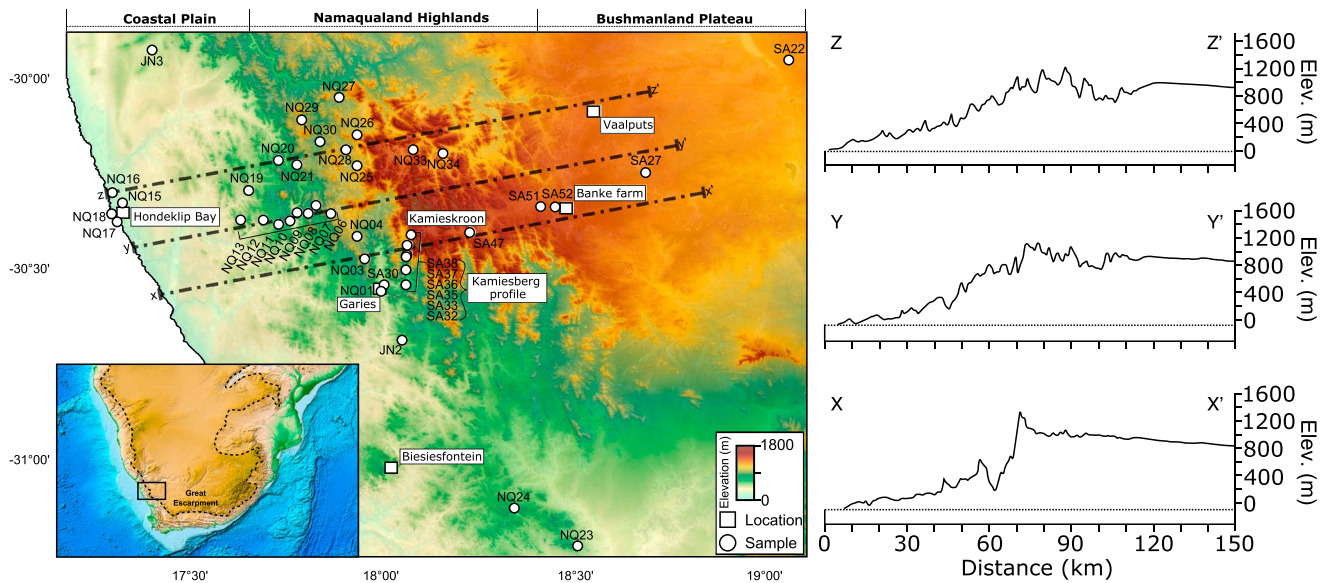


**Figure 1.** Inset figure shows the first-order topography of Southern Africa and location of the Namaqualand Highlands study area. Main location map digital elevation model created using SRTM90m data. Elevation map is draped over Landsat ETM+RGB:321 satellite images to enhance local relief and geomorphic features. Elevation profiles for three coast-perpendicular transects are shown and are used in Figure 9 with projected data.

## 2. Geology

### 2.1. Tectonic Setting of the Namaqualand Basement Rocks

Rocks of the Mesoproterozoic Namaqua Metamorphic Province dominate the geology of the study area (Figure 2). These basement rocks are composed mainly of granitic gneisses and granite bodies emplaced during multiple periods of orogeny and terrane accumulation [Tankard *et al.*, 1982; Groenewald *et al.*, 1991; Jacobs *et al.*, 1993; Cornell *et al.*, 2006]. The Namaqua Metamorphic Province therefore records a complicated history of magma emplacement and metamorphism that has produced a variety of supracrustal and intrusive rock types [Thomas *et al.*, 1994; Eglington, 2006; Voordouw and Rajesh, 2012]. A detailed description of these rock types can be found in Eglington [2006].

What is more pertinent in the context of this study is the tectonic fabric that was established at this time, as this basement structure may have been important in controlling the style of prerift, synrift, and postrift deformation [e.g., Daly *et al.*, 1989; Clemson *et al.*, 1997; Ziegler and Cloetingh, 2004; Corti *et al.*, 2007; Frimmel *et al.*, 2013]. At least four compressional deformation events have been documented in gneissic foliations and folds and are thought to have been driven by processes coeval with the regional Kibaran Orogeny (approximately 1200–1000 Ma) and global Grenville Orogeny (approximately 1300–950 Ma) [Jacobs *et al.*, 1993; Clifford *et al.*, 2004; Eglington, 2006; Viola *et al.*, 2012; Colliston *et al.*, 2014]. These deformation events were followed by a phase of extension in western Namaqualand that has been attributed to the collapse of the Namaqualand orogenic belt [Dewey *et al.*, 2006]. Dykes, folds, and lineations ascribed to these deformation events typically strike NW-SE or NE-SW and occasionally E-W [Cornell *et al.*, 2006]. The main phase of metamorphism of the Namaqua Metamorphic Province was largely granulite facies metamorphism ( $T$ : 800–860°C and  $P$ : 5–6 kbar/15–18 km) and was completed by 1000–800 Ma [Waters, 1989; Eglington, 2006].

The Vanrhynsdorp Group unconformably overlies the metamorphic basement and was deposited during the latter stages of the Pan-African orogeny (approximately 700–500 Ma) in a foreland basin setting and subsequently experienced very low grade metamorphism [Grasse and Germs, 1993]. These rocks crop out in the south of the study area, close to the town of Bitterfontein, in half-graben structures trending N-S as gently folded, fault parallel synclines that overlie an easterly dipping unconformity across the basement rocks [Grasse *et al.*, 2006; Macey *et al.*, 2011] (Figure 2). The influence of the Pan-African Orogeny is observed in the Namaqua Metamorphic Province as brittle overprint structures [Viola *et al.*, 2012]. Cambrian to Early Carboniferous rocks of the Cape Supergroup only crop out in the very southeastern part of our study area and overlie the



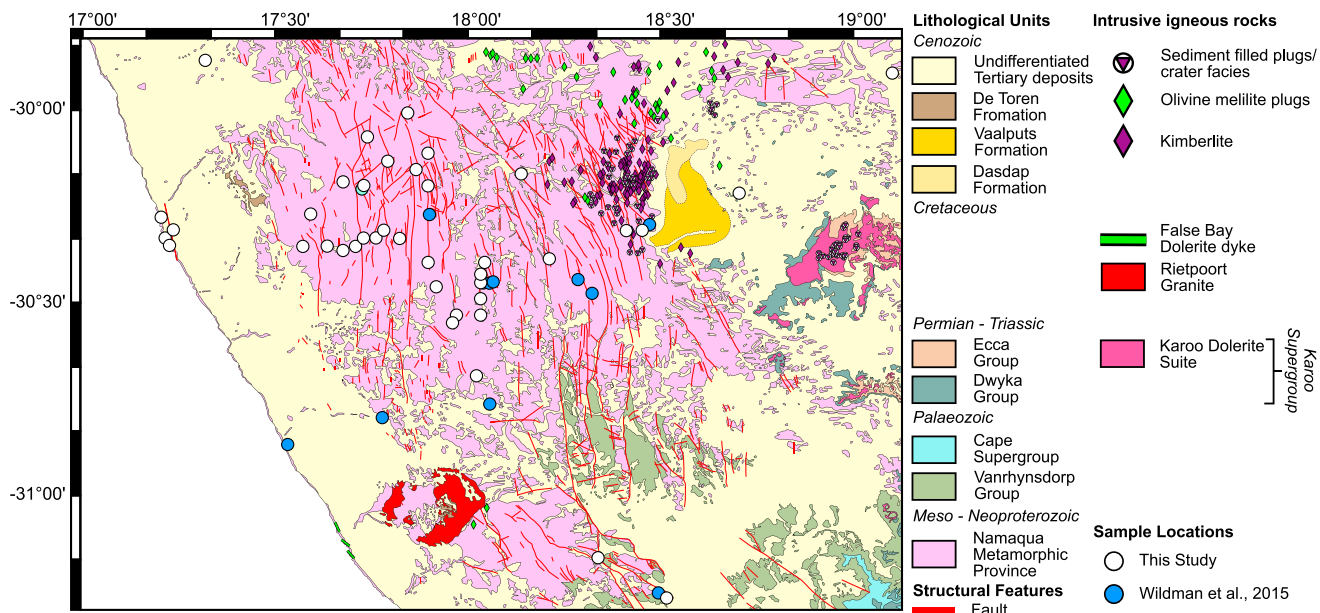


**Figure 2.** Geological map of the Namaqualand Highlands study area. Geological map was redrawn to highlight the major geological units, structures, and features relevant to this study, using 1:250,000 maps produced by the Council for Geoscience, South Africa. (Garies, sheet 3017 [de Beer, 2010]; Loriesfontein, sheet 3018 [Macey et al., 2011]; and Springbok, sheet 2916 [Marais et al., 2001].) The dashed line around the Dasdap and Vaalputs formations represents the proposed extent of these units [after Brandt et al., 2005; de Beer, 2010].

Vanrhynsdorp Group. The Cape Supergroup, which dominates the geology south of our study area, was deformed during Permian to Triassic compression to form the Cape Fold Belt [Newton et al., 2009].

## 2.2. The Karoo Supergroup

The sedimentary rocks of the Karoo Supergroup were deposited in a subcontinental foreland basin, north of the developing Cape Fold Belt, during the Carboniferous to Triassic period [Tankard et al., 2009]. The Karoo basin covers an area of approximately  $7 \times 10^5 \text{ km}^2$  across central South Africa (Figure 2). The Karoo Supergroup rocks that crop out within the study area include the lowermost Permian Dwyka Group and Ecce Group rocks [Johnson et al., 2006], which are intruded by Triassic-Jurassic Karoo dolerite sills and dykes. Dwyka glacial diamictites were unconformably deposited on the metamorphic basement and Vanrhynsdorp units during Late Carboniferous to Early Permian glaciations [Visser, 1990]. The thickness and lithofacies of the Dwyka Group are highly variable and are attributed to erosion of an irregular pre-Karoo relief [Visser, 1983, 1987, 1989; Johnson et al., 2006]. Conformably overlying the Dwyka Group glacial deposits is the Permian Ecce Group, consisting of shale units that are thinly laminated and fossiliferous [Johnson et al., 2006]. These rocks were deposited in a shallow-marine environment and are the dominant sedimentary unit in the northwest Karoo basin. The presence of Karoo Supergroup sedimentary rocks is important as they represent the last time the South African interior was unequivocally below sea level [Summerfield, 1985]. The intrusion of Karoo dolerite sills and dykes was coeval with the eruption of thick continental flood basalts ( $>1.5\text{--}2 \text{ km}$ ) and marks the termination of Karoo deposition and the onset of continental rifting in eastern Gondwana (approximately  $180 \pm 5 \text{ Ma}$ ) [Duncan et al., 1997; Jourdan et al., 2005, 2007; Moulin et al., 2011; Svensen et al., 2012]. Karoo dolerite intrusions are widely preserved in the eastern part of the study area as prominent isolated summits above the flat-lying plateau.

## 2.3. Synrift and Postrift Intrusive Activity

Post-Karoo igneous rocks, coeval with Atlantic rifting (approximately 160–130 Ma), can be found in the most southern region of the study area (Figure 2). The Koegel Fontein complex near the towns of Kotzesrus and Biesiesfontein is composed of a variety of intrusive bodies including tholeiitic basalt plugs, syenite and granite plutons, and dykes of varying composition [de Beer, 2002; Curtis et al., 2011]. A suite of NNW-SSE trending dolerite dykes crosscut the Koegel Fontein complex and is believed to have the same origin as the False Bay dolerite suite in the Southern Cape based on their age and composition [Day, 1987; Reid, 1990; Reid et al., 1991; Trumbull et al., 2007; de Beer, 2010].

Early Cenozoic intrusions are commonly olivine melilitite plugs and alkali and carbonatite dykes. The Biesiesfontein plugs intrude into the Rietpoort Granite and have been dated at approximately 55 Ma [Moore and Verwoerd, 1985]. The Sandkopsdrif Complex north of Rietpoort is made up of numerous alkaline and carbonatite dykes [de Beer, 2010; Curtis *et al.*, 2013] and is thought to postdate olivine melilitites in Biesiesfontein [Moore and Verwoerd, 1985]. An important observation that can be made from these intrusions is their coherent trend along a north to NNW striking fracture zone, suggesting a link between reactivation of major structures during the Early Cretaceous and the early Cenozoic creating pathways for intrusive rock [e.g., Moore *et al.*, 2008; Jelsma *et al.*, 2009].

The Gamoep intrusive suite (Figure 2), consisting of olivine melilitite plugs and possible kimberlite intrusions, is found inland on the interior plateau north of Banke Farm close to the Vaalputs nuclear repository site. The intrusions have been radiometrically dated at 54–77 Ma [Moore and Verwoerd, 1985], while terrestrial fossil and palynological evidence discovered in the sediment infill confirm a Late Cretaceous to Eocene age for these intrusions [Haughton, 1931; Estes, 1977; Scholtz, 1985; de Wit *et al.*, 1992].

#### 2.4. Late Cretaceous and Tertiary Deposits

The preservation of crater lake sedimentary successions over intrusive bodies is highly significant as they provide insights into the margin's postrift geological history, a record of which is otherwise absent. Up to 260 m of carbonaceous shales and tuff bands, commonly topped with conglomerates and arenites, are preserved within the diatremes of Late Cretaceous to early Cenozoic intrusions [Moore and Verwoerd, 1985]. These sediments are interpreted as lacustrine deposits and imply that limited erosion has taken place since the emplacement of the igneous intrusive rocks [Cornelissen and Verwoerd, 1975; Moore and Verwoerd, 1985; Hanson *et al.*, 2009; Stanley *et al.*, 2013]. Additional postrift sedimentary units include silicified kaolinized conglomerates and coarse-grained, cross-bedded sandstones of the Dasdap and Vaalputs formation, which form prominent mesas on the plateau near Banke Farm, south of Vaalputs [Brandt *et al.*, 2003, 2005] (Figure 2). Clast compositions within the conglomerate horizons and the occurrence of widespread cross laminations in the Dasdap sediments suggest that these sediments were deposited in a fluvial environment and derived from the surrounding basement and Dwyka Group rocks [Brandt *et al.*, 2003, 2005]. The volcanic pipes in the region discussed above are overlain by these units in places and therefore provide an upper age limit of approximately 67 Ma for the Dasdap sequence [Brandt *et al.*, 2003, 2005; Viola *et al.*, 2012].

The Vaalputs formation and adjacent Santab-se-Vloer Basin overlie the Dasdap sequence and are intersected and bounded by prominent NNW-SSW trending faults. The orientation of these structures is in keeping with the regional NNW-SSE structural trend [Viola *et al.*, 2012]. Although these sediments are severely lacking in age constraints, their similarity to nearby crater lake deposits and their relationship with Late Cretaceous igneous intrusions suggest that a Late Cretaceous-early Cenozoic age is possible.

Cenozoic deposits along the coastal plain are typically preserved in the form of elevated marine terraces, semi-consolidated and unconsolidated aeolian sand, and as channel fill sediments preserved in valleys within the high-relief escarpment zone. The coastal marine terraces are best represented by the Alexander Bay Formation, which records Miocene and younger cycles of erosion and weathering attributed to sea level fluctuations driven by both tectonic and eustatic processes [Roberts *et al.*, 2006]. Three distinct packages have been defined within the Alexander Bay Formation at 90 m, 50 m, and 30 m above sea level. The de Toren Formation is present on the Koegel Fontein intrusive complex and on the periphery of the Namaqualand Highlands at Quaggafontein farm. The sediments are proposed to have been deposited in a similar environment to the Dasdap Formation and have a similarly uncertain age, which is tentatively placed in the Oligocene by de Beer [2010, 2012].

### 3. Apatite Fission Track and (U-Th-Sm)/He Analysis

#### 3.1. Apatite Fission Track Results

Apatite fission track analysis was performed on all 42 samples using the external detector method [Hurford and Green, 1982] (Table 1 and Text S1 in the supporting information). Central AFT ages range from  $58.3 \pm 2.6$  to  $132.2 \pm 3.6$  Ma and do not show a correlation with elevation. Indeed, some of the youngest measured AFT ages can be found at the highest elevations (Figure 3a). Mean horizontal confined track lengths (MTLs) range from  $10.9 \pm 0.19$  to  $14.35 \pm 0.22$   $\mu\text{m}$  with the majority being greater than 13  $\mu\text{m}$ ; the standard deviation of length measurements ranges from 0.97 to 2.50. In cases where MTLs are relatively short or length distributions are relatively broad, the shape of the distribution is either normal around the mean value or is

**Table 1.** Results of Apatite Fission Track Analysis<sup>a</sup>

Table 1. Results of Apatite Fission Track Analysis <sup>a</sup>																											
Sample	Longitude (deg)	Latitude (deg)	Elevation (m)	$\rho_s^b$ ( $10^6 \text{ cm}^{-2}$ )	$\rho_i^b$ ( $10^6 \text{ cm}^{-2}$ )		$N_s^c$ ( $10^6 \text{ cm}^{-2}$ )	$N_i^c$ ( $10^6 \text{ cm}^{-2}$ )	$\rho_d^b$ ( $10^6 \text{ cm}^{-2}$ )	$N_d^c$	$P_V^{2,d}$	$D_{par}^e$ ( $\mu\text{m}$ )	$[U]_{AFT}^f$ (ppm)	Central AFT Age <sup>g</sup> $\pm 1\sigma$ (Ma)		Dispersion <sup>h</sup> (%)	Measured			c Axis Correction <sup>j</sup>			#HCT <sup>k</sup>				
					$\rho_i^b$	$\rho_s^b$								#Xtals	MTL ( $\mu\text{m}$ )		$\pm 1\sigma$	SD <sup>j</sup>	MTL ( $\mu\text{m}$ )	$\pm 1\sigma$	SD <sup>j</sup>						
JN2	18.05	-30.68	376	42.7	3.605	100.2	8.451	19.8	14.137	0.01	2.13	67.6	132.2	3.6	13%	20	13.73	0.11	1.08	14.74	0.12	0.79	103				
JN3	17.38	-29.90	418	24.2	1.790	64.7	4.796	19.9	14.137	0.81	1.91	44.1	116.8	3.2	10%	20	13.62	0.11	1.10	14.72	0.12	0.78	103				
NQ12-01	17.99	-30.55	238	15.0	1.365	40.4	3.675	14.6	16.086	0.04	1.49	37.6	85.4	3.4	19%	20	13.39	0.13	1.32	14.65	0.14	0.80	100				
NQ12-03	17.95	-30.46	582	11.1	1.163	29.8	3.127	14.7	16.086	0.57	1.83	27.0	86.0	3.0	17%	20	14.01	0.11	1.10	15.03	0.12	0.76	101				
NQ12-04	17.93	-30.40	720	7.2	1.324	21.2	3.898	16.6	16.348	0.00	1.65	27.8	89.6	4.1	20%	19	13.85	0.10	0.98	14.95	0.11	0.63	100				
NQ12-06	17.86	-30.34	690	26.7	2.080	76.9	5.989	16.5	16.348	0.32	1.62	65.3	90.2	2.4	12%	19	12.50	0.13	1.39	13.73	0.14	1.04	115				
NQ12-07	17.82	-30.32	688	29.6	2.511	72.0	6.095	14.8	16.086	0.12	1.92	65.0	96.0	2.6	14%	20	13.63	0.10	1.23	14.74	0.11	0.82	151				
NQ12-08	17.80	-30.34	598	23.1	2.283	60.9	6.012	16.5	16.348	0.06	2.98	49.5	98.7	3.0	14%	19	13.96	0.13	1.23	14.95	0.14	0.90	73				
NQ12-09	17.77	-30.34	355	12.6	1.153	31.8	2.906	17.1	16.086	0.49	2.49	25.8	106.6	3.8	15%	20	13.60	0.19	1.92	14.74	0.21	1.20	101				
NQ12-10	17.75	-30.36	239	5.9	2.08	19.2	6.78	16.5	16.348	0.50	3.42	16.3	79.7	6.3	25%	9	14.35	0.22	1.05	15.18	0.23	0.83	22				
NQ12-11	17.72	-30.37	416	4.6	4.77	11.2	1.167	17.2	16.086	0.82	2.07	10.1	110.4	6.0	23%	20	13.51	0.16	1.43	14.64	0.17	0.90	38				
NQ12-12	17.68	-30.36	388	31.2	1.649	96.3	5.096	16.5	16.348	0.10	2.89	83.4	83.7	2.7	16%	18	13.45	0.15	1.50	14.67	0.16	0.97	106				
NQ12-13	17.62	-30.36	354	7.8	7.47	21.8	2.082	14.9	16.086	0.28	1.45	19.3	84.0	4.1	20%	20	13.59	0.13	1.27	14.77	0.14	0.91	100				
NQ12-15	17.30	-30.32	38	4.5	3.73	11.7	9.66	15.0	16.086	0.17	2.06	10.8	91.5	6.3	35%	20	14.05	0.15	1.45	15.10	0.16	0.91	94				
NQ12-16	17.27	-30.29	11	8.5	6.43	22.0	1.654	15.2	16.086	0.01	1.87	19.5	93.5	6.1	34%	20	13.70	0.15	1.22	14.80	0.16	0.83	65				
NQ12-17	17.29	-30.36	5	8.6	9.14	21.7	2.316	16.8	16.086	0.14	1.82	17.5	104.9	4.6	23%	20	13.02	0.19	1.91	14.07	0.21	1.33	100				
NQ12-18	17.28	-30.34	5	8.9	1.161	21.8	2.846	16.9	16.086	0.02	2.11	16.6	108.4	4.9	23%	20	13.88	0.19	1.30	14.92	0.20	0.88	100				
NQ12-19	17.64	-30.28	250	5.2	7.54	11.8	1.723	15.4	16.086	0.64	1.90	10.8	105.8	4.6	22%	20	13.40	0.19	1.48	14.55	0.20	1.06	82				
NQ12-20	17.72	-30.20	473	22.3	1.556	53.5	3.723	15.6	16.086	0.18	2.28	45.3	102.5	3.6	15%	19	13.77	0.12	1.28	14.82	0.13	0.87	108				
NQ12-21	17.77	-30.21	665	24.6	1.468	80.9	4.831	17.3	16.086	0.00	1.82	54.6	83.2	4.0	23%	17	13.67	0.19	1.41	14.57	0.20	0.98	102				
NQ12-23	18.52	-31.23	300	9.0	7.79	40.3	3.474	16.5	16.348	0.18	1.56	32.0	58.3	2.6	29%	20	13.83	0.13	1.31	14.56	0.14	0.90	103				
NQ12-24	18.35	-31.13	400	20.8	1.164	58.3	3.259	16.5	16.348	0.93	2.27	46.8	92.7	3.2	12%	20	14.20	0.09	0.97	15.15	0.10	0.66	108				
NQ12-25	17.93	-30.21	740	7.1	7.72	15.6	1.700	15.8	16.086	0.64	2.46	14.3	112.6	4.9	19%	20	14.01	0.14	1.45	14.98	0.15	0.96	112				
NQ12-26	17.93	-30.13	850	37.4	2.822	90.4	6.823	16.5	16.348	0.17	2.43	79.7	107.2	2.7	12%	20	13.94	0.12	1.21	14.93	0.13	0.80	103				
NQ12-27	17.88	-30.03	600	18.5	2.167	44.5	5.213	16.2	16.086	0.43	1.91	38.0	105.8	2.7	15%	23	13.37	0.13	1.35	14.61	0.14	0.85	104				
NQ12-28	17.90	-30.17	650	35.6	2.282	95.2	6.107	17.4	16.086	0.35	2.15	76.0	102.1	2.5	12%	20	12.89	0.16	1.83	14.28	0.18	1.11	128				
NQ12-29	17.78	-30.09	720	28.7	5.86	74.8	1.527	16.5	16.348	0.17	2.20	61.6	99.1	5.6	17%	10	13.81	0.11	1.15	14.85	0.12	0.80	111				
NQ12-30	17.83	-30.15	550	31.6	2.426	74.9	5.758	16.4	16.348	0.40	1.75	58.2	108.5	2.6	12%	20	13.86	0.11	1.13	14.99	0.12	0.75	110				
NQ12-33	18.08	-30.17	1050	13.9	1.319	33.4	3.174	16.3	16.086	0.03	1.64	29.1	105.8	4.5	21%	20	13.56	0.14	1.40	14.76	0.15	0.97	100				
NQ12-34	18.16	-30.18	1000	15.0	9.49	34.8	2.203	16.3	16.438	0.05	1.93	30.6	110.0	5.3	22%	20	13.21	0.15	1.49	14.49	0.16	0.98	106				
SA12-22	19.08	-29.93	922	35.9	2.565	81.3	5.812	14.0	16.086	0.01	2.20	76.6	97.2	3.1	15%	20	14.04	0.14	1.48	15.07	0.15	0.97	108				
SA12-27	18.70	-30.23	987	5.6	3.34	24.1	1.434	16.6	16.348	0.71	1.84	22.4	60.9	3.7	27%	18	12.66	0.37	1.95	14.16	0.41	1.38	27				
SA12-30	18.00	-30.53	258	9.4	1.012	33.4	3.600	16.6	16.348	0.06	2.94	27.0	73.2	3.3	19%	20	14.17	0.22	1.20	15.10	0.23	0.80	100				
SA12-32	18.06	-30.53	351	6.0	1.06	20.4	3.36	16.2	16.348	0.85	1.70	18.6	75.1	8.3	8%	3	10.90	0.19	1.54	13.28	0.23	0.95	2				
SA12-33	18.06	-30.49	400	5.2	3.53	12.3	836	16.6	16.348	0.75	1.71	9.9	110.0	7.0	27%	23	13.48	0.28	1.33	14.63	0.30	0.95	23				
SA12-35	18.06	-30.45	605	3.4	2.32	6.5	442	14.1	16.086	0.62	1.87	6.1	119.0	10.0	43%	17	13.71	0.22	1.31	14.85	0.24	0.86	35				
SA12-36	18.06	-30.45	707	3.6	2.88	10.4	822	16.6	16.348	0.57	2.03	9.2	91.4	6.3	33%	21	13.90	0.17	1.58	14.98	0.18	0.93	82				

Table 1. (continued)

Sample	Longitude (deg)	Latitude (deg)	Elevation (m)	$\rho_s^b$ ( $10^6 \text{ cm}^{-2}$ )	$\rho_i^b$ ( $10^6 \text{ cm}^{-2}$ )		$N_i^c$ ( $10^6 \text{ cm}^{-2}$ )	$\rho_d^b$ ( $10^6 \text{ cm}^{-2}$ )	$N_d^c$ ( $10^6 \text{ cm}^{-2}$ )	$P\chi^2_d$	$D_{\text{par}}^e$ ( $\mu\text{m}$ )	$[U]^f$ (ppm)	Central AFT Age <sup>g</sup> $\pm 1\sigma$ (Ma)	Dispersion <sup>h</sup> (%)	#XtIs	Measured			c Axis Correction <sup>j</sup>			#HCT <sup>k</sup>																																																																																																																																																																																																																																																																																																																																																																																																																																																																																																																																																																																																																																																																																																																																																																																																																																																																																																																																																																																																																																																																																																																																																																																																																																																																																																																																																																																																										
																																																																																																																																																																																																																																																																																																																																																																																																																																																																																																																																																																																																																																																																																																																																																																																																																																																																																																																																																																																																																																																																																																																																																																																																																																																																																																																																																																																																																																</

<sup>a</sup>Analytical details can be found in SI-1 and SI-2. For details on sample lithology see SI-8.

<sup>b</sup> $\rho_i$  and  $\rho_d$  are track density of induced, spontaneous, dosimeter tracks.

<sup>c</sup> $N_i$ ,  $N_s$ , and  $N_d$  are the number of induced, spontaneous, and dosimeter tracks counted.

<sup>d</sup> $\chi^2$  value of the chi-square age homogeneity test [Galbraith, 2010].

<sup>e</sup> $D_{\text{par}}$  measurements are etch pit diameters used as a proxy for the influence of chemical composition on track annealing [Donelick et al., 2005]. Between three to five  $D_{\text{par}}$  measurements were measured for each dated single grain.

<sup>f</sup>Uranium content estimated using EDM.

<sup>g</sup>Central AFT ages calculated with TrackKey [Dunkl, 2002] with  $1\sigma$  standard error. Ages were calculated using a  $\zeta = 316.7 \pm 10.5$  (317.3  $\pm$  11.1 for samples JN2 and JN3) for a standard IRMM540 glass.

<sup>h</sup>Dispersion is the standard deviation of the true single-grain ages as a percentage of their central age [Galbraith, 2010].

<sup>i</sup>SD is the standard deviation of measured horizontal confined track lengths.

<sup>j</sup>Mean track length after individual track length measurements are corrected for their orientation to the c axis after Ketcham [2005].

<sup>k</sup>HCT = horizontal confined track.

negatively skewed with a large proportion of longer tracks and tail of shorter tracks (see Text S2 for all track length distribution plots).

Radial plots graphically illustrating single-grain dispersion can be found in Text S3. A chi-square ( $\chi^2$ ) age homogeneity test was performed on all samples to assess whether the measured single-grain ages represent a single population [Galbraith, 2010]. Nine samples yielded  $P(\chi^2)$  equal to or less than 0.05. Despite failing the chi-square test, a mixture model [Galbraith and Green, 1990] (Text S3) does not define a clear distinction of two or more populations. For the majority of samples, single-grain fission track age dispersion is moderate to low (i.e.,  $\leq 20\%$ ). Samples with higher levels of dispersion are typically associated with samples with low track densities. It is likely that every sample is best approximated by a single population, and any apparent dispersion in single-grain ages is predominantly induced by intergrain variations in compositionally controlled track annealing rates.

The classic “boomerang” relationship [e.g., Green, 1986; Gallagher and Brown, 1997] is not seen for this data set, as almost all MTLs are reasonably long and similar in value (i.e.,  $>13 \mu\text{m}$ ) and because there is a fairly narrow age range for most samples (approximately 80–120 Ma) (Figure 3b). As there are no clear peaks in the boomerang plot, it is not possible to define discrete thermal events, and it is likely that most samples resided at elevated temperatures and were entirely, or almost entirely, reset prior to the Cretaceous. However, several samples have short ( $<13 \mu\text{m}$ ) MTL and young AFT ages (approximately  $<80$  Ma), implying that these samples may have resided at temperatures within the partial annealing zone (PAZ) following an initial cooling event and then either cooled during a distinct cooling event or by slow, protracted cooling.

$D_{\text{par}}$  values range from 1.45 to  $3.42 \mu\text{m}$  with most values (76% of samples) falling between 1.7 and  $2.3 \mu\text{m}$ . While many samples have comparable  $D_{\text{par}}$  measurements with Durango apatite ( $2.05 \pm 0.16 \mu\text{m}$ ) [Sobel and Seward, 2010], many fall out with the Durango range. This variation means that some samples have compositionally



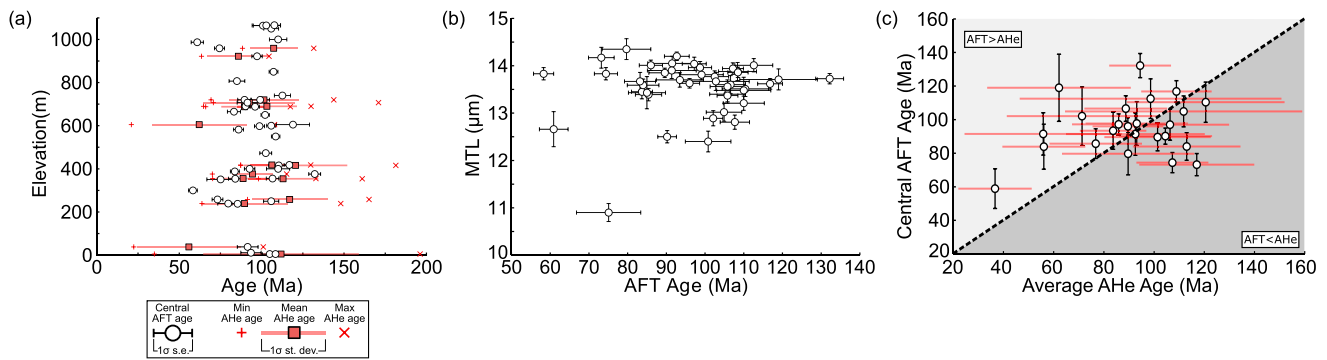


**Figure 3.** (a) Plot of AFT and AHe age against elevation. White circles are central AFT ages with uncertainty bars representing  $1\sigma$  standard error on the central age. Red squares are uncorrected mean AHe ages with uncertainty bars representing  $1\sigma$  standard deviation (standard deviation is used in this instance to highlight the dispersion in single-grain AHe ages), red plus symbol and crosses represent the minimum and maximum AHe single-grain age. (b) AFT age against MTLs uncorrected for their  $c$  axis orientation. In AFT ages are central AFT ages with  $1\sigma$  standard error; MTLs are uncorrected for their  $c$  axis orientation with  $1\sigma$  standard error. (c) Plot of central AFT ages against mean AHe age. Vertical error bars are  $1\sigma$  standard error on the central age, and horizontal error bars are  $1\sigma$  standard deviation on the mean AHe age. Dashed line represents the one-to-one relationship.

controlled annealing properties different from Durango standard. Any significant compositional control over annealing is treated appropriately during thermal history inversion.

### 3.2. Apatite (U-Th-Sm)/He Results

Multiple single-grain (U-Th-Sm)/He analyses were performed on a subset of 16 samples that were chosen based on the high quality of the apatite separates and optimal geographical location for the study (Table 2). Between 5 and 21 single-grain ages were determined for each sample in an attempt to quantify and utilize the intersample grain date dispersion (see below). Details on analytical techniques can be found in Text S4. Mean AHe ages, uncorrected for alpha ejection, range from  $55.8 \pm 31.34$  to  $120.6 \pm 31.4$  Ma, and alpha ejection corrected ages [after Farley *et al.*, 1996] range from  $74.0 \pm 43.9$  to  $156.9 \pm 40.9$  Ma. Although “mean” AHe sample ages provide a useful frame of reference for comparison with AFT ages and the wider geological context, they do not necessarily correspond to a specific geological event at that time. In a similar manner to an AFT age, an AHe age is a product of a thermal history that is initially unknown. Depending on the form of this thermal history and the chemical and physical properties of individual apatite grains, mean AHe ages can be associated with large degrees of single-grain age dispersion. Dispersion (standard deviation of age/mean age) is large for samples in our data set, ranging from 12 to 56%. As thermal diffusion of  $^4\text{He}$  dominates at elevated temperatures [Brown *et al.*, 2013], the style of thermal history experienced by a sample will almost always lead to an over-correction of the  $^4\text{He}$  age using a single alpha-correction factor [Farley *et al.*, 1996; Meesters and Dunai, 2002a, 2002b; Herman *et al.*, 2007; Gautheron *et al.*, 2012]. This effect may be a contributing cause of some of the corrected AHe ages being older than their corresponding AFT age (Figure 3c) and the magnitude of single-grain age dispersion (Figure 4 and Text S5). However, as the interaction between alpha ejection, radiation damage effects, and He diffusion remains poorly understood, we have chosen to quote raw, uncorrected, AHe ages and we deal with the effect of alpha ejection by accounting for  $^4\text{He}$  lost through alpha ejection during each time step of the modeling approach following the approach proposed by Meesters and Dunai [2002a, 2002b].

Variation in effective uranium (eU) content, grain size, and whether or not crystals analyzed are fragments of larger crystals have been shown to be key factors that control the measured AHe date for a particular grain (Table 3) [Flowers *et al.*, 2009; Gautheron *et al.*, 2009; Reiners and Farley, 2001; Brown *et al.*, 2013; Beucher *et al.*, 2013]. If a sample has experienced relatively slow cooling through the partial He retention zone, then positive correlations of spherical equivalent grain radius ( $R^*$ ) and/or eU with AHe age may be evident [Reiners and Farley, 2001; Flowers *et al.*, 2009]. However, as demonstrated by Brown *et al.* [2013], the combined effects of these influences may decouple the expected correlation. Moreover, a large number of grains analyzed in this study were fragments of larger grains and had only 1 (1T) or no (0T) terminations, and therefore, simple 2-D correlations between eU and  $R^*$  and grain date will be disrupted (Figure 4). Despite this, many samples do show an apparent positive age- $R^*$  correlation (see Text S5 for all  $R^*$  and eU-AHe date plots). Sample NQ12-15 is the only sample for which we can observe a negative date- $R^*$  correlation, although this sample has the fewest number of grains and therefore the correlation is poorly constrained.

**Table 2.** Results of Apatite (U-Th-Sm)/He Analysis<sup>a</sup>

Sample	Grain #	(cc)	(ng)	(ppm)	(ng)	(ppm)	(ng)	(ppm)	(ng)	(ppm)	T <sup>c</sup>	(μm)	(μm)	F <sub>t</sub>	(Ma)		Average		SD			
															(Ma)	8.4	94.4	12.3	Average	SD		
JN2	1	1.8E-09	0.10	69.3	7.2E-04	0.50	0.42	291.4	138.3	1	116.3	70.5	40.6	0.62	74.6	121.2	13.7	94.4	12.3	138.5	14.4	
	2	2.0E-09	0.05	36.9	3.6E-04	0.27	0.77	567.3	170.4	1	112.6	69.4	39.8	0.59	70.1	118.5	13.6					
	3	1.8E-09	0.07	52.3	5.2E-04	0.38	0.51	367.7	139.0	1	120.1	67.9	39.7	0.60	78.3	130.7	14.9					
	4	8.9E-09	0.27	73.5	1.9E-03	0.53	1.98	545.7	202.3	2	187.9	87.7	53.3	0.70	99.2	11.3	141.4					
	5	9.3E-09	0.25	69.0	1.8E-03	0.50	2.21	613.6	213.7	2	197.7	85.2	52.6	0.70	98.9	11.3	142.3					
	6	8.9E-09	0.14	66.1	1.0E-03	0.48	2.57	1170.7	341.7	2	126.4	83.2	46.9	0.65	97.2	11.2	149.0					
	7	8.7E-09	0.27	102.8	1.9E-03	0.75	1.74	663.5	259.5	2	158.8	81.1	48.5	0.67	105.3	12.0	156.5					
	8	5.9E-09	0.12	32.4	8.6E-04	0.24	1.87	507.2	151.8	2	167.6	93.6	54.9	0.70	86.0	9.9	122.2					
	9	9.8E-09	0.25	83.7	1.8E-03	0.61	2.57	866.0	287.8	1	117.4	100.3	52.7	0.69	94.2	10.8	135.6					
	10	5.7E-09	0.14	53.6	1.0E-03	0.39	1.80	667.3	210.8	1	116.1	96.1	51.0	0.68	82.6	9.5	121.0					
	12	1.5E-08	0.23	71.2	1.7E-03	0.52	4.47	1372.7	394.3	2	152.6	92.2	53.1	0.69	94.6	10.9	136.7					
	17	1.9E-08	0.46	99.9	3.3E-03	0.72	4.02	864.1	303.7	1	192.7	98.1	58.6	0.73	112.5	12.9	154.2					
	18	2.2E-08	0.62	125.1	4.5E-03	0.91	4.82	959.4	351.4	1	208.5	97.9	59.5	0.73	102.9	11.8	140.6					
	19	7.1E-09	0.20	66.6	1.4E-03	0.48	1.35	446.0	171.9	1	120.7	99.8	53.0	0.70	111.8	12.8	159.6					
	20	7.8E-09	0.27	83.5	2.0E-03	0.61	1.82	548.3	213.0	1	139.5	97.3	54.1	0.71	90.9	10.4	128.6					
	21	8.2E-09	0.32	87.8	2.3E-03	0.64	1.68	463.9	197.5	1	160.5	94.7	54.9	0.71	94.1	10.7	132.0					
	23	3.9E-09	0.11	49.5	7.7E-04	0.36	1.01	464.8	159.1	1	96.2	94.6	47.6	0.66	93.1	10.7	140.4					
	24	7.2E-09	0.21	62.6	1.5E-03	0.45	1.28	373.8	150.9	1	152.2	94.6	54.1	0.71	115.2	13.1	162.7					
	25	3.7E-09	0.10	47.6	7.6E-04	0.35	0.86	389.7	139.6	1	101.6	93.2	47.9	0.67	99.5	11.4	149.4					
	26	4.1E-09	0.15	43.2	1.1E-03	0.31	1.13	321.3	119.0	1	146.2	97.8	55.0	0.71	80.6	9.2	113.5					
	27	5.1E-09	0.17	81.7	1.2E-03	0.59	1.02	480.0	195.1	1	101.9	91.0	47.2	0.67	101.5	11.6	152.5					
	JN3	1	2.6E-09	0.16	24.2	1.1E-03	0.18	0.20	29.9	31.4	1	170.4	124.1	68.2	0.78	103.6	11.4	132.5	106.2	12.9	140.6	18.7
		2	3.0E-09	0.17	12.7	1.3E-03	0.09	0.12	8.6	14.8	1	187.7	171.4	88.2	0.83	122.0	13.4	146.2				
		3	2.2E-09	0.15	32.3	1.1E-03	0.23	0.17	38.0	41.4	2	187.6	98.2	58.4	0.75	95.1	10.5	127.4				
		4	3.9E-09	0.22	42.8	1.6E-03	0.31	0.34	66.9	58.8	1	157.9	113.5	62.6	0.76	107.0	11.9	140.7				
		5	2.7E-09	0.16	16.5	1.2E-03	0.12	0.17	17.1	20.7	1	184.4	146.2	78.5	0.81	107.1	11.8	131.8				
		6	1.9E-09	0.11	20.3	7.7E-04	0.15	0.19	36.0	28.9	1	160.9	113.9	63.1	0.76	103.6	11.5	136.1				
7		2.5E-09	0.08	18.0	6.1E-04	0.13	0.51	109.2	43.8	2	191.3	99.0	59.0	0.73	100.3	11.5	144.3					
8		2.4E-09	0.13	30.9	9.4E-04	0.22	0.39	93.0	53.0	1	120.4	118.3	59.5	0.74	87.2	9.8	120.9					
9		2.5E-09	0.13	20.9	9.4E-04	0.15	0.11	17.7	25.3	1	210.8	108.6	64.8	0.77	129.8	14.3	185.7					
NQ12-04	1	5.1E-09	0.40	42.77	2.9E-03	0.31	0.13	13.8	46.3	1	328.6	106.1	68.5	0.79	96.4	13.5	122.0	101.4	21.2	134.8	25.6	
	2	4.5E-09	0.29	63.33	2.1E-03	0.46	0.45	100.2	87.3	1	202.1	94.5	57.4	0.74	93.4	12.7	126.4					
	4	1.2E-09	0.08	30.30	6.2E-04	0.22	0.03	10.9	0.36	129.1	33.1	2	188.7	76.8	47.9	0.70	101.0					
	5	4.3E-09	0.22	29.71	1.6E-03	0.22	0.06	7.4	0.92	124.0	31.7	2	196.2	123.0	70.2	0.80	143.8					
	6	1.4E-09	0.12	23.07	8.6E-04	0.17	0.03	5.9	24.6	1	142.7	119.9	63.3	0.77	92.4	13.0	119.4					
	7	3.3E-10	0.03	9.70	2.2E-04	0.07	0.03	8.7	0.30	96.6	11.8	2	187.8	80.6	49.8	0.70	69.3					
	8	2.5E-09	0.20	24.72	1.5E-03	0.18	0.06	7.2	26.6	2	261.9	111.5	68.9	0.79	93.6	13.1	118.2					
	12	2.0E-09	0.12	38.85	8.9E-04	0.28	0.16	52.1	0.34	109.4	51.4	2	164.8	87.2	51.7	0.71	98.1					
	22	2.1E-09	0.12	23.27	8.6E-04	0.17	0.05	10.0	0.53	104.7	25.8	2	245.4	90.9	57.5	0.75	124.4					
	NQ12-06	3	4.4E-09	0.21	33.3	1.5E-03	0.24	1.46	230.01	0.69	108.7	87.8	1	176.6	119.6	67.0	0.76	64.7	103.2	18.3	135.7	23.3
		4	3.6E-09	0.17	37.8	1.3E-03	0.27	0.53	115.71	0.35	74.9	65.22	1	165.4	105.3	59.9	0.74	96.7				
		5	7.9E-09	0.49	64.2	3.5E-03	0.47	0.45	60.10	1.50	198.7	78.74	1	191.3	125.4	70.8	0.79	105.9				
6		1.5E-08	0.88	128.9	6.4E-03	0.93	0.95	138.30	1.23	179.4	162.34	2	247.9	104.8	64.9	0.77	110.0					
8		1.0E-08	0.51	60.5	3.7E-03	0.44	1.24	147.70	1.04	124.6	95.64	1	176.6	137.4	74.2	0.79	105.1					
9		1.2E-09	0.05	14.1	3.5E-04	0.10	0.17	50.83	0.13	37.9	26.11	1	176.0	88.1	52.9	0.71	109.2					
NQ12-07	14	4.7E-09	0.13	19.3	9.4E-04	0.14	0.68	100.70	0.54	80.4	43.08	2	191.7	118.3	67.8	0.77	130.0					
	16	5.7E-09	0.11	17.0	8.1E-04	0.12	1.40	213.17	0.76	115.8	67.19	2	241.0	104.3	64.3	0.75	103.7					
	2	1.9E-09	0.12	51.0	8.9E-04	0.37	0.29	121.0	0.19	77.5	79.8	2	168.3	75.3	46.2	0.67	80.7	89.6	14.1	122.5	19.1	
	4	2.9E-09	0.21	46.9	1.5E-03	0.34	0.17	37.4	0.24	53.9	56.1	1	175.6	100.6	58.7	0.75	94.2					
	7	4.0E-10	0.02	14.8	1.5E-04	0.11	0.12	84.0			34.6	2	123.9	68.1	40.1	0.61	66.0					

Table 2. (continued)

Sample	Grain #	(cc)	(ng)	(ppm)	(ng)	(ppm)	(ng)	(ppm)	(ng)	(ppm)	(ppm)	(ng)	(ppm)	T <sup>c</sup>	(μm)	(μm)	F <sub>t</sub>	(Ma)		Average		SD	
																		(Ma)	(Ma)	Average	SD	Average	SD
NQ12-09	8	4.3E-09	0.23	35.7	1.6E-03	0.26	0.30	47.2	0.42	65.3	47.0	1	202.2	111.9	65.7	0.77	152.3	15.7	115.9	15.7	152.3	20.7	
	9	5.8E-10	0.04	47.5	3.2E-04	0.34	0.08	89.7	69.0	2	153.3	49.4	31.9	0.53	73.8	10.0	97.0	10.0	73.8	10.0	97.0	13.2	
	13	3.2E-09	0.15	27.7	1.1E-03	0.20	0.40	72.6	0.33	59.7	44.9	2	228.4	97.6	60.3	0.75	104.0	11.5	104.0	11.5	104.0	15.3	
	15	1.7E-09	0.10	38.5	7.1E-04	0.28	0.18	69.5	0.17	67.4	55.1	1	112.9	95.0	50.2	0.70	95.9	13.1	95.9	13.1	95.9	19.1	
	16	5.5E-10	0.04	17.7	3.0E-04	0.13	0.06	24.5	0.11	46.2	23.6	2	140.8	81.4	47.4	0.69	80.9	8.9	80.9	8.9	80.9	13.0	
	17	1.8E-09	0.13	49.3	9.7E-04	0.36	0.10	37.6	58.4	2	166.5	80.5	48.6	0.70	91.0	12.3	119.6	12.3	91.0	12.3	119.6	16.2	
	25	2.0E-09	0.12	22.5	8.7E-04	0.16	0.20	37.7	0.29	53.8	31.6	1	154.0	117.0	63.6	0.76	97.6	13.3	97.6	13.3	97.6	17.7	
	26	1.6E-09	0.12	49.3	8.5E-04	0.36	0.14	57.0	0.18	74.5	63.1	2	134.0	84.2	48.1	0.69	88.8	9.7	88.8	9.7	88.8	14.1	
	28	1.2E-09	0.12	89.2	8.6E-04	0.65	0.06	44.3	100.3	2	131.5	63.4	38.3	0.62	73.9	10.0	97.2	10.0	73.9	10.0	97.2	13.2	
	33	1.2E-09	0.07	16.5	5.3E-04	0.12	0.07	15.9	0.24	55.1	20.4	2	200.4	93.9	57.1	0.82	101.8	11.2	101.8	11.2	101.8	15.2	
	1	1.2E-09	0.04	32.2	3.1E-04	0.23	0.39	293.8	0.09	70.0	101.4	2	146.3	60.3	37.5	0.57	70.3	7.9	70.3	7.9	70.3	13.8	
	2	1.9E-09	0.06	21.0	4.4E-04	0.15	0.63	215.1	0.11	36.3	71.7	2	177.4	80.9	49.4	0.67	73.9	8.3	73.9	8.3	73.9	12.3	
	3	2.4E-09	0.08	21.8	5.5E-04	0.16	0.59	169.2	61.7	0	128.4	103.7	55.4	0.71	90.1	13.0	126.5	13.0	90.1	13.0	126.5	18.3	
	5	7.5E-09	0.18	18.2	1.3E-03	0.13	1.94	197.3	64.6	0	191.2	143.2	78.1	0.79	96.2	14.0	121.2	14.0	96.2	14.0	121.2	17.7	
	6	5.1E-09	0.10	17.0	7.6E-04	0.12	0.89	144.3	0.19	30.8	51.0	2	158.9	124.3	67.0	0.76	132.9	14.9	132.9	14.9	132.9	19.6	
	7	2.6E-09	0.10	18.5	7.0E-04	0.13	0.64	121.7	47.3	0	192.8	103.8	61.3	0.74	84.7	12.2	114.2	12.2	84.7	12.2	114.2	16.4	
	8	2.0E-09	0.06	10.3	4.0E-04	0.07	0.54	99.7	0.24	44.1	33.8	1	157.2	117.1	64.0	0.75	86.7	9.7	86.7	9.7	86.7	13.0	
9	1.2E-09	0.04	11.6	2.6E-04	0.08	0.34	108.4	0.14	43.6	37.2	1	142.3	93.5	52.8	0.70	85.7	9.4	85.7	9.4	85.7	13.5		
11	1.0E-09	0.04	22.0	2.7E-04	0.16	0.31	181.9	64.9	1	111.5	77.8	43.3	0.63	77.4	11.2	122.8	11.2	77.4	11.2	122.8	17.8		
12	3.2E-09	0.10	23.1	7.0E-04	0.17	0.88	211.4	0.19	45.5	73.0	1	150.3	105.0	58.4	0.73	86.8	12.6	86.8	12.6	86.8	17.4		
15	9.7E-10	0.03	7.8	1.9E-04	0.06	0.30	88.2	28.5	1	133.6	100.8	54.9	0.71	82.0	11.9	116.1	11.9	82.0	11.9	116.1	16.9		
16	4.2E-09	0.10	20.2	7.5E-04	0.15	0.88	171.6	0.20	39.4	60.7	2	206.9	99.5	60.1	0.73	108.4	12.2	108.4	12.2	108.4	16.6		
17	2.8E-09	0.10	31.0	6.9E-04	0.22	0.86	279.3	0.08	27.2	96.8	1	143.2	92.3	52.4	0.71	78.3	11.4	78.3	11.4	78.3	16.4		
NQ12-10	2	6.7E-10	0.06	19.4	4.4E-04	0.14	0.02	6.6	0.23	72.9	21.1	1	103.1	109.8	53.7	0.73	81.7	9.5	81.7	9.5	81.7	12.9	
	3	9.5E-10	0.08	17.7	5.6E-04	0.13	0.02	5.0	0.28	64.6	19.0	1	178.6	98.5	57.9	0.75	91.8	10.6	91.8	10.6	91.8	14.0	
	4	7.2E-10	0.04	18.6	2.8E-04	0.13	0.02	7.8	0.10	49.2	20.5	1	152.8	73.5	44.4	0.68	136.4	17.9	136.4	17.9	136.4	26.6	
	5	3.1E-10	0.04	9.3	2.7E-04	0.07	0.01	2.6	10.0	1	108.1	121.1	58.2	0.75	63.8	9.0	84.6	9.0	63.8	9.0	84.6	11.9	
	6	1.1E-09	0.08	25.6	5.9E-04	0.19	0.02	5.5	0.26	82.7	27.1	1	163.2	87.7	51.9	0.72	101.4	12.9	101.4	12.9	101.4	17.8	
	8	5.5E-10	0.06	20.4	4.5E-04	0.15	0.03	8.6	0.02	3.4	22.6	1	172.7	83.3	50.3	0.71	66.3	9.2	66.3	9.2	66.3	12.8	
	9	1.5E-09	0.12	27.3	8.8E-04	0.20	0.03	7.2	0.34	75.8	29.2	1	146.6	109.7	59.9	0.76	90.3	10.0	90.3	10.0	90.3	13.1	
	10	1.4E-09	0.12	24.4	8.9E-04	0.18	0.02	3.4	0.28	60.9	18.6	2	179.4	101.2	59.2	0.76	65.8	7.4	65.8	7.4	65.8	16.9	
	12	7.1E-10	0.08	16.8	5.6E-04	0.12	0.03	7.2	0.28	60.9	18.6	2	179.4	101.2	59.2	0.76	65.8	7.4	65.8	7.4	65.8	9.8	
	13	3.9E-10	0.04	23.4	3.2E-04	0.17	0.02	8.8	0.02	8.8	25.6	1	105.0	84.5	45.2	0.68	66.3	9.2	66.3	9.2	66.3	13.5	
	14	4.7E-09	0.30	19.6	2.2E-03	0.14	0.19	12.1	1.59	104.0	22.6	1	194.9	176.8	91.2	0.84	107.2	11.9	107.2	11.9	107.2	14.2	
	15	5.8E-10	0.06	13.3	4.3E-04	0.10	0.02	5.0	0.02	5.0	14.6	1	155.1	107.3	59.8	0.76	72.8	10.1	72.8	10.1	72.8	13.3	
	17	5.8E-10	0.06	18.2	4.0E-04	0.13	0.04	13.1	0.13	60.6	13.3	2	143.2	92.3	52.4	0.72	72.9	7.9	72.9	7.9	72.9	11.4	
	18	5.2E-10	0.02	11.8	1.8E-04	0.09	0.01	6.1	0.13	60.6	13.3	2	138.4	77.1	45.2	0.68	148.0	19.9	148.0	19.9	148.0	29.3	
	NQ12-11	5	5.9E-10	0.04	6.4	3.0E-04	0.05	0.03	4.9	0.16	25.8	7.6	1	185.1	116.8	66.6	0.78	99.2	10.9	99.2	10.9	99.2	13.9
		6	4.7E-10	0.03	3.7	1.9E-04	0.03	0.02	3.3	0.14	19.7	4.5	1	227.6	111.4	67.1	0.78	115.4	12.8	115.4	12.8	115.4	16.4
		7	3.4E-10	0.02	3.6	1.3E-04	0.03	0.03	6.1	5.1	1	234.6	93.1	58.3	0.74	109.4	11.9	147.4	11.9	109.4	11.9	147.4	16.0
8		8.7E-10	0.04	9.8	2.9E-04	0.07	0.03	6.8	11.5	0	155.8	101.5	57.4	0.75	153.6	20.9	205.9	20.9	153.6	20.9	205.9	28.0	
10		1.7E-10	0.01	2.8	8.8E-05	0.02	0.01	1.7	3.2	1	122.4	119.2	60.1	0.76	101.1	24.8	133.4	24.8	101.1	24.8	133.4	32.7	
11		3.5E-10	0.01	2.0	1.0E-04	0.01	0.01	1.2	2.2	0	202.8	117.7	68.4	0.79	181.4	24.7	230.3	24.7	181.4	24.7	230.3	31.4	
12		4.4E-10	0.03	5.3	1.9E-04	0.04	0.02	3.8	6.3	1	180.2	104.6	60.8	0.76	117.1	14.5	154.1	14.5	117.1	14.5	154.1	19.1	
NQ12-13	13	3.8E-10	0.03	4.1	2.4E-04	0.03	0.01	1.4	4.4	1	194.5	128.0	72.2	0.80	87.3	12.2	109.0	12.2	87.3	12.2	109.0	15.2	
	1	8.7E-10	0.06	7.2	4.6E-04	0.05	0.04	4.3	8.3	1	186.5	136.7	75.0	0.81	98.9	13.5	122.6	13.5	98.9	13.5	122.6	16.7	
	3	2.1E-09	0.14	19.3	1.0E-03	0.14	0.10	14.0	22.8	1	177.6	127.1	70.2	0.79	107.3	14.6	135.5	14.6	107.3	14.6	135.5	18.4	
	4	7.7E-10	0.05	15.6	3.7E-04	0.11	0.05	14.7	19.2	2	202.1	80.0	50.1	0.71	98.1	10.9	138.9	10.9	98.1	10.9	138.9	15.5	
	5	1.6E-09	0.07	9.6	5.2E-04	0.07	0.04	5.0	10.9	1	206.8	120.1	69.8	0.79	161.0	22.1	203.2	22.1	161.0	22.1	203.2	27.9	
	7	1.0E-09	0.07	15.2	5.0E-04	0.11	0.03	7.4	17.1	1	209.7	93.1	57.1	0.75	104.8	14.4	140.3	14.4	104.8	14.4	140.3	19.3	
	1	8.7E-10	0.06	7.2	4.6E-04	0.05	0.04	4.3	8.3	1	186.5	136.7	75.0	0.81	98.9	13							

**Table 2.** (continued)

Sample	Grain #	(cc)	(ng)	(ppm)	(ng)	(ppm)	(ng)	(ppm)	(ppm)	(ng)	(ppm)	T <sup>c</sup>	(μm)	(μm)	F <sub>t</sub>	Average		SD		(Ma)	Average	SD	SD	
																(ppm)	(Ma)	(Ma)	(Ma)					
NQ12-15	8	2.0E-09	0.14	42.4	1.0E-03	0.31	0.05	16.3	0.14	40.8	46.6	2	180.1	85.5	51.8	0.72	104.9	11.8	145.3	16.4				
	10	8.1E-10	0.04	11.5	2.9E-04	0.08	0.03	8.6	0.15	44.4	13.6	2	149.7	96.1	54.5	0.73	136.4	16.2	186.3	22.1				
	12	1.7E-09	0.11	15.0	7.8E-04	0.11	0.09	12.1			17.9	1	202.5	118.9	68.9	0.79	106.1	14.4	134.7	18.3				
	15	8.2E-10	0.05	10.2	3.9E-04	0.07	0.05	8.6	0.29	54.7	12.3	2	213.4	99.7	60.6	0.76	99.3	11.2	131.0	14.8				
	2	4.1E-11	0.01	1.1	6.0E-05	0.01	0.03	3.6	0.03	4.6	2.0	1	219.2	116.1	68.9	0.78	22.4	3.4	28.9	4.4	55.8	31.3	74.3	
	3	2.0E-10	0.02	2.1	1.5E-04	0.02	0.12	12.3	0.12	12.5	5.0	2	260.4	121.9	74.1	0.79	32.1	3.5	40.8	4.5				
	6	2.7E-10	0.01	2.3	9.5E-05	0.02	0.07	13.2	0.06	10.0	5.4	2	255.2	94.1	59.6	0.74	70.1	8.8	95.4	11.9				
	7	1.1E-10	0.01	1.1	5.8E-05	0.01	0.03	4.6			2.1	0	192.8	103.8	61.3	0.75	53.5	5.8	68.8	7.5				
NQ12-17	8	2.9E-10	0.01	2.4	8.6E-05	0.02	0.05	9.5	0.04	8.5	4.7	2	212.3	95.6	58.5	0.73	101.0	16.4	137.5	22.3				
	2	1.3E-09	0.092	9.0	6.7E-04	0.07	0.03	2.8	0.13	12.8	9.7	1	170.6	154.6	79.8	0.82	104.5	13.8	127.4	16.8	111.8	47.3	136.4	
	4	3.4E-10	0.028	6.8	2.0E-04	0.05	0.01	3.5			7.7	2	180.9	94.9	56.4	0.74	88.7	12.2	119.4	16.4				
	6	2.9E-09	0.151	6.9	1.1E-03	0.05	0.11	5.1	0.22	10.3	8.1	1	229.8	194.9	102.6	0.86	132.9	14.2	155.0	16.5				
	7	1.2E-09	0.075	5.7	5.4E-04	0.04	0.07	5.1			0.0	6.9	2	227.9	151.9	85.4	0.83	111.1	15.1	133.7	18.1			
	8	3.1E-10	0.064	5.3	4.6E-04	0.04	0.03	2.3	0.25	20.7	5.9	2	211.5	149.5	82.8	0.83	34.9	4.0	42.2	4.8				
	9	3.9E-09	0.194	8.0	1.4E-03	0.06	0.38	15.7			11.7	2	243.6	199.2	106.0	0.86	112.6	15.4	130.2	17.9				
	10	5.8E-10	0.055	5.3	4.0E-04	0.04	0.10	9.3	0.19	17.8	7.5	2	206.7	141.4	79.0	0.81	59.9	6.6	74.0	8.1				
SA12-22	11	6.8E-10	0.048	4.8	3.5E-04	0.03	0.02	2.4			5.4	2	169.6	153.1	79.1	0.82	102.7	14.1	126.0	17.3				
	12	2.2E-09	0.090	13.1	6.5E-04	0.10	0.03	4.1	0.08	12.3	14.2	1	178.9	123.6	68.9	0.79	181.3	22.0	229.1	27.7				
	13	5.4E-10	0.065	8.3	4.7E-04	0.06	0.03	3.6	0.12	15.7	9.2	2	182.7	130.5	72.1	0.80	60.4	7.0	75.6	8.8				
	16	4.4E-09	0.187	10.9	1.4E-03	0.08	0.13	7.6	0.31	17.8	12.8	1	217.0	177.5	94.5	0.85	161.3	17.2	190.7	20.3				
	18	2.5E-09	0.090	8.8	6.5E-04	0.06	0.05	5.1	0.21	20.2	10.0	2	190.4	146.1	79.2	0.82	196.2	21.5	240.2	26.4				
	19	8.3E-10	0.058	5.5	4.2E-04	0.04	0.02	2.2			6.1	2	181.5	151.5	80.2	0.82	106.4	14.7	129.9	18.0				
	1	4.5E-09	0.52	37.3	3.8E-03	0.27	0.26	19.0			42.0	2	295.9	136.6	83.2	0.83	63.5	7.1	76.9	8.6	85.9	18.6	108.4	
	2	3.4E-09	0.28	37.0	2.0E-03	0.27	0.15	19.1			41.7	1	201.0	122.8	70.6	0.79	89.0	10.0	112.0	12.6				
SA12-30	3	3.1E-09	0.29	25.5	2.1E-03	0.18	0.30	26.1			31.8	2	237.4	139.2	80.7	0.82	70.0	7.8	85.7	9.5				
	4	5.6E-09	0.36	84.5	2.6E-03	0.61	0.35	82.3			104.5	2	156.3	104.3	58.7	0.75	102.4	11.3	136.7	15.1				
	7	1.1E-08	0.74	86.0	5.3E-03	0.62	0.64	74.2			104.1	2	214.7	126.0	73.1	0.80	104.5	11.5	130.7	14.4				
	1	5.0E-09	0.30	13.7	2.2E-03	0.10	0.06	3.0	1.19	54.5	14.5	1	302.6	169.1	99.1	0.86	127.0	13.8	148.4	16.1	117.0	22.9	144.0	
	2	9.0E-10	0.07	20.0	5.4E-04	0.15	0.01	3.8	0.37	98.9	21.1	1	160.3	95.9	55.3	0.74	91.4	11.6	123.1	15.6				
	3	1.1E-09	0.08	11.5	5.9E-04	0.08	0.02	3.2	0.40	56.4	12.3	1	250.5	106.0	65.6	0.78	98.8	11.1	126.4	14.2				
	5	4.2E-09	0.31	15.2	2.2E-03	0.11	0.02	0.8			15.5	1	260.8	175.5	98.5	0.86	110.1	16.2	128.6	19.0				
	6	1.7E-09	0.09	8.6	6.7E-04	0.06	0.01	1.0			8.9	1	307.0	117.9	74.2	0.81	146.8	21.3	181.6	26.4				
SA12-35	8	1.9E-09	0.15	13.1	1.1E-03	0.09	0.02	1.5			13.5	1	239.7	138.1	80.4	0.82	100.5	14.6	122.0	17.7				
	9	9.7E-09	0.44	13.0	3.2E-03	0.09	0.06	1.8	2.67	79.3	13.6	1	317.4	205.6	116.5	0.88	165.2	18.1	188.2	20.6				
	10	2.3E-09	0.12	11.9	8.8E-04	0.09	0.07	7.1	0.86	84.6	13.6	1	197.0	143.3	78.8	0.82	129.1	14.1	158.3	17.3				
	11	1.5E-09	0.13	23.8	9.5E-04	0.17	0.01	2.5			24.5	1	249.6	93.8	59.2	0.76	91.5	13.3	120.4	17.5				
	12	2.7E-09	0.18	11.7	1.3E-03	0.09	0.02	1.1	0.85	55.6	12.1	2	302.9	141.8	86.2	0.84	113.5	13.7	135.9	16.4				
	14	4.9E-09	0.26	21.0	1.9E-03	0.15	0.04	3.0			21.9	1	225.6	147.9	83.5	0.83	147.7	21.3	178.1	25.7				
	16	9.3E-10	0.07	9.9	5.0E-04	0.07	0.01	2.1	0.43	61.5	10.4	2	212.9	114.2	67.6	0.79	99.4	12.0	126.1	15.2				
	17	1.2E-09	0.08	17.3	5.9E-04	0.13	0.02	4.3	0.36	77.4	18.4	2	203.5	95.6	58.1	0.75	107.0	12.5	142.1	16.5				
	19	1.5E-09	0.10	13.6	7.6E-04	0.10	0.01	0.7	0.52	67.8	13.9	1	162.4	137.4	72.4	0.80	109.9	29.5	136.6	36.6				
	4	4.2E-10	0.02	2.7	1.4E-04	0.02	0.04	5.8	0.37	51.9	4.1	1	174.3	127.5	70.0	0.78	107.8	14.9	137.6	19.0	62.1	28.6	81.1	
	5	1.7E-10	0.02	3.5	1.2E-04	0.03	0.03	5.4			4.8	1	216.5	94.1	58.0	0.74	60.0	8.2	80.9	11.0				
	6	4.9E-11	0.01	1.2	6.0E-05	0.01	0.03	4.6	0.37		2.2	2	234.5	110.5	67.1	0.77	20.9	2.4	27.3	3.1				
	7	8.9E-10	0.01	1.1	1.1E-04	0.01	0.21	15.1	0.76	55.3	4.6	1	157.6	186.5	87.9	0.82	104.4	15.3	128.1	18.8				
	10	2.3E-10	0.01	2.5	1.0E-04	0.02	0.07	11.9	0.28	49.9	5.3	1	207.4	103.1	61.9	0.75	60.8	8.7	81.4	11.6				
	11	8.3E-11	0.01	2.2	8.2E-05	0.02	0.06	12.2			5.1	2	237.5	93.1	58.4	0.73	26.0	3.7	35.7	5.1				
	13	5.0E-10	0.08	7.2	5.8E-04	0.05	0.19	17.5			11.4	2	248.0	132.9	78.6	0.81	32.6	4.5	40.4	5.6				
	14	2.2E-10	0.02	3.5	1.2E-04	0.03	0.06	13.8			6.7	1	143.9	112.3	60.6	0.74	59.4	8.4	79.9	11.3				

**Table 2.** (continued)

Sample	Grain #	<sup>4</sup> He (cc)	<sup>238</sup> U (ng)	<sup>235</sup> U (ng)	<sup>232</sup> Th (ng)	<sup>147</sup> Sm (ng)	eU <sup>b</sup> (ppm)	T <sup>c</sup> (μm)	L <sup>d</sup> (μm)	W <sup>d</sup> (μm)	R <sup>e</sup> (μm)	F <sub>t</sub>	±Estimated UC <sup>g</sup>		Corrected Age <sup>h</sup>		Raw Age (Ma)		Corrected Age (Ma)	
													Age	(Ma)	Average	SD	Average	SD	Average	SD
SA12-36	15	2.9E-10	0.02	2.6	1.5E-04	0.02	0.05	5.8	4.0	1	199.3	127.7	72.5	0.79	73.7	10.2	93.2	12.9		
	16	2.6E-10	0.02	3.8	1.4E-04	0.03	0.03	5.8	5.2	1	219.0	96.4	59.3	0.75	78.8	10.7	105.4	14.3		
	17	2.0E-10	0.01	2.4	8.3E-05	0.02	0.07	15.3	6.1	2	245.0	87.6	55.7	0.72	58.8	8.4	82.1	11.8		
	1	1.3E-09	0.03	4.2	1.9E-04	0.03	0.43	68.5	20.2	2	245.2	101.0	62.8	0.74	81.0	11.9	109.3	16.1	92.5	27.7
	3	8.5E-10	0.03	5.0	2.2E-04	0.03	0.20	32.7	11.5	1	217.5	106.1	64.0	0.73	88.8	9.7	118.0	12.9		
	4	9.8E-10	0.02	4.2	1.7E-04	0.02	0.37	67.1	18.9	1	167.5	114.2	63.9	0.77	73.0	8.0	97.9	10.7		
	5	1.5E-09	0.06	7.8	4.4E-04	0.06	0.36	46.8	18.8	2	203.2	123.4	71.0	0.78	86.2	12.4	110.9	15.9		
	6	4.4E-09	0.07	5.9	4.8E-04	0.04	1.35	121.4	34.5	1	189.8	152.5	81.6	0.80	93.8	13.8	117.2	17.3		
	7	1.1E-09	0.02	3.2	1.1E-04	0.02	0.29	59.7	17.3	1	173.6	105.2	60.6	0.73	98.5	10.6	134.9	14.6		
	9	1.4E-09	0.06	4.3	4.7E-04	0.03	0.25	16.5	7.6	1	169.5	187.8	90.6	0.83	95.1	13.4	114.8	16.2		
SA12-38	10	7.1E-10	0.02	5.5	1.2E-04	0.03	0.27	92.2	25.5	1	171.4	82.6	49.9	0.67	72.7	10.7	107.9	15.9		
	11	4.2E-09	0.08	4.2	5.6E-04	0.02	0.45	24.3	8.9	1	275.9	163.1	94.4	0.83	170.9	18.6	205.2	22.3		
	13	4.2E-09	0.05	7.4	3.8E-04	0.05	1.26	179.0	49.5	1	193.7	120.4	68.9	0.76	87.1	9.3	114.3	12.3		
	16	1.8E-09	0.03	5.1	2.0E-04	0.04	0.75	134.9	36.8	2	212.9	114.2	67.6	0.76	70.7	7.8	96.6	10.6		
	1	2.4E-09	0.16	19.0	1.1E-03	0.14	0.10	11.9	0.91	110.3	22.0	1	169.2	139.0	73.9	0.80	106.8	11.5	133.0	14.4
	2	3.3E-09	0.20	25.6	1.4E-03	0.19	0.28	36.5	1.20	156.9	34.4	1	154.1	140.7	72.4	0.79	100.3	10.8	126.3	13.6
	3	1.4E-09	0.09	21.9	6.3E-04	0.16	0.15	36.7	0.57	142.6	30.7	2	142.1	105.6	57.7	0.74	89.5	9.8	120.9	13.3
	4	6.3E-09	0.07	6.0	5.4E-04	0.04	1.84	149.3	0.86	69.7	41.2	2	277.1	133.0	80.5	0.80	100.2	11.3	125.9	14.2
	5	8.1E-09	0.51	26.1	3.7E-03	0.19	0.39	19.8	2.10	107.4	30.9	1	237.1	181.0	98.2	0.85	106.6	14.5	125.2	17.0
	6	5.4E-09	0.21	26.0	1.5E-03	0.19	0.61	75.0	1.01	124.2	43.8	1	156.3	143.9	73.9	0.79	120.4	16.8	152.0	21.2
	7	2.6E-09	0.16	18.7	1.2E-03	0.14	0.20	23.8	1.33	155.9	24.4	2	230.2	121.6	72.1	0.79	95.6	10.5	120.4	13.2
	8	3.8E-09	0.21	31.3	1.5E-03	0.23	0.10	14.4	34.9	0	160.5	129.7	69.3	0.79	130.3	17.9	164.6	22.7		
	9	7.5E-09	0.53	41.5	3.8E-03	0.30	0.27	21.5	46.9	0	223.6	150.5	84.4	0.83	103.8	14.2	125.3	17.2		
	10	2.5E-09	0.19	31.1	1.3E-03	0.23	0.17	28.3	37.9	2	210.2	106.2	63.6	0.77	88.4	9.7	115.0	12.6		
	11	6.3E-09	0.38	34.3	2.7E-03	0.25	0.24	22.1	1.63	148.0	39.8	2	233.7	137.0	79.4	0.82	114.0	12.5	139.6	15.3
	12	6.3E-09	0.27	48.8	1.9E-03	0.35	0.49	89.2	0.91	165.9	70.1	1	145.7	122.5	64.7	0.77	131.6	18.0	171.6	23.5

<sup>a</sup>Analytical details can be found in Text S4. For details on sample lithology see Table S8.<sup>b</sup>eU (effective uranium) is calculated as eUppm = [Uppm] + (0.235\*(Thppm)).<sup>c</sup>T = Number of terminations identified on crystal.<sup>d</sup>L and W = length and width of crystal or crystal fragment.<sup>e</sup>R\* = spherical equivalent radius calculated as  $R^* = (3^*(RL))/(2^*(R + L))$  where  $R = W/2$ .<sup>f</sup>Correction factor after Farley et al. [1996], assuming homogeneous distribution U and Th.<sup>g</sup>Estimate uncertainty is equal to 1σ analytical uncertainty, which includes error propagated from U, Th, Sm, and He measurement uncertainties, plus an additional 10% which is the standard deviation (reproducibility) of repeat analysis of Durango apatite standards.<sup>h</sup>Corrected AHe age = raw AHe age/Ft.



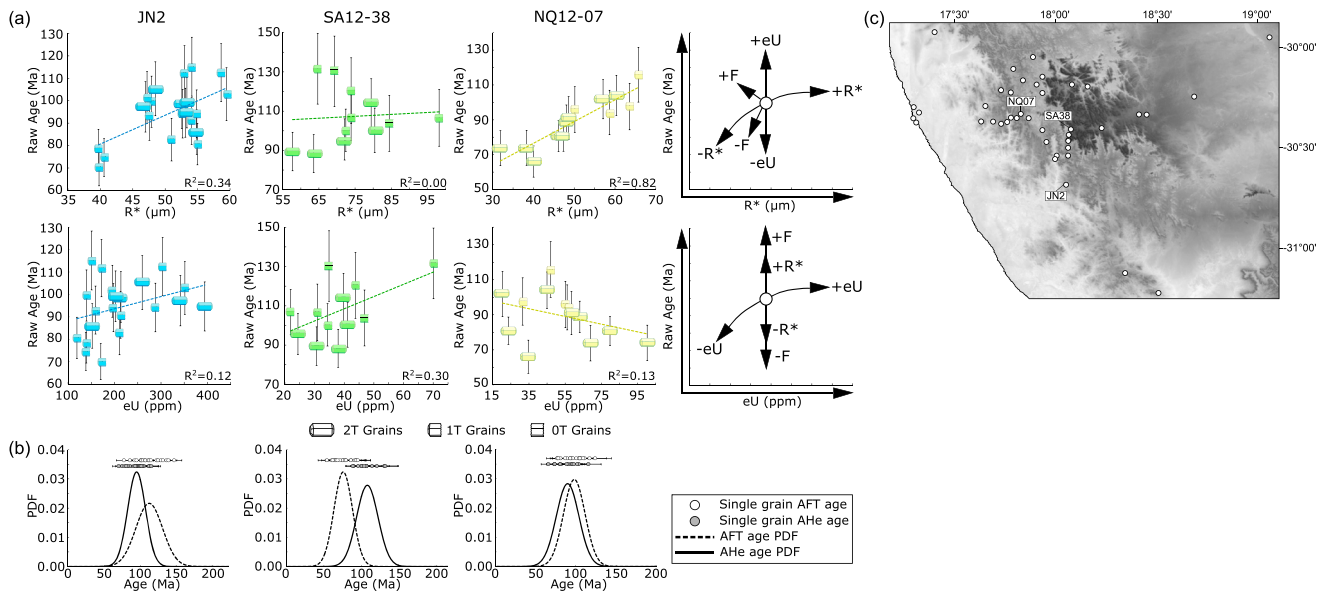


**Figure 4.** (a) Relationships of AHe age (uncorrected) against spherical equivalent radius ( $R^*$ ) (top row) and against effective uranium ( $eU = [U] + [0.235 \cdot Th]$ ). All uncertainties include  $1\sigma$  analytical uncertainty plus an additional 10% uncertainty observed in the dispersion of Durango standards analyzed. The two plots in the final column are cartoons illustrating the relative influence on AHe ages by the different factors causing natural AHe single-grain age dispersion ( $R^*$  = spherical equivalent radius;  $eU$  = effective uranium; and  $F$  = crystal fragment length) [after Brown *et al.*, 2013]. The competing influence of all dispersion contributors perturbs simple 2-D relationships. Age increases with increasing  $eU$  and  $R^*$ . Larger fragment lengths of broken crystals are typically older than small fragment lengths. (b) Probability density functions of a normal distribution centered on the mean AFT and mean AHe age with  $1\sigma$  the standard deviation on the mean. (c) Location map of samples used for dispersion plots.

Plots of  $eU$  versus single-grain age are more complex, and different samples show correlations that are positive, negative, or entirely absent. However, a simple linear correlation between  $eU$  and grain age should be not expected even for “well-” behaved samples, because the effect of radiation damage accumulation and annealing is not linear, and it is dependent on the thermal history. For example, Flowers *et al.* [2009] report that for relatively slow cooling rates (approximately  $0.1\text{--}1^\circ\text{C/Myr}$ ), the age- $eU$  relationship will first be positively correlated but will then plateau above  $eU$  concentrations of approximately 50 ppm. Our understanding of how the accumulation and annealing of radiation defects occur, and the impact this has on alpha trapping and helium diffusion, is still developing [Gautheron *et al.*, 2013; Mbongo-Djimbi *et al.*, 2015]. Expecting to observe simple correlations in single-grain ages and  $eU$  may also be ambitious considering that grain radius and the presence of fragmented grains influence the effective closure temperature and preservation of the He diffusion profile within grains, respectively. However, we emphasize that the observed intersample grain age dispersion is likely a real and natural effect that contains useful information about the sample’s thermal history irrespective of whether the simple 2-D plots of grain age versus  $eU$  and  $R^*$  show clear correlations or not [Flowers and Kelley, 2011; Brown *et al.*, 2013].

Other factors that can cause single-grain age dispersion (Table 3) must also be considered though, such as the possible presence of U and Th zonation [Flowers and Kelley, 2011; Ault and Flowers, 2012; Farley *et al.*, 2011], unidentified U- and Th-bearing inclusions [House *et al.*, 1997; Stockli *et al.*, 2000; Fitzgerald *et al.*, 2006; Vermeesch *et al.*, 2007], implantation [Farley *et al.*, 1996; Spiegel *et al.*, 2009; Gautheron *et al.*, 2012], the contribution of Sm [Hansen and Reiners, 2006; Vermeesch, 2008], and the dominant influence of the thermal history of the sample in controlling He diffusion.

### 3.3. Summary of Joint AFT and AHe Data

The AFT data presented here include AFT ages that range from the Early Cretaceous to early Cenozoic with moderate to long MTLs (approximately  $13\text{ }\mu\text{m}$ ) and track length distributions that are generally narrow to moderately broad (standard deviation  $0.97$  to  $1.95\text{ }\mu\text{m}$ ). The qualitative relationship of the track length and AFT age data indicates that the dominant phase of crustal cooling occurred throughout the Cretaceous. However, only by using inverse modeling can we resolve the temporal and spatial variability of crustal cooling across the study area.

**Table 3.** Summary of the Different Factors That Contribute to Single-Grain AHe Age Dispersion and the Estimated Magnitude of Dispersion Introduced by Each of These Factors

Dispersion Factor	Contribution to Dispersion	Comments	References
Grain size ( $R^*$ )	$\pm 50$ –100%	$R^*$ of approximately 50–100 $\mu\text{m}$ , depending on the thermal history	<i>Reiners and Farley</i> [2001] and <i>Brown et al.</i> [2013]
Radiation Damage (eU)	$\pm 50$ –100%	Depending on thermal history and difference in the eU, content of individual grains can exceed 200%.	<i>Gautheron et al.</i> [2009], <i>Flowers et al.</i> [2009], and <i>Brown et al.</i> [2013]
Fragment length	$\pm 7$ –60%	Depending on length of fragment and original position of fragment relative to the whole grain.	<i>Brown et al.</i> [2013]
Zonation	$\pm 10$ –15%	30–40% dispersion for some thermal histories and extreme heterogeneity, true age may be older or younger depending on whether the crystal has an enriched core or rim, respectively.	<i>Meesters and Dunai</i> [2002a], <i>Fitzgerald et al.</i> [2006], <i>Farley et al.</i> [2011], and <i>Ault and Flowers</i> [2012]
Implantation	older by 60%	Effect will vary depending on the size of “bad neighbor,” [U] and [Th] content of bad neighbor, and whether or not the apatite is in contact with one or many bad neighbors.	<i>Spiegel et al.</i> [2009] and <i>Gautheron et al.</i> [2012]
Alpha ejection factor (Ft)	older age by 3–8%	Depending on thermal history and zonation patterns	<i>Meesters and Dunai</i> [2002a, 2002b], <i>Gautheron et al.</i> [2012], and <i>Brown et al.</i> [2013]
Sm	0.1–10%	In certain situations (low [U] and [Th], anomalously high [Sm]) can exceed 25%.	<i>Fitzgerald et al.</i> [2006] and <i>Vermeesch et al.</i> [2008]
Mineral inclusions	older by <10%	More than a few percent only when inclusions are quite large (<0.1 of the grain size) and/or have an unusually high U and Th content (i.e., >1000 times that of the apatite).	<i>Vermeesch et al.</i> [2007]

In general, the AHe ages are in agreement with AFT ages in that they are predominantly Early Cretaceous to early Cenozoic. It is not uncommon to observe AHe ages equal to or exceeding their corresponding AFT ages [*Hendriks and Redfield*, 2005; *Fitzgerald et al.*, 2006; *Green and Duddy*, 2006; *Flowers and Kelley*, 2011; *Danišik et al.*, 2012; *Ksienzyk et al.*, 2014] for reasons discussed above. Only three samples have mean AHe ages that are older and do not overlap within the uncertainty of the mean AFT age (Figure 3c).

When comparing mean sample AHe ages with mean (or central or pooled) sample AFT ages, it is not clear what meaning to ascribe to any differences in these values because of the wide range of factors that affect single-grain ages in both systems. For many cases, where a sample has experienced a protracted low-temperature thermal history, it would be expected that some single grains yield AFT ages older than AHe and also the reverse, depending on the relative eU, grain size, and CI composition of the different grains. Large, U-, Th-, and F-rich grains may yield old AHe ages and young AFT ages, whereas small, U-poor, Th-poor, but CI-rich grains may yield young AHe ages and old AFT ages. For this reason, we present and examine the single-grain date distributions of both methods to try and avoid problems that may arise from interpreting sample mean ages directly (Figure 4b and Text S6).

If a sample yields concordant mean AHe and mean AFT ages, this is often interpreted as indicative of a sample cooling rapidly through both the partial annealing zone (PAZ) and partial retention zone at a time indicated by the measured ages. However, because AFT and AHe analyses are not performed on the same grains, and the thermal sensitivity of each grain is different due to different grain sizes and compositions, it does not necessarily follow that concordant mean sample ages indicate rapid cooling at that time. For the same reasons, samples having AFT and AHe data that appear at first complex, or even incompatible, may well contain coherent, useful thermal history information once the real uncertainties on each measurement are formally acknowledged and accounted for when modeling the data.

## 4. Thermal History Inversion

### 4.1. Approach

In this study, QTQt, a Bayesian transdimensional approach to data inversion, as described in detail by *Gallagher* [2012], is used for the inference of thermal history models. Fission track ages and track length data are modeled using the multikinetic fission track annealing model of *Ketcham et al.* [2007]. For samples that also have AHe data, all single-grain ages are jointly inverted alongside the corresponding fission track data

using the model and parameters of *Gautheron et al.* [2009], which accounts for the effect of radiation damage accumulation and its annealing on He diffusion.

The Bayesian method requires us to define the model space as a prior probability distribution (i.e., range of temperature and time over which to search). The model space is then sampled using a MCMC approach [e.g., *Gilks*, 2005; *Sambridge et al.*, 2006; *Gallagher et al.*, 2009], whereby the current model is perturbed to produce a proposed model. This model is then accepted or rejected based on a combination of the data fit (likelihood) of the proposed model and the prior probability, relative to the same measures for the current model. The transdimensional Bayesian aspect of the modeling technique penalizes complex models proposed during sampling in favor of models with fewer  $T$ - $t$  points that adequately fit the observed data. An additional novel aspect of QTQt is the ability to model samples from vertical profiles together. This function is also employed below for a subset of samples that form an “elevation profile” over a relatively short distance of approximately 10 km. Such a multisample profile inversion also incorporates an additional model parameter representing the temperature difference or offset between the top and bottom samples, with a prior determined by an assumed range for the geothermal gradient.

The MCMC algorithm was run for a minimum of approximately 200,000 iterations after discarding an initial approximately 50,000 “burn in” runs [see *Gallagher et al.*, 2009]. In most cases, however, the number of runs far exceeds this as short approximately 10,000 iteration runs are performed in order to choose appropriate values for the MCMC search parameters before performing longer runs. This choice is based on the acceptance rates of proposed model parameters (being between 20 and 60%) and the parameter sampling being stationary (i.e., no obvious trends as a function of iteration). The output of the Bayesian approach is an ensemble of accepted thermal history models, each with an associated posterior probability. From this collection of thermal histories, a mean thermal history model (weighted by the posterior probability of each individual thermal history), termed the expected model, is produced with 95% credible intervals that provide the uncertainty on the model. The nature of the expected model is that it will retain well-constrained features (i.e., features common to many individual models) while more complex deviations observed in only a small number of viable models are averaged out. The expected model, and its associated uncertainty measures, provides the most robust albeit conservative insight to the overall thermal history of the sample.

#### 4.2. Additional Model Constraints

For each sample, the oldest sample age (i.e., the AFT age or oldest AHe single-grain age for the sample) is used to define the center of a uniform prior on time, with a range of plus/minus oldest sample age. The prior information on temperature range was centered on 70°C with a range of  $\pm 70^\circ\text{C}$ . The number of time-temperature points sampled from this prior is allowed to vary from 2 (including the present data temperature) to 50. The thermal history is constructed by interpolating linearly between these sampled time-temperature points. This sampling strategy imposes no constraints about the form of the thermal history (e.g., monotonic cooling), but the form is determined by the data themselves. Additional prior information, if available from geological constraints, can be entered in a similar manner as a range of time and temperature. All samples from this region are outcrop samples taken from basement lithologies apart from SA12-27, which was collected from a boulder clast of basement origin from within the glacial tillite of the Permian Dwyka Group. During modeling, SA12-27 was assigned a specific initial constraint of  $300 \pm 10$  Ma,  $5 \pm 5^\circ\text{C}$  to represent that the sample was at the surface at this time. For basement samples, an initial constraint of  $550 \pm 50$  Ma and  $100 \pm 100^\circ\text{C}$  was used to reflect the uncertainty surrounding the paleotemperature of the sample during the Pan-African Orogeny. For each model, only the post-300 Ma thermal history is presented. Before 300 Ma, thermal history models are unconstrained because the data require that all sample temperatures are close to or above the base of the apatite PAZ (i.e., approximately  $110 \pm 10^\circ\text{C}$ ) prior to cooling in the Mesozoic. The present-day temperature value is assumed to be  $20 \pm 10^\circ\text{C}$  for all samples.

A lack of geological information limits the amount of postrift constraints that can be added to the models. However, the implications of sporadic fossil evidence, sedimentary deposits, and igneous intrusions across the region on nearby samples are also investigated. The thermal history for the cluster of samples collected at Hondeklip Bay can be constrained using fossil evidence in thin sedimentary formations that overlie the Namaqua Metamorphic Province rocks across the coastal plain. Fossil hominoid teeth from the marine sand Alexander Bay Formation assign an early Miocene age to the deposit [*Senut et al.*, 1997]. The Alexander Bay Formation overlies the calcified and silicified gravels and sandstones of the Koignass Formation, which

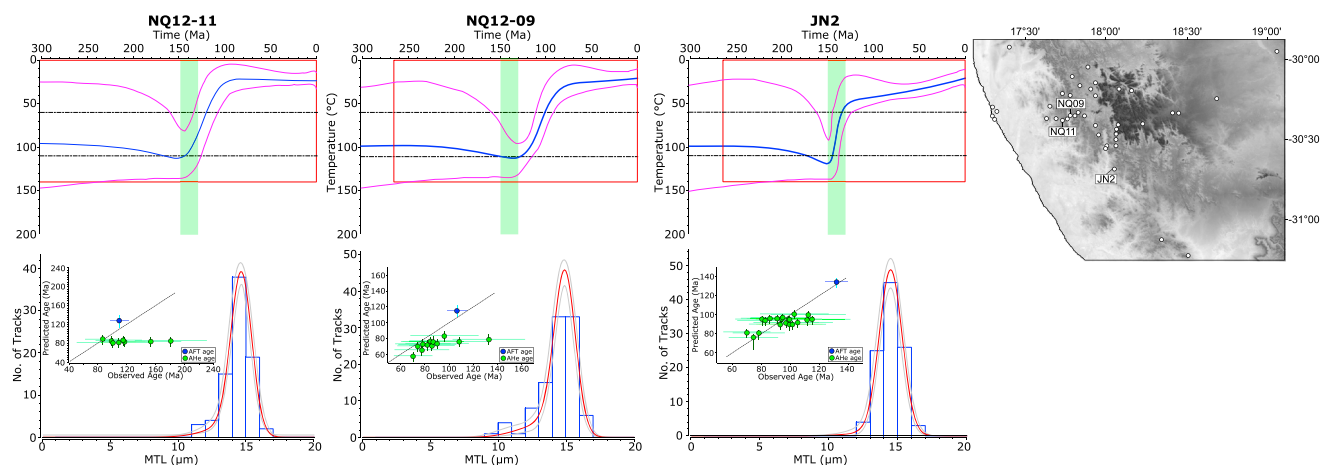


**Figure 5.** Thermal history modeling results for three samples from the Namaqualand Highlands highlighting Early Cretaceous cooling (top row), their data predictions (bottom row), and their location on the topographic map of the study area. In Figure 5 (top row), blue line shows the expected model (i.e., average of all models weighted for their posterior probability); magenta lines indicate 95% credible intervals for the expected model. Red box indicates the prior information on temperature and time. Green box is used to indicate the timing of the synrift cooling episode predicted across the entire margin (i.e., approximately 150–130 Ma). Figure 5 (bottom row) shows the observed track length distributions; red curve indicates the predicted track length distributions, and grey curves indicate 95% credible intervals (i.e., uncertainty) for track length distribution prediction. Inset plot shows the relationship of observed data against model-predicted data; green circles represent single-grain AHe ages, and blue circles represent AFT ages.

is presumed to have been deposited in a fluvial environment during a late Oligocene to early Miocene marine regression [de Beer, 2010]. Coastal samples are therefore assigned an additional constraint of  $20 \pm 10$  Ma,  $20 \pm 10^\circ\text{C}$  to reflect near-surface temperatures of the basement rock prior to deposition of these Cenozoic deposits.

Sediments in and around the Vaalputs area and fossiliferous crater lake sediments preserved in the Gamoep intrusive suite, and in particular the Arnot pipe at Banke Farm (Figures 1 and 2), provide Late Mesozoic and Cenozoic constraints for samples on the plateau. The Dasdap and Vaalputs sediments are proposed to be Late Cretaceous to early Paleocene in age. This age is supported by palynological evidence dated at 71 to 64 Ma [Scholtz, 1985] and preservation of fossilized frogs and wood in clay deposits [Adamson, 1931; Haughton, 1931]. Estes [1977] reported younger pollen and fossil leaf evidence from the same lacustrine sediments aged from the late Eocene to early Oligocene. A constraint box of  $50 \pm 20$  Ma,  $20 \pm 10^\circ\text{C}$  was included for samples SA12-51, SA12-52, and SA12-27.

### 4.3. Results

#### 4.3.1. Early Cretaceous Cooling Histories

A signal of Early Cretaceous cooling is evident in many samples across the study area. Figure 5 shows representative thermal histories of this form (see Figure S7 for all thermal history models). The path of the expected thermal history indicates cooling through the PAZ beginning at approximately 150–130 Ma and reaches near-surface temperatures by approximately 50–30 Ma (Figure 5, top and bottom rows). Due to the unconstrained initial conditions of the model, it is unclear whether the sample was already undergoing cooling or still being heated prior to the cooling episode predicted by the model. Cooling rates for the main phase of cooling predicted by these thermal histories are approximately 0.5–2.5°C/Myr, over a period of approximately 50 Myr (150–100 Myr).

More rapid cooling during the Early Cretaceous (approximately 150–130 Ma) time interval is rarely observed. However, in occasional samples (e.g., JN2, Figure 5, right figure), cooling rates of approximately 4.5–5.5°C/Myr over a 10 Myr period are predicted. Following this period of rapid cooling, the cooling rate rapidly decreases to approximately 0.2–0.3°C/Myr during the Late Cretaceous and is maintained through the Cenozoic. These models imply that crustal cooling persisted throughout the Early Cretaceous across the entire margin, predominantly at a moderate and steady rate, although local variations exist. A consistent observation is that near-surface temperatures ( $\leq 40^\circ\text{C}$ ) were reached and maintained by the early Cenozoic.

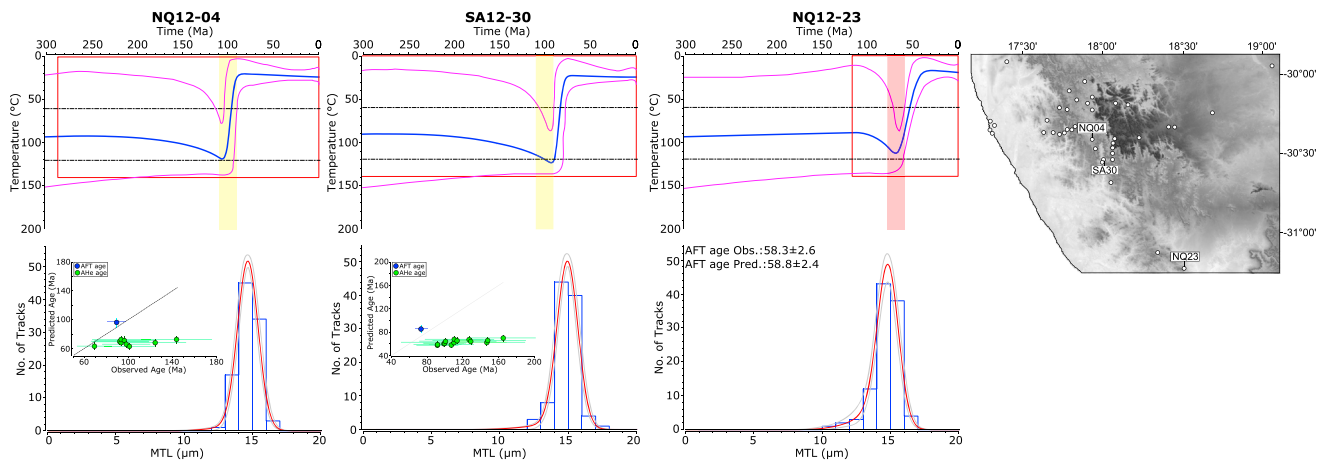


**Figure 6.** Thermal history modeling results for three samples from the Namaqualand Highlands highlighting middle-Late Cretaceous cooling (top row), their data predictions (bottom row), and their location on the topographic map of the study area. In Figure 6 (top row), blue line shows the expected model (i.e., average of all models weighted for their posterior probability); magenta lines indicate 95% credible intervals for the expected model. Red box indicates the prior information on temperature and time. Yellow and red boxes are used to indicate the timing of the postrift cooling episodes: approximately 110–90 Ma (structurally controlled denudation across the entire margin and regional denudation of the interior plateau) and approximately 80–60 Ma (structurally controlled denudation, potentially caused by compression-driven inversion in parts of South Africa and in Namibia), respectively. Figure 6 (bottom row) shows the observed track length distributions; red curve indicates the predicted track length distributions, and grey curves indicate 95% credible intervals (i.e., uncertainty) for track length distributions prediction. Inset plot shows the relationship of observed data against model-predicted data; green circles represent single-grain AHe ages, and blue circles represent AFT age.

#### 4.3.2. Late Cretaceous Cooling Histories

Cooling initiating during the middle-Late Cretaceous (approximately 110–90 Ma) time interval, characterized by rapid cooling rates, is the dominant style of thermal history across the margin (e.g., Figure 6 (top and bottom rows); see Text S7). Cooling rates generally range from approximately 1.5–5°C/Myr but in certain samples can be higher at 7.4–8.1°C/Myr (e.g., NQ12-04). Following rapid cooling during the Late Cretaceous, samples are predicted to reside at temperatures  $\leq 40^{\circ}\text{C}$  and cool steadily through the Cenozoic toward present-day surface temperatures. As these samples cooled from temperatures of approximately  $110 \pm 10^{\circ}\text{C}$  during the Late Cretaceous, any record of earlier cooling (i.e., the Early Cretaceous cooling history described above) is not preserved. The absence of a Late Cretaceous pulse of cooling in “Early Cretaceous cooling histories” could be due to a lack of information in the data, meaning that the approach adopted by QTQt does not need or cannot resolve a two-stage cooling history from the available data. However, we interpret the monotonic Early Cretaceous thermal histories as a real feature with geological significance, as it is the most probable cooling path given the data available, and any alternative would involve forcing the model to satisfy a preferred thermal history.

A second Late Cretaceous cooling episode is poorly preserved but is present in the study area. The thermal history for one sample clearly shows cooling initiating at between 70 and 65 Ma (Figure 6, right figure). The style of cooling for NQ12-23 is very rapid, occurring at a rate of 10°C/Myr. This sample resides in a complex structural setting and is approximately 50 km SW of the Koegel Fontein igneous complex, which has intrusive bodies dated to approximately 70–50 Ma [de Beer, 2002]. Fission track data for this sample are robust with a large number of track lengths and single-grain ages. The regional significance of this cooling history cannot be inferred from this sample alone and is therefore discussed in more detail below alongside other regional AFT data.

#### 4.3.3. Multisample Inversion

A subset of samples, composed of eight outcrop samples from the western flank of the “Kamiesberg Mountain,” including two samples from the data set of Wildman *et al.* [2015], covers an elevation range of 1220 m and is separated by a distance of less than 10 km (north to south) and 5 km (east to west) (Figure 7). Data from these samples are treated as an elevation profile and are modeled together as described in section 4.1. Contrary to the expected relationship of AFT age and elevation, the oldest AFT ages in this profile are at the base. As expected, these samples have the poorest data fit when all samples in the profile are modeled together (Figure 7, left column). To resolve this issue, the profile is better split into (i) a lower profile consisting of three samples with AFT ages of approximately 115 Ma (Figure 7, middle column) and (ii) an upper profile consisting of



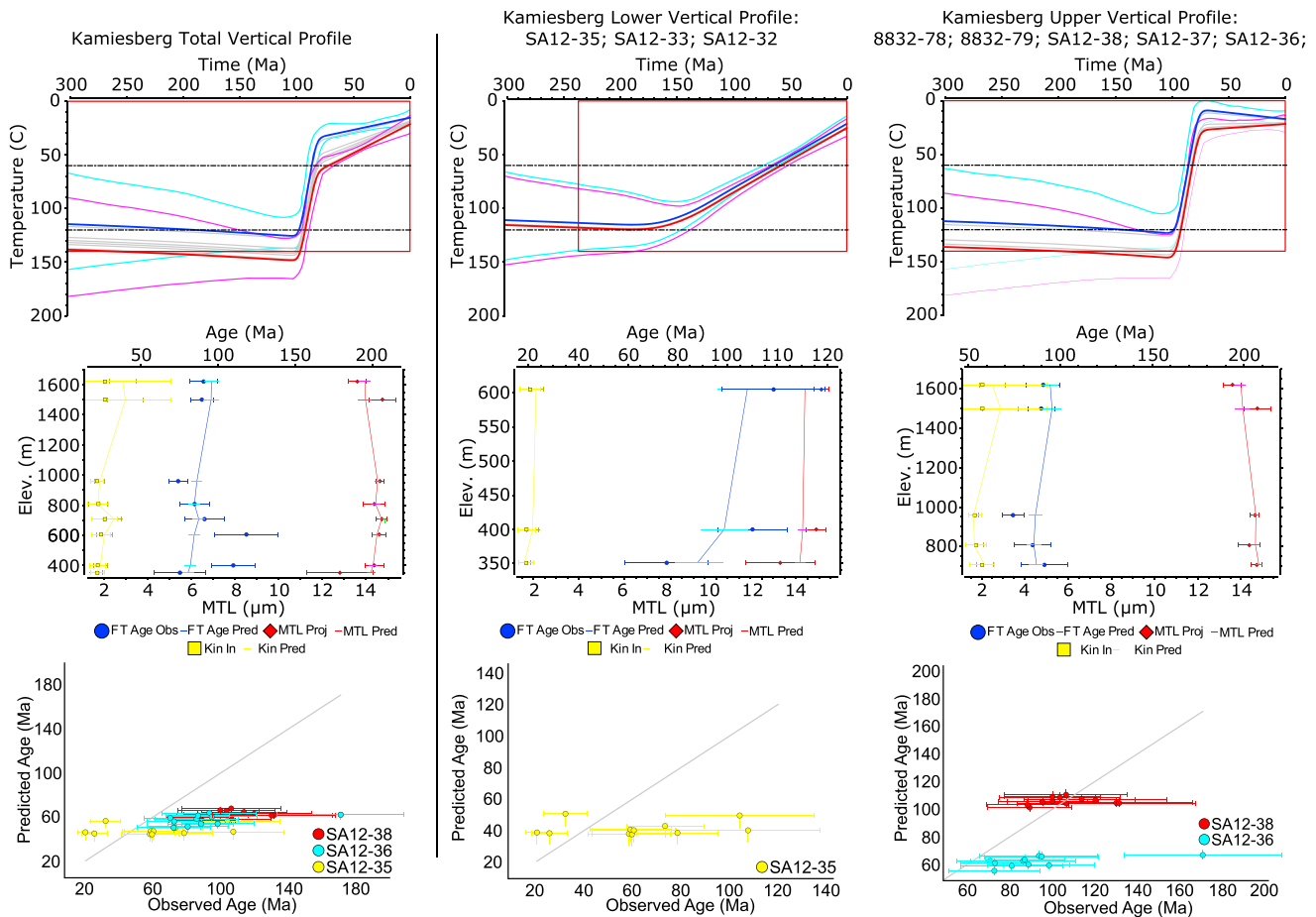


**Figure 7.** Thermal history modeling results for an elevation profile of (top row) samples in the Namaqualand Highlands and (bottom row) their data predictions. In Figure 7 (top row), blue line shows the expected model (i.e., average of all models weighted for their posterior probability) for the upper sample; red lines show the expected model for the bottom sample in the profile; and grey lines show expected model for intervening samples. Cyan and magenta lines indicate 95% credible intervals for the top and bottom sample expected model, respectively. Red box indicates the prior information on temperature and time. (middle and bottom rows) model predictions. Legend for data prediction plots can be found in the figure.

five AFT ages that are approximately 90 Ma (Figure 7, right column). A rapidly cooled, tightly constrained cooling event at approximately 110–90 Ma is defined for the upper profile, while a slower cooling history initiating at approximately 150–130 Ma is defined for the lower profile. As the age-elevation relationship of the entire profile is inconsistent with that of a profile sampled from a single coherent block and the data are better reproduced by two distinct thermal histories, it is possible that displacement on an unmapped fault has resulted in the lower profile (i.e., down-thrown block) retaining thermal history information from the synrift period while the upper profile (i.e., up-thrown block) has cooled during later erosion.

It is difficult to reproduce all of the single-grain AHe ages for samples in the elevation profile regardless of whether the data are modeled as a single profile or two profiles. In fact, for most models with AHe data, it is predominantly the younger AHe single-grain ages that are predicted best. The poor fit of the AHe data relative to that of AFT data is likely to be due to a combination of our limited understanding of the He system and the treatment of the data in the modeling approach to compensate for this. Although we have attempted to account for both grain size and radiation damage effects, the latter is still not ideally parameterized, particularly for high eU samples and potentially for additional compositional heterogeneity [Gautheron *et al.*, 2013; Mbongo-Djimbi *et al.*, 2015]. Moreover, the effect of other factors that could produce observed AHe ages that were “too old” (e.g., grain fragmentation, zonation, and implantation) is unaccounted for and may, in the future, improve data fits. For this reason, less weight was placed on AHe ages, by assigning an uncertainty to AHe single-grain ages greater than the analytical uncertainty and allowing the AHe single-grain age to be resampled from this uncertainty range.

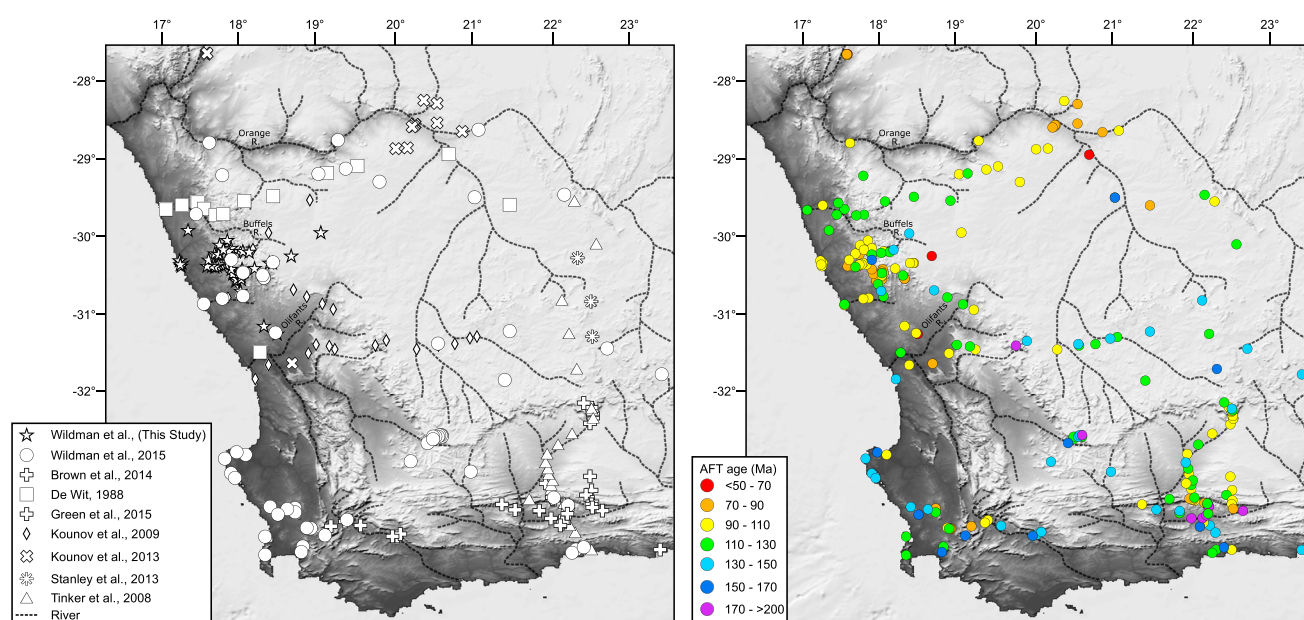


**Figure 8.** Location map of published low-temperature thermochronology data for southwest Africa: AFT data only [Wildman *et al.*, 2015; Green *et al.*, 2015; Brown *et al.*, 2014; Kounov *et al.*, 2009; Tinker *et al.*, 2008a; de Wit, 1998], AHe data only [Stanley *et al.*, 2013], and AFT and AHe data (Wildman *et al.* (this study)) [Kounov *et al.*, 2013]. Drainage network taken from Dollar [1998].

## 5. Timing and Mechanisms of Crustal Cooling

### 5.1. AFT and AHe Data From the SW African Continental Margin and Interior Plateau

Aside from new AFT data presented in this study and previously published by the same authors [e.g., Brown *et al.*, 1990; Wildman *et al.*, 2015], AFT analysis in the Namaqualand region has been limited (Figure 8). Data from Kounov *et al.* [2009] consists of two transects across the Namaqualand continental margin and extend onto the inland plateau (Figure 8). Combining all available data sets provides an extremely detailed low-temperature thermochronology database across this sector of the margin by improving the regional and local sample coverage as well as improving the temporal resolution by including AHe analysis.

Data from earlier studies are largely consistent with the new data presented here. AFT ages are generally Early to Late Cretaceous with moderate to long MTLs. The exceptions to this are one sample of Late Jurassic age reported by Wildman *et al.* [2015] (8732-46) in the heart of the Namaqualand Highlands and an Early Jurassic age recorded by Kounov *et al.* [2009] from their southern transect near the town Calvinia. Kounov *et al.* [2009] propose that inverse modeling of their data supports a two-stage thermal history across the margin. The major phase of cooling is ascribed to the mid-Cretaceous (115–90 Ma) and is attributed to a tectonically induced period of enhanced denudation. Moreover, they suggest that discrete fault block reactivation during this time results in differential denudation over major structures. The earlier event was driven by either rift-related tectonic denudation or thermal relaxation of the surface following widespread Karoo magmatism at approximately 180 Ma [Jourdan *et al.*, 2005]. Kounov *et al.* [2009] give preference to the latter mechanism, as this cooling episode is only recorded in samples from the plateau region of the southern transect that were collected in the Karoo basin. However, data from Brown *et al.* [1990] and Wildman *et al.* [2015] and data presented here clearly preserved a record of Early Cretaceous cooling across the coastal plain, escarpment zone, and plateau. Moreover, offshore sediment volume analysis has predicted synrift sediment accumulation in offshore basins at this time [Guillocheau *et al.*, 2012] (see section 6.1). Although a thermal effect of the Karoo may have contributed to the recorded thermal history, an erosional response to rifting is likely to have been a major factor.

The latest Jurassic to Early Cretaceous cooling at approximately 160–130 Ma is recorded regionally but preserved only locally. The discrete, structurally controlled nature of the second cooling event from 115 to 90 Ma across the margin is somewhat poorly constrained by Kounov *et al.* [2009], due to the uncertainty in their fission track data and uncertainties in models. The distinction of these two cooling episode is much more prominent in our study through the combination of AFT and AHe analysis and high-resolution sampling.

Evidence for a 110–90 Ma cooling event spanning the entire subcontinent of South Africa can be found in (i) AFT data from the southwestern cape [Wildman *et al.*, 2015], southern margin [Tinker *et al.*, 2008a; Green *et al.*, 2015], southeastern margin [Brown *et al.*, 2002], and along the southern Orange River valley [de Wit, 1988]; (ii) AHe data from the southeastern Kaapvaal Craton [Flowers and Schoene, 2010] and from samples collected from kimberlites on the South African Plateau [Stanley *et al.*, 2013]; and (iii) a joint AFT and AHe study from the Augrabies Falls and Fish River Canyon along the Orange River [Kounov *et al.*, 2013] (Figure 8).

AFT or AHe data advocating a Late Cretaceous to early Cenozoic (or even younger) cooling event is still limited despite the growing number of studies occurring in single-outcrop samples, if at all [e.g., de Wit, 1988; Kounov *et al.*, 2013]. However, in northern Namibia, many AFT ages of approximately 60–80 Ma are widely observed on the coastal plain as well as penetrating well inland [Raab *et al.*, 2002; Brown *et al.*, 2014]. These AFT ages agree with the single early Cenozoic AFT age presented here, implying that structurally controlled denudation in Namibia may have also been manifested in parts of Southern Africa. AFT data are used by Green *et al.* [2015] to infer that parts of the southern margin, particularly the southwestern cape, have cooled from approximately 60–70°C since 30 Myr. This cooling equates to approximately 1.5 to 2.5 km of denudation for a geothermal gradient of 20 to 25°C/km, which is greater than the estimates derived from other data sets from the region (approximately 1–1.5 km) [Tinker *et al.*, 2008a; Stanley *et al.*, 2013; Wildman *et al.*, 2015]. Although local variations in the amount of Cenozoic denudation may exist, Green *et al.* [2015] utilize a different modeling approach and geological framework for interpreting their data [e.g., Green *et al.*, 2013]. While our Bayesian approach yields simple cooling histories that adequately fit the data without invoking unconstrained geological events, Green *et al.* [2015] use likelihood theory [Gallagher, 1995] and a modeling procedure that explicitly seeks discrete temperature maxima and thus invariably produces thermal histories with multiple discrete episodes of inferred burial and erosion.

## 5.2. Timing and Spatial Patterns of Denudation

The last major thermal event expressed regionally across Southern Africa is the emplacement of the Karoo igneous intrusions and continental flood basalts at approximately 182–183 Ma [Svensen *et al.*, 2012]. Evidence of younger igneous bodies in Southern Africa is found in the form of localized alkaline intrusive pipes emplaced during the Late Cretaceous and early Cenozoic [Moore and Verwoerd, 1985; de Beer, 2010; Curtis *et al.*, 2013]. In Namibia, Early Cretaceous flood basalts are preserved as part of the Parana-Etendeka igneous province dated at approximately 130 Ma [Reid *et al.*, 1990; Reid and Rex, 1994]. However, due to the lack of any preservation in South Africa, their southern extent is unknown. The lack of significant thermal activity following the Jurassic combined with the coherence of the timing of cooling with peaks in offshore sediment accumulation in the offshore basin [Rouby *et al.*, 2009; Guillocheau *et al.*, 2012; Wildman *et al.*, 2015] suggests that cooling was primarily driven by onshore denudation.

We performed simple calculations of the amount of denudation required to drive cooling over distinct time intervals:  $D_{t_0-t_1} = (\Delta T_{t_0-t_1})/G$ , where  $D$  is the estimate of denudation over the desired time interval ( $t_0 - t_1$ ) and  $G$  is the estimated geothermal gradient. The amount of denudation required to cool the sample from elevated temperatures to surface temperatures depends on the geothermal gradient of the region. Present-day geothermal gradients across much of Southern Africa are approximately 20–25°C/km [Ballard and Pollack, 1987; Jones, 1987]. Maintaining the conservative approach adopted during modeling, the upper limit of this temperature range (i.e., 25°C/km) was assumed to best represent the paleogeothermal gradient. The influence of geothermal gradient on denudation estimates is nonlinear and most significant for low geothermal gradients. A low geothermal gradient is unlikely to be the case in the study area as the basement rocks are particularly enriched in heat-producing radiogenic elements (U, Th, and K) [Andreoli *et al.*, 2006], which will have helped to maintain moderate-high heat flow values across the Namaqualand Highlands [Jones, 1987; Andreoli *et al.*, 2006].

Estimates of denudation are made using the expected thermal history model and assuming a geothermal gradient of 25°C/km. Figure 9 shows three coast-perpendicular transects highlighting the spatial patterns of denudation over major time intervals. The timing for the onset of cooling that is predicted by sample thermal histories is only recorded when the sample cools below approximately 110°C. Therefore, in cases where much of the early portion of the thermal history is unconstrained, cooling and the mechanism driving cooling may have been ongoing prior to the predicted onset of cooling. Estimates of denudation for a particular time interval should be consulted alongside the thermal history and assessed in terms of how well the thermal history is constrained at this time.





During the Early Cretaceous (approximately 150–110 Ma) total denudation is generally between 1 and 2 km and appears to be fairly consistent across the length of the transect. However, as many samples do not record cooling until the Late Cretaceous, fewer samples can be used to estimate earlier denudation. Two samples along transect YY' predict estimates of approximately 4 km of denudation in the Early Cretaceous with approximately 2 km occurring during the 150–130 Ma interval. Localized zones of higher denudation at this time may have been a result of a variable prerift topography or localized structural offsets. The farthest sample inland, SA12-27, was collected from a basement clast within the Dwyka Group stratigraphic unit and is therefore constrained at the surface at approximately 300 Ma. The thermal history predicts consistent heating to temperatures of approximately 120°C at approximately 100 Ma, which would imply progressive burial until the Late Cretaceous. This burial event could reflect internal drainage of an eroding rift flank resulting in inland deposition. However, what the maximum post-Dwyka paleotemperature was for this sample and when that paleotemperature was attained is uncertain, and therefore, there is the possibility that burial was completed at almost any time between the stratigraphic age and approximately 100 Ma (Text S7).

The most significant period of denudation occurred during the Late Cretaceous (approximately 110–70 Ma) with a denudation thickness of approximately 2–4 km, and in some cases close to 5 km, being predicted across all three transects. This thickness of denudation is not seen uniformly across the transects, with some sample thermal histories observing no inflection in their cooling history in the Late Cretaceous but preserving the Early Cretaceous record of cooling. Although “Early Cretaceous” thermal histories do not record the onset of rapid Late Cretaceous cooling, these thermal history paths still imply that slow cooling, and denudation on the order of 1 km, continued throughout the Late Cretaceous across the entire margin. This pattern of denudation may have been driven by a combination of localized fault block uplift across major and minor faults combined with a regional uplift of the entire margin.

Denudation during the Cenozoic is predicted to be low in comparison to the Cretaceous, less than approximately 1 km in most samples over this time. Exceptions to this appear to be predominantly found far onto the plateau (see thermal histories for NQ Plateau and SA12-27), where denudation in the early Cenozoic exceeds 1–2 km from approximately 70 to 30 Ma. Over the last 30 Ma, denudation is predicted to be less than 0.5 km. Low amounts of Cenozoic denudation are supported by cosmogenic nuclide studies in southwestern Africa [Kounov *et al.*, 2007], Namibia [Cockburn *et al.*, 2000; van der Wateren and Dunai, 2001; Bierman and Caffee, 2001; Codilean *et al.*, 2008, 2014], and the Southern Cape [Decker *et al.*, 2011; Erlanger *et al.*, 2012; Scharf *et al.*, 2013; Bierman *et al.*, 2014; Kounov *et al.*, 2015], which all report a decrease in denudation rate by an order of magnitude during the Cenozoic relative to the Cretaceous.

## 6. Discussion

### 6.1. Sediment Accumulation in the Orange Basin

The catchment of the present-day Orange River covers an area of approximately  $1 \times 10^6 \text{ km}^2$  and transports material eroded from the continent to the offshore Orange Basin. It is suggested that since breakup, the main drainage outlet to the Orange Basin was located in a position similar to that of the present-day Orange River, Buffels River, or Olifants River [e.g., Partridge and Maud, 1987; Dollar, 1998; de Wit, 1999; de Wit *et al.*, 2000; Goudie, 2005; Stevenson and McMillan, 2004] (Figure 8). Therefore, most of the sediment derived from erosion of the southwestern continental margin and interior hinterland following breakup has been transported to the Orange Basin via the proto-Orange River and smaller rivers along the coast [e.g., Gilchrist *et al.*, 1994; Kooi and Beaumont, 1994; van der Beek *et al.*, 2002; de Wit *et al.*, 2000; Goudie, 2005]. Due to the long-term stability of the Orange River catchment, the record of sediment accumulation preserved in the Orange Basin provides independent constraints on the timing of onshore erosion [e.g., Rouby *et al.*, 2009; Guillocheau *et al.*, 2012].

Previous studies have provided detailed descriptions of the Orange Basin stratigraphy [Muntingh and Brown, 1993; Brown *et al.*, 1995; McMillan, 2003; Paton *et al.*, 2008; Kuhlmann *et al.*, 2010; Wildman *et al.*, 2015] and

**Figure 9.** Coast-perpendicular sections (see Figure 1) with predictions on magnitudes of denudation over time intervals since 150 Ma and sample/profile models used to derive these estimates. Data within 7.5 km on either side of the section trace were projected at 90° onto the line of section. Denudation estimates are made directly from thermal history models generated by inverting data from this study and from Wildman *et al.* [2015]. Denudation is estimated using an assumed geothermal gradient of 25°C/km. Samples comprising multisample inversions are as follows: Kamiesberg Upper: 8832-78, 8832-79, SA12-38, SA12-37, and SA12-36; Kamiesberg Lower: SA12-35 and SA12-33; NQ Plateau: 8832-75 and SA12-52; and NQ Coast: NQ12-15, NQ12-16, NQ12-17, and NQ12-18.



chronology of sediment accumulation over the last approximately 150 Myr [Rust and Summerfield, 1990; Rouby *et al.*, 2009; Guillocheau *et al.*, 2012]. Here we simply highlight the correlation between offshore accumulation in the Orange Basin as constrained primarily by the comprehensive investigation by Guillocheau *et al.* [2012] and the timing of denudation as inferred from our thermal history models. Two major peaks in accumulated sediment volume characterize the record of postrift sediment influx to the Orange Basin. The first peak records accumulated sediment volumes of approximately  $10 \times 10^{14} \text{ m}^3$  from 150 to 130 Ma (i.e., syn-rift) and the second peak, the maximum recorded sediment volume, of approximately  $11 \times 10^{14} \text{ m}^3$  is observed at approximately 80–70 Ma. In addition to a clear peak in accumulated volume being defined during the Campanian, there is a well-defined period of increasing sediment volume preceding this peak that begins at approximately 110–100 Ma. Another noticeable feature of the offshore sediment accumulation history is the minimal accumulation predicted throughout the Cenozoic ( $5 \times 10^{14} \text{ m}^3$ ).

We reiterate and lend further support to the conclusions drawn from our previous AFT study on the southern Atlantic margin [Wildman *et al.*, 2015] that denudation episodes inferred from the thermal histories derived from joint inversion of AFT and AHe data are consistent with the offshore accumulation history in the Orange Basin. Coherent features include an initial episode of denudation/sedimentation during the synrift (approximately 165–130 Ma) [Jackson *et al.*, 2000; Eagles, 2007; Heine *et al.*, 2013] period, an episode of postrift denudation at approximately 110–90 Ma, which coincides with increasing sediment volumes during the Middle to Late Cretaceous, and minimal denudation throughout the Cenozoic, which is reflected in low levels of accumulation from the end Cretaceous to the present day. The lag time between the onset of denudation in the mid-Cretaceous and the peak volume of sediment in the basin may be related to a disruption of internal drainage networks during the creation of fault-related relief, transient storage within the large proto-Orange catchment, or due to regional tilting of the African continent [e.g., Braun *et al.*, 2014].

## 6.2. Evidence for Postrift Faulting Along the Southwest African Margin

The structural evolution of the Namaqualand sector of the South Atlantic continental margin is complex and poorly understood [Andreoli *et al.*, 2009]. Deformation associated with major prerift tectonic events defined the preexisting structural grain in both Namaqualand and in the Cape Fold Belt. These ancient fractures likely provided sites of preexisting weakness in the lithosphere that controlled the style of fault propagation during rifting [e.g., Ziegler and Cloetingh, 2004; Autin *et al.*, 2013; Corti *et al.*, 2013; Will and Frimmel, 2013] and may have provided the location for postrift deformation during later tectonic events [e.g., Sykes, 1978; Daly *et al.*, 1989; Saintot *et al.*, 2011; Viola *et al.*, 2012].

By combining remote sensing techniques to identify major structural lineaments with a detailed field-based analysis of brittle fault structures, Viola *et al.* [2012] suggest that a record of postrift reactivation is preserved in the Namaqualand basement rocks. The earliest synrift or postrift paleostress tensor identified by Viola *et al.* [2012] is suggested to have been produced by subhorizontal extension orientated NE-SW, causing reactivation of older faults during the Early Cretaceous. This phase of extension is assigned to the initiation of rifting and opening of the Atlantic due to the coherence of the orientation of extension and the perpendicular orientation of major Early Cretaceous dyke swarms [Reid and Rex, 1994; Will and Frimmel, 2013].

Postrift paleotensors identified by Viola *et al.* [2012] are suggested to represent alternating episodes of regional extension and compression throughout the Middle to Late Cretaceous. However, the timing of these events is poorly constrained. Moreover, paleostress analysis in NW Namibia suggests that ENE-WSW and NE-SW extension prevailed during rifting and Late Cretaceous, respectively, and provides no clear evidence of compression [Salomon *et al.*, 2014, 2015]. In the Vaalputs region, inland of the Namaqualand Highlands, normal fault-slip structures extend into the silicified and kaolinitized weathering profiles of the Dasdap alluvial fan sediments [Brandt *et al.*, 2003, 2005] and into the volcanic breccias preserved at the Gamoep mellilite pipe (77–54 Ma) [Phillips *et al.*, 2000]. Despite the limited robust information on the timing of faulting from these studies, they provide important field evidence that postrift faulting has occurred. Thermochronology data reported here and in Kounov *et al.* [2009] suggest that this faulting may have begun during the mid-Cretaceous. The thermal history predictions made from the Kamiesberg profile (see section 4.3.3 above) suggest that differential denudation may have occurred across prominent NNW-SSE lineaments dissecting the profile, as a result of mid-Cretaceous fault movement.

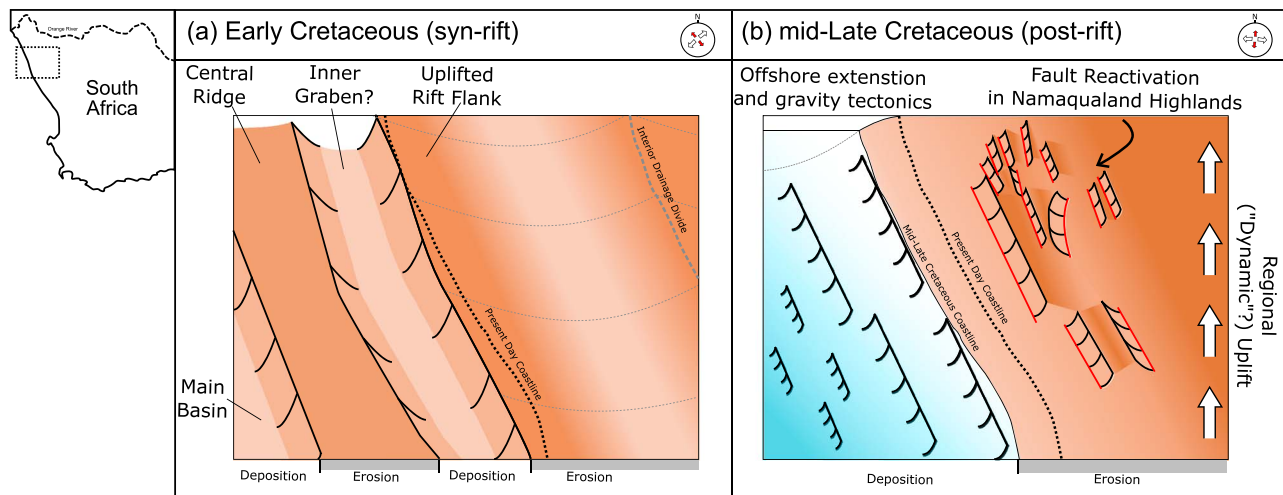


**Figure 10.** Cartoon representation of the post-Jurassic tectonic evolution of the southwest African continental margin. (a) Rifting during the Early Cretaceous creates deep fault-bounded grabens in the proximal part of the margin and a fault-bounded uplifted rift flank. Synrift erosion of uplifted fault blocks and elevated rift flanks occurs during extension due to the drop of regional base levels to the nascent Atlantic Ocean with deposition resulting in developing basins. The uplifted rift flank is eroded by escarpment downwearing most likely with an interior drainage divide causing denudation to extend far inland. (b) Prolonged extension across the South Atlantic and regional intraplate stresses are augmented with extensional stresses induced from vertical motions related to the loading and unloading of the margin and the possible presence of a buoyant mantle upwelling beneath the continental interior also causing regional uplift of South Africa. The preexisting structure and preferential orientation of these structures with the regional stress field at this time primes the faults for reactivation. Brittle tectonics may have extended into the offshore domain with gravitational slumping occurring farther oceanward due to a regional uplift of the continent. Paleostress tensors taken after Viola *et al.* [2012].

Within the offshore postrift sedimentary successions, gravitational tectonics is described involving extension-driven slumping in the proximal margin and toe thrusting in the outer shelf [Brown, 1995; Paton *et al.*, 2008; de Vera *et al.*, 2010; Hirsch *et al.*, 2010]. The major zone of extension and compression has a basal detachment in the marine shales of the Turonian-Cenomanian boundary [Muntingh and Brown, 1993; Séranne and Anka, 2005; de Vera *et al.*, 2010]. The development of growth strata and stratigraphic relationships led de Vera *et al.* [2010] to conclude that gravitational tectonics were periodically active in short-lived episodes. The regional mechanisms that trigger movement on these faults are still uncertain but have been related to the influx of high volumes of sediment to the basin [Jungslager, 1999; Paton *et al.*, 2007; Kuhlmann *et al.*, 2010], basin inversion and the development of enhanced structural relief, or margin uplift [Séranne and Anka, 2005; Paton *et al.*, 2008; de Vera *et al.*, 2010]. The timing of offshore gravitationally driven tectonic episodes (approximately 100–80 Ma) overlaps with the timing of major denudation of the continental margin inferred from low-temperature thermochronology. It is now possible to explicitly link this period of structurally controlled denudation onshore, involving the removal of several kilometers of material from the continental margin and interior to the onset of offshore slumping. Viola *et al.* [2005] have documented younger neotectonic inversion structures in the Orange Basin that are linked to the onshore structural network in southern Namibia and Namaqualand. In the southern offshore basins, detailed seismic reflection has provided additional evidence of discrete episodes of basin inversion and/or reactivation [Bate and Malan, 1992; Boyd *et al.*, 2011; Hartwig *et al.*, 2012; Paton *et al.*, 2008; Tinker *et al.*, 2008b; van der Merwe and Fouche, 1992].

### 6.3. Drivers of Postrift Tectonic Activity: Regional and Local Mechanisms

Apatite fission track and AHe data from continental margins have commonly been interpreted in terms of simple conceptual models of escarpment evolution following breakup [e.g., Ollier and Pain, 1997; Gallagher and Brown, 1999; Gunnell *et al.*, 2003; Campanile *et al.*, 2008; Persano *et al.*, 2002, 2005; Braun and van der Beek, 2004]. However, the temporal and spatial pattern of the data presented here is incompatible with that predicted by any of these conceptual models [Gallagher and Brown, 1999]. The discrepancy primarily lies in the common occurrence of young postrift AFT and AHe ages far inland of the escarpment. Abrupt age variations across basement structures also suggest a more complex evolution of the margin. We advocate that while a phase of synrift erosion of elevated rift flanks occurred (Figure 10a), an episode of postrift denudation during the Middle to Late Cretaceous is more significant in terms of the geomorphic evolution of the margin

(Figure 10b). Based on our study, we suggest that postrift denudation is triggered by deformation of the upper crust driven by a combination of regional horizontal and vertical stresses that are focused by local thermal and mechanical properties of the crust.

The present-day stress field across the southwestern African continental margin is characterized by a NW-SE/NNW-SSE orientation of horizontal principal compressive stress, which has been attributed to lithospheric resistance to plate and microplate movements [Bird *et al.*, 2006]. The stress field is proposed to be induced by overall net NE-SW extension and has been linked to neotectonics and present-day seismic activity in the area [Andreoli *et al.*, 1996; Ben-Avraham *et al.*, 2002; Brandt *et al.*, 2005; Viola *et al.*, 2005; White *et al.*, 2009; de Beer, 2012]. This stress field will have evolved over time with changes in plate direction and spreading velocity and, as is the case today, would have promoted faulting across the margin. Loading of the offshore Orange Basin during the synrift and postrift phases, causing flexure of the lithosphere, would have enhanced coast-perpendicular extensional stresses at this time [Kusznir *et al.*, 1991; Wernicke and Axen, 1988; Redfield *et al.*, 2005; Salomon *et al.*, 2014; Redfield and Osmundsen, 2013]. However, the style and location of fault reactivation will be dependent on the orientation of faults to the regional stress field and may have involved local compression within an overall extension regime [e.g., Holford *et al.*, 2014].

The timing of postrift denudation proposed here is coeval with a maximum Atlantic seafloor spreading rate (Figure 11) of 7–8 cm/yr during the Middle Cretaceous (approximately 120–80 Ma) [Coffin *et al.*, 1998; Müller *et al.*, 2008; Labails *et al.*, 2009; Torsvik *et al.*, 2009; Moulin *et al.*, 2010]. The start of this maximum spreading rate coincides with the onset of seafloor spreading in the southern Atlantic at approximately 120 Ma (chron-CM0). At approximately 100 Ma, a change in plate motion linked to the final breakup of South America and Africa after seafloor spreading propagated northward to the equatorial Atlantic [Eagles, 2007; Heine *et al.*, 2013; Jones *et al.*, 1995; Moulin *et al.*, 2010; Nürnberg and Müller, 1991; Torsvik *et al.*, 2009; Granot and Dymant, 2015], although a change in spreading rate velocity is only recorded in one model (Africa-NGU) [Colli *et al.*, 2014] of Atlantic spreading rates (Figure 11). A sharp decrease in plate velocity occurs from 80 to 70 Ma, dropping to rates of approximately 3–4 cm/yr [Cande *et al.*, 1988; Müller *et al.*, 2008; Torsvik *et al.*, 2009; Moulin *et al.*, 2010], which is coincident with another shift in plate spreading direction (C31; Figure 11) and the cessation of major denudation predicted by our thermal history models.

Changes to the orientation of plate movement can be observed in the geometry of Late Cretaceous to early Cenozoic magnetic anomalies in the Mid-Atlantic and SW Indian Ocean (Figure 11). The slowdown in plate velocity at this time has been linked to the development of new transform faults along the ridge crest and the arrival of the Reunion Plume beneath the India-African plate boundary [Cande and Stegman, 2011; Pérez-Díaz and Eagles, 2014]. The magnitude of stress required to reactivate faults is dependent on fault geometry, fault orientation relative to the regional stress field, and the frictional resistance along the fault plane [Sibson, 1985; Turner and Williams, 2004]. However, it is possible that even relatively small in-plane stresses may promote deformation [Cloetingh and Burov, 2011]. Recent plate reconstruction models have predicted deformation along intracontinental rift systems in South America, West Africa, and central Africa during the Cretaceous normal polarity superchron (chron CM0-C34) [Torsvik *et al.*, 2009; Heine *et al.*, 2013; Pérez-Díaz and Eagles, 2014], which was largely completed by approximately 90 Ma [Granot and Dymant, 2015]. However, kinematic modeling has predicted that between 33 and 58% of intracontinental deformation is accommodated away from major intracontinental rift basins [e.g., Guiraud and Maurin, 1992; Loule and Pospisil, 2013; Pérez-Díaz and Eagles, 2014]. It is suggested in our study that Middle to Late Cretaceous postrift fault reactivation at the southwest African continental margin contributes to this additional deformation.

Regional vertical movements of the African Plate are driven by isostatic adjustments to unloading and loading of the crust [Gilchrist and Summerfield, 1990; Hartley *et al.*, 1996; Molnar *et al.*, 2015] and the presence of vertical stresses at the base of the lithosphere exerted by a buoyant mantle anomaly beneath the continent [Lithgow-Bertelloni and Silver, 1998; Gurnis *et al.*, 2000; Nyblade and Sleep, 2003; Braun *et al.*, 2014]. The latter of these has received particular attention in an attempt to constrain the spatial extent and magnitude of dynamic uplift and the creation of dynamic topography over time [Forte *et al.*, 2010; Moucha and Forte, 2011; Braun, 2010; Flament *et al.*, 2014]. Recent numerical surface process modeling has shown that modest amounts of dynamic uplift can trigger kilometers of erosion [Braun *et al.*, 2013]. The relative contribution of truly dynamic topography (i.e., topography supported only by active flow within the mantle) in creating Southern Africa's high elevation is arguably small, while the isostatic compensation of the South African crust

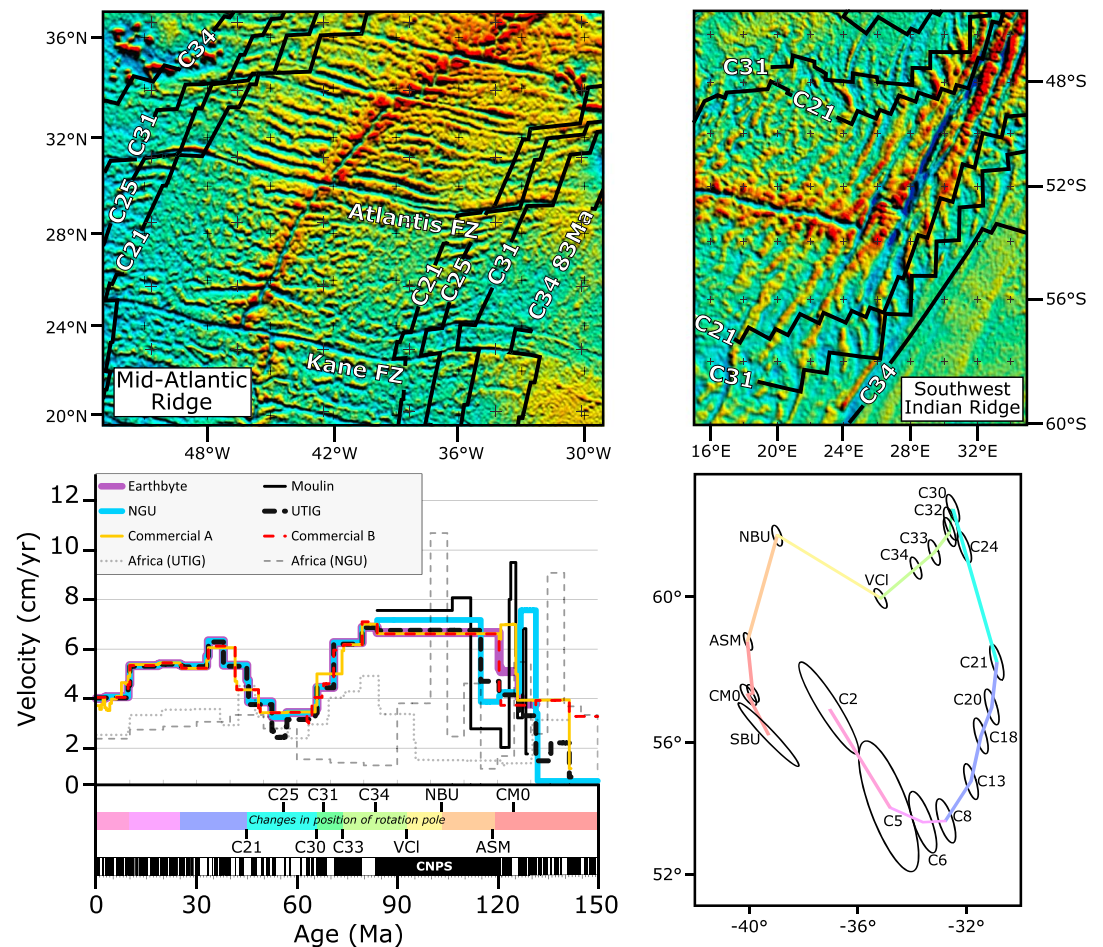


**Figure 11.** (top row) Key Late Cretaceous to early Cenozoic magnetic anomalies on WGM2012 global model gravity maps of ocean flow lines for the Mid-Atlantic Ridge and Southwest Indian Ridge. (bottom left) Spreading rates of South Atlantic opening for different plate reconstruction models from 150 Myr to the present for a point currently located at 57.2°W, 36°S in a reference frame that keeps Africa fixed [after Colli *et al.*, 2014]. Africa (NGU) and Africa (UTIG) show the absolute velocities of Africa in a mantle reference frame for an approximately conjugate point in the Orange Basin, at 15°E, 27.5°S. See Colli *et al.* [2014, and references therein] for a full discussion of each individual plate reconstruction model. (bottom right) Location of the African Plate finite rotation pole over time [after Pérez-Díaz and Eagles, 2014]. Ellipses indicate 95% confidence intervals on location. Colored lines correspond to time intervals beneath histogram of spreading rate velocity.

and mantle lithosphere arising from the relative buoyancy of material comprising the flow plays a far more important role [Molnar *et al.*, 2015]. Changes in the thermal structure and chemical and mineralogical composition of the lithosphere during the Middle Cretaceous (approximately 100–90 Ma) have been documented [Bell *et al.*, 2003; Griffin *et al.*, 2003; Janney *et al.*, 2010; Stanley *et al.*, 2013, 2015] and could have triggered isostatically driven uplift of the South African landscape at this time [Molnar *et al.*, 2015].

The coupled dynamics of horizontal and vertical motions has been explored by mantle flow modeling by Colli *et al.* [2014]. The intrinsic linkage between horizontal and vertical motions illustrated by these models suggests that the coeval changes at approximately 90 Ma and 30 Ma in the South Atlantic spreading rates (Figure 11) and uplift of the southwest African continental margin are geodynamically linked to one another. The interaction between in-plane stresses in the lithosphere and thermal convection in the mantle has been investigated by recent three-dimensional thermomechanical models using realistic lithospheric rheologies and predict complex patterns of short-wavelength deformation of a brittle crust overlying a ductile mantle lithosphere [Burov, 2011; Guillou-Frotier *et al.*, 2012; Burov and Gerya, 2014; Koptev *et al.*, 2015]. This work offers the interesting possibility of a regional, long-wavelength mechanism of uplift, like mantle flow, causing quite local deformation at the surface, and would explain why we observe both regional and local signals of



tectonic activity within Southern Africa during the mid-Cretaceous. The emplacement of mid-Cretaceous alkaline intrusions along major tectonic boundaries may also indicate a link between mantle convection and tectonic readjustments [Jelsma *et al.*, 2009].

Regional denudation during the Middle to Late Cretaceous, predicted by thermochrometry data [Brown *et al.*, 2002, 2014; Tinker *et al.*, 2008a; Kounov *et al.*, 2009, 2013; Flowers and Schoene, 2010; Stanley *et al.*, 2013, 2015; Wildman *et al.*, 2015], has underpinned the timing of uplift events proposed by numerical models [e.g., van der Beek *et al.*, 2002; Braun *et al.*, 2014; Molnar *et al.*, 2015]. By jointly inverting AFT and AHe data, our modeling results limit the thickness of overburden removed during the Cenozoic to less than 1 km or, in rare cases, less than 1.5 km. This observation is therefore consistent with models invoking a Cretaceous age for the present-day landscape and is difficult to reconcile with models that predict the development of the present-day topography from an initially flat surface over the last 30 Myr [e.g., Partridge and Maud, 1987; Burke, 1996; Burke and Gunnell, 2008; Roberts and White, 2010; Paul *et al.*, 2014; Rudge *et al.*, 2015]. Our interpretation does not preclude modest amounts of surface uplift and channel incision occurring during the Cenozoic but requires that subsequent erosion was minimal, likely due to the prevailing arid to semiarid climate at the time [de Wit, 1999; Pickford and Senut, 1999; Bamford, 2000; Gutzmer and Beukes, 2000]. In addition to limiting the contribution of Cenozoic erosion, our new data reveal short-wavelength variations in the spatial pattern of mid-Cretaceous denudation, which are attributed to postrift brittle deformation of the margin and continental interior. Our data are incapable of resolving the specific kinematics of postrift deformation that is caused by a complex interaction of horizontal and vertical induced stresses and crustal heterogeneity. However, these data provide important new quantitative constraints that can help to constrain future numerical models that link surface process, mantle geodynamics, and global plate tectonics.

## 7. Conclusion

This study provides the first suite of joint AFT and AHe data across the Namaqualand sector of the southwest African continental margin. The data provide evidence for major crustal cooling of the margin during the Cretaceous with only minor cooling (less than 30–40°C) occurring through the Cenozoic. Joint thermal history inversion of the data provides evidence for two distinct major cooling episodes, which caused kilometer-scale denudation (approximately 2–5 km). The early denudation event is associated with synrift erosion of preexisting topography, possibly augmented by tectonic uplift during rifting, while the later episode was triggered by postrift tectonic reactivation of the margin and regional uplift of the continent in the middle-Late Cretaceous. Any contribution of Cenozoic tectonic or surface processes did not cause enough erosion to be reflected in the thermochronology data, and the total Cenozoic erosion is restricted to less than approximately 1–1.5 km.

The overall spatial and temporal pattern of erosion as documented here requires an explanation that can accommodate both a regional, long-wavelength geomorphic response extending well inland of the major escarpment zone and more localized, short-wavelength fault-related erosion. We believe that the observed pattern of topographic evolution, as inferred through the erosional response documented here, implies that several mechanisms operating at or certainly dominating over different wavelengths are involved.

In addition to erosion of the regional, long-wavelength topography linked to chemical and thermal mantle lithosphere changes, we propose that intracontinental deformation and related relief was an important feature of the postrift development of the margin. The transfer of plate boundary stresses arising from significant changes in the plate kinematics within the South Atlantic and West Indian Oceans, combined with an enhanced tensional stress field across the margin induced by flexure of the lithosphere, triggered fault reactivation and led to localized erosion patterns during the Middle to Late Cretaceous. It is possible that some of the short-wavelength deformation is itself linked to the deeper mantle mechanism through a more complex response of the lithosphere to vertical stresses, although this possibility remains speculative at this stage.

While the exact geometry of structures and the precise location of faults that accommodated major offsets are still unknown, the data presented here indicate a major surface response to significant middle-Late Cretaceous tectonic activity, which occurred along the so-called passive continental margin of the southwest Africa.



## Acknowledgments

Full analytical details, data tables, QTQt models, and QTQt data files can be accessed through the supporting information. We thank Marco Andreoli, Olivier Datueil, Francois Guillocheau, Tim Redfield, Delphine Rouby, and Giulio Viola for their insightful discussions at various stages of the project. Marco Andreoli and staff at NECSA are thanked for their logistic support during fieldwork in Namaqualand. Rebecca Flowers, Taylor Schildgen, and Peter van der Beek are thanked for their constructive comments on this work. This work was funded by the Natural Environment Research Council, UK, grants NE/H008276/1; NE/H008454/1; and NE/JE500252/1.

## References

- Adamson, R. S. (1931), Note on some petrified wood from Banke, Namaqualand, *Trans. R. Soc. S. Afr.*, 19(3), 255–258, doi:10.1080/00359193109518838.
- Andreoli, M. A. G., M. Doucouré, J. Van Bever Donker, D. Brandt, and N. J. B. Andersen (1996), Neotectonics of southern Africa, *Afr. Geosci. Rev.*, 3, 1–16.
- Andreoli, M. A. G., R. J. Hart, L. D. Ashwal, and H. Coetzee (2006), Correlations between U, Th content and metamorphic grade in the western Namaqualand Belt, South Africa, with implications for radioactive heating of the crust, *J. Petrol.*, 47(6), 1095–1118, doi:10.1093/petrology/egl004.
- Andreoli, M. A. G., G. Viola, A. Kounov, J. Scheepers, O. Heidbach, and I. Stengel (2009), History of stress at Vaalputs, Namaqualand, South Africa: Evidence for a Mid-Cretaceous “Wegener-type Orogeny” in western southern Africa, in *11th SAGA Biennial Technical Meeting and Exhibition*, pp. 515–520, South African Geophysical Association Conference, Swaziland, 16–18 Sept.
- Aslanian, D. and M. Moulin (2013), Palaeogeographic consequences of conservative models in the South Atlantic Ocean, *Geol. Soc. London, Spec. Publ.*, 369(1), 75–90, doi:10.1144/SP369.5.
- Aslanian, D. et al. (2009), Brazilian and African passive margins of the Central Segment of the South Atlantic Ocean: Kinematic constraints, *Tectonophysics*, 468(1), 98–112, doi:10.1016/j.tecto.2008.12.016.
- Ault, A. K., and R. M. Flowers (2012), Is apatite U–Th zonation information necessary for accurate interpretation of apatite (U–Th)/He thermochronometry data?, *Geochim. Cosmochim. Acta*, 79, 60–78, doi:10.1016/j.gca.2011.11.037.
- Autin, J. N., Bellahsen, S., Leroy, L., Hussen, M. O., Beslier, and E. d’Acremont (2013), The role of structural inheritance in oblique rifting: Insights from analogue models and application to the Gulf of Aden, *Tectonophysics*, 607, 51–64, doi:10.1016/j.tecto.2013.05.041.
- Ballard, S. and H. N. Pollack (1987), Diversion of heat by Archean cratons: A model for southern Africa, *Earth Planet. Sci. Lett.*, 85(1), 253–264, doi:10.1016/0012-821X(87)90036-7.
- Bamford, M. K. (2000), Fossil woods of Karoo age deposits in South Africa and Namibia as an aid to biostratigraphical correlation, *J. Afr. Earth Sci.*, 31(1), 119–132, doi:10.1016/S0899-5362(00)00077-4.
- Bate, K. J. and J. A. Malan (1992), Tectonostratigraphic evolution of the Algoa, Gamtoos and Pletmos basins, offshore South Africa, in *Inversion Tectonics of the Cape Fold Belt, Karoo and Cretaceous Basins of Southern Africa*, pp. 61–73, Balkema, Rotterdam, Netherlands.
- Bell, D. R. M., D. Schmitz, and P. E. Janney (2003), Mesozoic thermal evolution of the southern African mantle lithosphere, *Lithos*, 71(2), 273–287.
- Ben-Avraham, Z., G. Smith, M. Reshef, and E. Jungslager (2002), Gas hydrate and mud volcanoes on the southwest African continental margin off South Africa, *Geology*, 30(10), 927–930, doi:10.1130/0091-7613(2002)030<0927:GHAMVO>2.0.CO;2.
- Beucher, R. R. W., Brown, S., Roper, F., Stuart, and C. Persano (2013), Natural age dispersion arising from the analysis of broken crystals: Part II. Practical application to apatite (U–Th)/He thermochronometry, *Geochim. Cosmochim. Acta*, 120, 395–416, doi:10.1016/j.gca.2013.05.042.
- Bierman, P. R. and M. Caffee (2001), Slow rates of rock surface erosion and sediment production across the Namib Desert and escarpment, southern Africa, *Am. J. Sci.*, 301(4–5), 326–358, doi:10.2475/ajsc.301.4-5.326.
- Bierman, P. R., R. Coppersmith, K. Hanson, J. Neveling, E. W. Portenga, and D. H. Rood (2014), A cosmogenic view of erosion, relief generation, and the age of faulting in southern Africa, *GSA Today*, 24(9), 4–11, doi:10.1130/GSATG206A.1.
- Bird, P., Z. Ben-Avraham, G. Schubert, M. Andreoli, and G. Viola (2006), Patterns of stress and strain rate in southern Africa, *J. Geophys. Res.*, 111, B08402, doi:10.1029/2005JB003882.
- Blaich, O. A. J. I., Faleide, and F. Tsikalas (2011), Crustal breakup and continent-ocean transition at South Atlantic conjugate margins, *J. Geophys. Res.*, 116, B01402, doi:10.1029/2010JB007686.
- Boyd, D., Z. Anka, R. Di Primio, G. Kuhlmann, and M. J. De Wit (2011), Passive margin evolution and controls on natural gas leakage in the Orange Basin, South Africa, *S. Afr. J. Geol.*, 114(3–4), 415–432.
- Brandt, D. M. A. G., Andreoli, and T. S. McCarthy (2003), Mesozoic fluvial deposits on a rifted continental margin near Vaalputs, Namaqualand, South Africa, *S. Afr. J. Geol.*, 106(1), 11–16, doi:10.2113/1060011.
- Brandt, D. M. A. G., Andreoli, and T. S. McCarthy (2005), The late Mesozoic palaeosols and Cenozoic fluvial deposits at Vaalputs, Namaqualand, South Africa: Possible depositional mechanisms and their bearing on the evolution of the continental margin, *S. Afr. J. Geol.*, 108(2), 271–284, doi:10.2113/108.2.271.
- Braun, J. (2010), The many surface expressions of mantle dynamics, *Nat. Geosci.*, 3(12), 825–833, doi:10.1038/ngeo1020.
- Braun, J. and C. Beaumont (1989), A physical explanation of the relation between flank uplifts and the breakup unconformity at rifted continental margins, *Geology*, 17(8), 760–764, doi:10.1130/0091-7613(1989)017<0760:APEOTR>2.3.CO;2.
- Braun, J. and P. Van Der Beek (2004), Evolution of passive margin escarpments: What can we learn from low-temperature thermochronology?, *J. Geophys. Res.*, 109, F04009, doi:10.1029/2004JF000147.
- Braun, J., X. Robert, and T. Simon-Labrie (2013), Eroding dynamic topography, *Geophys. Res. Lett.*, 40, 1494–1499, doi:10.1002/grl.50310.
- Braun, J., F. Guillocheau, C. Robin, G. Baby, and H. Jelsma (2014), Rapid erosion of the Southern African Plateau as it climbs over a mantle superswell, *J. Geophys. Res. Solid Earth*, 119, 6093–6112, doi:10.1002/2014JB010998.
- Bronner, A. D., Sauter, G., Manatschal, G., Péron-Pinvidic, and M. Munschy (2011), Magmatic breakup as an explanation for magnetic anomalies at magma-poor rifted margins, *Nat. Geosci.*, 4(8), 549–553, doi:10.1038/ngeo1201.
- Brown, L. F., J. M. Benson, G. J. Brink, S. Doherty, A. Jollands, E. H. A. Jungslager, J. H. G. Keenan, A. Muntingh, and N. J. S. van Wyk (1995), *Sequence Stratigraphy in Offshore South African Divergent Basins: An Atlas on Exploration for Cretaceous Lowstand Traps by Soekor (Pty) Ltd*, AAPG Stud. in Geol. 41, AAPG, doi:10.1306/St41600.
- Brown, R. M., Summerfield, A., Gleadow, K., Gallagher, A., Carter, R., Beucher, and M. Wildman (2014), Intracontinental deformation in southern Africa during the Late Cretaceous, *J. Afr. Earth Sci.*, 100, 20–41, doi:10.1016/j.jafrearsci.2014.05.014.
- Brown, R. W. D., J. Rust, M. A. Summerfield, A. J. Gleadow, and M. C. De Wit (1990), An Early Cretaceous phase of accelerated erosion on the south-western margin of Africa: Evidence from apatite fission track analysis and the offshore sedimentary record, *Int. J. Radiat. Appl. Instrum., Part D*, 17(3), 339–350, doi:10.1016/1359-0189(90)90056-4.
- Brown, R. W., M. A. Summerfield, and A. J. Gleadow (2002), Denudational history along a transect across the Drakensberg Escarpment of southern Africa derived from apatite fission track thermochronology, *J. Geophys. Res.*, 107(B12), 2350, doi:10.1029/2001JB000745.
- Brown, R. W., R. Beucher, S. Roper, C. Persano, F. Stuart, and P. Fitzgerald (2013), Natural age dispersion arising from the analysis of broken crystals. Part I: Theoretical basis and implications for the apatite (U–Th)/He thermochronometer, *Geochim. Cosmochim. Acta*, 122, 478–497, doi:10.1016/j.gca.2013.05.041.
- Brune, S. C., Heine, M., Pérez-Gussinyé, and S. V. Sobolev (2014), Rift migration explains continental margin asymmetry and crustal hyper-extension, *Nat. Commun.*, 5, 4014.
- Buiter, S. J. and T. H. Torsvik (2014), A review of Wilson Cycle plate margins: A role for mantle plumes in continental break-up along sutures? *Gondwana Res.*, 26(2), 627–653, doi:10.1038/ncomms5014.

- Burbank, D. W., and R. S. Anderson (2012), *Tectonic Geomorphology*, 2nd ed., 454 pp., Wiley, West Sussex, U. K.
- Burke, K. (1996), The African Plate, *S. Afr. J. Geol.*, 99(4), 341–409.
- Burke, K. and Y. Gunnell (2008), The African erosion surface: A continental-scale synthesis of geomorphology, tectonics, and environmental change over the past 180 million years, *Geol. Soc. Am. Mem.*, 201, 1–66, doi:10.1130/2008.1201.
- Burov, E. B. (2011), Rheology and strength of the lithosphere, *Mar. Pet. Geol.*, 28(8), 1402–1443, doi:10.1016/j.marpetgeo.2011.05.008.
- Burov, E. B. and T. Gerya (2014), Asymmetric three-dimensional topography over mantle plumes, *Nature*, 513(7516), 85–89, doi:10.1038/nature13703.
- Calignano, E. D. Sokoutis, E. Willingshofer, F. Gueydan, and S. Cloetingh (2015), Strain localization at the margins of strong lithospheric domains: Insights from analog models, *Tectonics*, 34, 396–412, doi:10.1002/2014TC003756.
- Campanile, D. C. G. Nambiar, P. Bishop, M. Widdowson, and R. Brown (2008), Sedimentation record in the Konkan–Kerala Basin: Implications for the evolution of the Western Ghats and the Western Indian passive margin, *Basin Res.*, 20(1), 3–22, doi:10.1111/j.1365-2117.2007.00341.x.
- Cande, S. C. and D. R. Stegman (2011), Indian and African plate motions driven by the push force of the Reunion plume head, *Nature*, 475(7354), 47–52, doi:10.1038/nature10174.
- Cande, S. C. J. L. LaBrecque, and W. F. Haxby (1988), Plate kinematics of the South Atlantic: Chron C34 to present, *J. Geophys. Res.*, 93, 12,479–13,492, doi:10.1029/JB093ib11p13479.
- Clemson, J. J. Cartwright, and J. Booth (1997), Structural segmentation and the influence of basement structure on the Namibian passive margin, *J. Geol. Soc.*, 154(3), 477–482, doi:10.1144/gsjgs.154.3.0477.
- Clifford, T. N. E. S. Barton, R. A. Stern, and J. C. Duchesne (2004), U–Pb zircon calendar for Namaquan (Grenville) crustal events in the granulite-facies terrane of the O’okiep copper district of South Africa, *J. Petrol.*, 45(4), 669–691, doi:10.1093/petrology/egg097.
- Cloetingh, S. and E. Burov (2011), Lithospheric folding and sedimentary basin evolution: A review and analysis of formation mechanisms, *Basin Res.*, 23(3), 257–290.
- Cloetingh, S. E. Burov, and T. Francois (2013), Thermo-mechanical controls on intra-plate deformation and the role of plume-folding interactions in continental topography, *Gondwana Res.*, 24(3), 815–837, doi:10.1016/j.gr.2012.11.012.
- Cockburn, H. A. P. R. W. Brown, M. A. Summerfield, and M. A. Seidl (2000), Quantifying passive margin denudation and landscape development using a combined fission-track thermochronology and cosmogenic isotope analysis approach, *Earth Planet. Sci. Lett.*, 179(3), 429–435, doi:10.1016/S0012-821X(00)00144-8.
- Codilean, A. T. P. Bishop, F. M. Stuart, T. B. Hoey, D. Fabel, and S. P. Freeman (2008), Single-grain cosmogenic <sup>21</sup>Ne concentrations in fluvial sediments reveal spatially variable erosion rates, *Geology*, 36(2), 159–162, doi:10.1130/G24360a.1.
- Codilean, A. T. C. R. Fenton, D. Fabel, P. Bishop, and S. Xu (2014), Discordance between cosmogenic nuclide concentrations in amalgamated sands and individual fluvial pebbles in an arid zone catchment, *Quat. Geochronology*, 19, 173–180, doi:10.1016/j.quageo.2012.04.007.
- Coffin, M. F. L. M. Gahagan, and L. A. Lawver (1998), Present-day plate boundary digital data compilation, Univ. of Tex. Inst. for Geophys. Tech. Rep. 174, 5 pp.
- Cogné, N. K. Gallagher, and P. R. Cobbold (2011), Post-rift reactivation of the onshore margin of southeast Brazil: Evidence from apatite (U–Th)/He and fission-track data, *Earth Planet. Sci. Lett.*, 309(1), 118–130, doi:10.1016/j.epsl.2011.06.025.
- Colli, L. I. Stotz, H. P. Bunge, M. Smethurst, S. Clark, G. Iaffaldano, A. Tassara, F. Guillocheau, and M. C. Bianchi (2014), Rapid South Atlantic spreading changes and coeval vertical motion in surrounding continents: Evidence for temporal changes of pressure-driven upper mantle flow, *Tectonics*, 32, 1304–1321, doi:10.1002/2014TC003612.
- Colliston, W. P. A. E. Schoch, and J. Cole (2014), The Grenvillian Namaqua–Natal fold belt adjacent to the Kaapvaal Craton: 1. Distribution of Mesoproterozoic collisional terranes deduced from results of regional surveys and selected profiles in the western and southern parts of the fold belt, *J. Afr. Earth Sci.*, 100, 7–19, doi:10.1016/j.jafrearsci.2014.05.017.
- Cornelissen, A. K. and W. J. Verwoerd (1975), The Bushmanland kimberlites and related rocks, *Phys. Chem. Earth*, 9, 71–80, doi:10.1016/B978-0-08-018017-5.50011-0.
- Cornell, D. H. R. J. Thomas, R. Gibson, H. F. G. Moen, D. L. Reid, J. M. Moore, and R. L. Gibson (2006), The Namaqua–Natal Province, in *Geological Society of South Africa*, pp. 325–379, Pretoria, South Africa.
- Corti, G. J. van Wijk, S. Cloetingh, and C. K. Morley (2007), Tectonic inheritance and continental rift architecture: Numerical and analogue models of the East African Rift system, *Tectonics*, 26, TC6006, doi:10.1029/2006TC002086.
- Corti, G. G. Ranalli, A. Agostini, and D. Sokoutis (2013), Inward migration of faulting during continental rifting: Effects of pre-existing lithospheric structure and extension rate, *Tectonophysics*, 594, 137–148, doi:10.1016/j.tecto.2013.03.028.
- Curtis, C. G. R. B. Trumbull, C. H. de Beer, C. Harris, D. L. Reid, and R. L. Romer (2011), Geochemistry of the early Cretaceous Koegel Fontein anorogenic igneous complex, South Africa, *S. Afr. J. Geol.*, 114(3–4), 353–378, doi:10.2113/gssajg.114.3-4.353.
- Curtis, C. G. C. Harris, R. B. Trumbull, C. de Beer, and L. Mudzanani (2013), Oxygen isotope diversity in the anorogenic Koegel Fontein complex of South Africa: A case for basement control and selective melting for the production of low- $\delta^{18}\text{O}$  magmas, *J. Petrol.*, 54(7), 1259–1283, doi:10.1093/petrology/egt011.
- Daly, M. C. J. Chorowicz, and J. D. Fairhead (1989), Rift basin evolution in Africa: The influence of reactivated steep basement shear zones, *Geol. Soc. London Spec. Publ.*, 44(1), 309–334, doi:10.1144/gsl.sp.1989.044.01.17.
- Danišik, M. P. Štěpánčíková, and N. J. Evans (2012), Constraining long-term denudation and faulting history in intraplate regions by multisystem thermochronology: An example of the Sudetic Marginal Fault (Bohemian Massif, central Europe), *Tectonics*, 31, TC2003, doi:10.1029/2011TC003012.
- Dauteuil, O. F. Deschamps, O. Bourgeois, A. Mocquet, and F. Guillocheau (2013), Post-breakup evolution and palaeotopography of the North Namibian Margin during the Meso-Cenozoic, *Tectonophysics*, 589, 103–115, doi:10.1016/j.tecto.2012.12.022.
- Day, R. W. (1987), False Bay dolerites, *Ann. Geol. Surv. S. Afr.*, 21, 1–7.
- de Beer, C. H. (2002), *The Geology of the Calvinia Area: Explanation of 1:250 000-Scale Sheet 3118 Calvinia*, Council for Geosci., South Africa.
- de Beer, C. H. (2010), *The Geology of the Garies Area: Explanation of 1:250 000-Scale Sheet 3017 Garies*, Council for Geosci., South Africa.
- de Beer, C. H. (2012), Evidence of Neogene to Quaternary faulting and seismogenic deformation along the Namaqualand coast, South Africa, *S. Afr. J. Geol.*, 115(2), 117–136, doi:10.2113/gssajg.115.2.117.
- de Vera, J. P. Granado, and K. McClay (2010), Structural evolution of the Orange Basin gravity-driven system, offshore Namibia, *Mar. Pet. Geol.*, 27(1), 223–237, doi:10.1016/j.marpetgeo.2009.02.003.
- de Wit, M. C. J. (1988), Aspects of the geomorphology of the north-western Cape, South Africa, in *Geomorphological Studies in Southern Africa*, edited by G. F. Dardis and B. P. Moon, pp. 57–69, CRC Press, Rotterdam, Netherlands.
- de Wit, M. C. J. (1999), Post-Gondwana drainage and the development of diamond placers in western South Africa, *Econ. Geol.*, 94(5), 721–740, doi:10.2113/gsecongeo.94.5.721.
- de Wit, M. C. J. J. D. Ward, and R. Spaggiari (1992), A reappraisal of the Kangnas dinosaur site, Bushmanland, South Africa, *S. Afr. J. Sci.*, 88(9–10), 504–507.

- de Wit, M. C. J. T. R. Marshall, and T. C. Partridge (2000), Fluvial deposits and drainage evolution, in *The Cenozoic of Southern Africa*, edited by T. C. Partridge and R. R. Maud, pp. 55–72, Oxford Univ. Press, Oxford, U. K.
- Decker, J. E. S. Niedermann, and M. J. de Wit (2011), Soil erosion rates in South Africa compared with cosmogenic  $^3\text{He}$ -based rates of soil production, *S. Afr. J. Geol.*, *114*(3–4), 475–488, doi:10.2113/gssajg.114.3-4.475.
- Decker, J. E. S. Niedermann, and M. J. De Wit (2013), Climatically influenced denudation rates of the southern African plateau: Clues to solving a geomorphic paradox, *Geomorphology*, *190*, 48–60, doi:10.1016/j.geomorph.2013.02.007.
- Dewey, J. F. L. Robb, and L. Van Schalkwyk (2006), Did Bushmanland extensionally unroof Namaqualand? *Precambrian Res.*, *150*(3), 173–182, doi:10.1016/j.precamres.2006.07.007.
- Dollar, E. S. (1998), Palaeofluvial geomorphology in southern Africa: A review, *Prog. Phys. Geogr.*, *22*(3), 325–349, doi:10.1177/030913339802200302.
- Donelick, R. A. P. B. O'Sullivan, and R. A. Ketcham (2005), Apatite fission-track analysis, *Rev. Mineral. Geochem.*, *58*(1), 49–94, doi:10.2138/rmg.2005.58.3.
- Duncan, R. A. P. R. Hooper, J. Rehacek, J. S. Marsh, and A. R. Duncan (1997), The timing and duration of the Karoo igneous event, southern Gondwana, *J. Geophys. Res.*, *102*, 18,127–18,138, doi:10.1029/97JB00972.
- Dunkl, I. (2002), TRACKKEY: A Windows program for calculation and graphical presentation of fission track data, *Comput. Geosci.*, *28*(1), 3–12, doi:10.1016/S0098-3004(01)00024-3.
- Eagles, G. (2007), New angles on South Atlantic opening, *Geophys. J. Int.*, *168*(1), 353–361, doi:10.1111/j.1365-246x.2006.03206.x.
- Eagles, G. and M. König (2008), A model of plate kinematics in Gondwana breakup, *Geophys. J. Int.*, *173*(2), 703–717, doi:10.1111/j.1365-246x.2008.03753.x.
- Eglinton, B. M. (2006), Evolution of the Namaqua-Natal Belt, southern Africa—A geochronological and isotope geochemical review, *J. Afr. Earth Sci.*, *46*(1), 93–111, doi:10.1016/j.jafrearsci.2006.01.014.
- Erlanger, E. D. E. Granger, and R. J. Gibbon (2012), Rock uplift rates in South Africa from isochron burial dating of fluvial and marine terraces, *Geology*, *40*(11), 1019–1022, doi:10.1130/g33172.1.
- Estes, R. (1977), Relationships of the South African fossil frog *Eoxenopoides reuningi* (Anura, Pipidae), *S. Afr. Mus. Ann.*, *73*(2), 1–36.
- Farley, K. A. R. A. Wolf, and L. T. Silver (1996), The effects of long alpha-stopping distances on (U-Th)/He ages, *Geochim. Cosmochim. Acta*, *60*(21), 4223–4229, doi:10.1016/S0016-7037(96)00193-7.
- Farley, K. A. D. L. Shuster, and R. A. Ketcham (2011), U and Th zonation in apatite observed by laser ablation ICPMS, and implications for the (U-Th)/He system, *Geochim. Cosmochim. Acta*, *75*(16), 4515–4530, doi:10.1016/j.gca.2011.05.020.
- Fitzgerald, P. G. S. L. Baldwin, L. E. Webb, and P. B. O'Sullivan (2006), Interpretation of (U-Th)/He single grain ages from slowly cooled crustal terranes: A case study from the Transantarctic Mountains of southern Victoria Land, *Chem. Geol.*, *225*(1), 91–120, doi:10.1016/j.chemgeo.2005.09.001.
- Flament, N. M. Gurnis, S. Williams, M. Seton, J. Skogseid, C. Heine, and R. D. Müller (2014), Topographic asymmetry of the South Atlantic from global models of mantle flow and lithospheric stretching, *Earth Planet. Sci. Lett.*, *387*, 107–119, doi:10.1016/j.epsl.2013.11.017.
- Flowers, R. M. and S. A. Kelley (2011), Interpreting data dispersion and—inverted dates in apatite (U-Th)/He and fission-track datasets: An example from the US midcontinent, *Geochim. Cosmochim. Acta*, *75*(18), 5169–5186, doi:10.1016/j.gca.2011.06.016.
- Flowers, R. M. and B. Schoene (2010), (U-Th)/He thermochronometry constraints on unroofing of the eastern Kaapvaal craton and significance for uplift of the southern African Plateau, *Geology*, *38*(9), 827–830, doi:10.1130/g30980.1.
- Flowers, R. M. R. A. Ketcham, D. L. Shuster, and K. A. Farley (2009), Apatite (U-Th)/He thermochronometry using a radiation damage accumulation and annealing model, *Geochim. Cosmochim. Acta*, *73*(8), 2347–2365.
- Forte, A. M. R. Moucha, N. A. Simmons, S. P. Grand, and J. X. Mitrovica (2010), Deep-mantle contributions to the surface dynamics of the North American continent, *Tectonophysics*, *481*(1), 3–15, doi:10.1016/j.tecto.2009.06.010.
- François, T. E. Burov, B. Meyer, and P. Agard (2013), Surface topography as key constraint on thermo-rheological structure of stable cratons, *Tectonophysics*, *602*, 106–123, doi:10.1016/j.tecto.2012.10.009.
- Franco-Magalhaes, A. O. B. M. A. A. Cuglieri, P. C. Hackspacher, and A. R. Saad (2014), Long-term landscape evolution and post-rift reactivation in the southeastern Brazilian passive continental margin: Taubaté basin, *Int. J. Earth Sci.*, *103*(2), 441–453, doi:10.1007/s00531-013-0967-4.
- Frimmel, H. E. M. A. Basei, V. X. Correa, and N. Mbangula (2013), A new lithostratigraphic subdivision and geodynamic model for the Pan-African western Saldania Belt, South Africa, *Precambrian Res.*, *231*, 218–235, doi:10.1016/j.precamres.2013.03.014.
- Gaina, C. T. H. Torsvik, D. J. van Hinsbergen, S. Medvedev, S. C. Werner, and C. Labails (2013), The African Plate: A history of oceanic crust accretion and subduction since the Jurassic, *Tectonophysics*, *604*, 4–25, doi:10.1016/j.tecto.2013.05.037.
- Galbraith, R. F. (2010), *Statistics for Fission Track Analysis*, 240 pp., Chapman and Hall/CRC, Florida.
- Galbraith, R. F. and P. F. Green (1990), Estimating the component ages in a finite mixture, *Int. J. Radiat. Appl. Instrum., Part D*, *17*(3), 197–206, doi:10.1016/1359-0189(90)90035-v.
- Gallagher, K. (1995), Evolving temperature histories from apatite fission-track data, *Earth Planet. Sci. Lett.*, *136*(3), 421–435, doi:10.1016/0012-821x(95)00197-k.
- Gallagher, K. (2012), Transdimensional inverse thermal history modeling for quantitative thermochronology, *J. Geophys. Res.*, *117*, B02408, doi:10.1029/2011JB008825.
- Gallagher, K. and R. Brown (1997), The onshore record of passive margin evolution, *J. Geol. Soc.*, *154*(3), 451–457, doi:10.1144/gsjgs.154.3.0451.
- Gallagher, K. and R. Brown (1999), Denudation and uplift at passive margins: The record on the Atlantic Margin of southern Africa, *Philos. Trans. R. Soc. London A*, *357*(1753), 835–859, doi:10.1098/rsta.1999.0354.
- Gallagher, K. K. Charvin, S. Nielsen, M. Sambridge, and J. Stephenson (2009), Markov chain Monte Carlo (MCMC) sampling methods to determine optimal models, model resolution and model choice for Earth Science problems, *Mar. Pet. Geol.*, *26*(4), 525–535, doi:10.1016/j.marpetgeo.2009.01.003.
- Gautheron, C. L. Tassan-Got, J. Barbarand, and M. Pagel (2009), Effect of alpha-damage annealing on apatite (U-Th)/He thermochronology, *Chem. Geol.*, *266*(3), 157–170, doi:10.1016/j.chemgeo.2009.06.001.
- Gautheron, C. L. Tassan-Got, R. A. Ketcham, and K. J. Dobson (2012), Accounting for long alpha-particle stopping distances in (U-Th-Sm)/He geochronology: 3D modeling of diffusion, zoning, implantation, and abrasion, *Geochim. Cosmochim. Acta*, *96*, 44–56, doi:10.1016/j.gca.2012.08.016.
- Gautheron, C. J. Barbarand, R. A. Ketcham, L. Tassan-Got, P. van der Beek, M. Pagel, R. Pinna-Jamme, F. Couffignal, and M. Fialin (2013), Chemical influence on  $\alpha$ -recoil damage annealing in apatite: Implications for (U-Th)/He dating, *Chem. Geol.*, *351*, 257–267, doi:10.1016/j.chemgeo.2013.05.027.
- Gilchrist, A. R. and M. A. Summerfield (1990), Differential denudation and flexural isostasy in formation of rifted-margin upwarps, *Nature*, *346*, 739–742, doi:10.1038/346739a0.

- Gilchrist, A. R. H. Kooi, and C. Beaumont (1994), Post-Gondwana geomorphic evolution of southwestern Africa: Implications for the controls on landscape development from observations and numerical experiments, *J. Geophys. Res.*, 99, 12,211–12,228, doi:10.1029/94JB00046.
- Gilks, W. R. (2005), *Markov Chain Monte Carlo*, John Wiley, doi:10.1002/0470011815.b2a14021.
- Goudie, A. S. (2005), The drainage of Africa since the Cretaceous, *Geomorphology*, 67(3), 437–456, doi:10.1016/j.geomorph.2004.11.008.
- Granot, R. and J. Dymet (2015), The Cretaceous opening of the South Atlantic Ocean, *Earth Planet. Sci. Lett.*, 414, 156–163, doi:10.1016/j.epsl.2015.01.015.
- Green, P. F. (1986), On the thermo-tectonic evolution of Northern England: Evidence from fission track analysis, *Geol. Mag.*, 123(5), 493–506, doi:10.1017/s0016756800035081.
- Green, P. F. and I. R. Duddy (2006), Interpretation of apatite (U–Th)/He ages and fission track ages from cratons, *Earth Planet. Sci. Lett.*, 244(3), 541–547, doi:10.1016/j.epsl.2006.02.024.
- Green, P. F. K. Lidmar-Bergström, P. Japsen, J. M. Bonow, and J. A. Chalmers (2013), *Stratigraphic Landscape Analysis, Thermochronology and the Episodic Development of Elevated, Passive Continental Margins*, Geol. Surv. of Den. and Greenl., Dan. Minist. of Clim., Energy and Build, Copenhagen.
- Green, P. F. I. R. Duddy, P. Japsen, J. M. Bonow, and J. A. Malan (2015), Post-breakup burial and exhumation of the southern margin of Africa, *Basin Res.*, doi:10.1111/bre.12167.
- Gresse, P. G. and G. J. B. Germs (1993), The Nama foreland basin: Sedimentation, major unconformity bounded sequences and multisided active margin advance, *Precambrian Res.*, 63(3), 247–272, doi:10.1016/0301-9268(93)90036-2.
- Gresse, P. G. M. W. Von Veh, and H. E. Frimmel (2006), Namibian (Neoproterozoic) to early Cambrian successions, in *The Geology of South Africa*, pp. 395–420, Geol. Soc. of S. Afr., Johannesburg, South Africa.
- Griffin, W. L. S. Y. O'Reilly, L. M. Natapov, and C. G. Ryan (2003), The evolution of lithospheric mantle beneath the Kalahari Craton and its margins, *Lithos*, 71(2), 215–241, doi:10.1016/j.lithos.2003.07.006.
- Greenewald, P. B. G. H. Grantham, and M. K. Watkeys (1991), Geological evidence for a Proterozoic to Mesozoic link between southeastern Africa and Dronning Maud Land, Antarctica, *J. Geol. Soc.*, 148(6), 1115–1123, doi:10.1144/gsjgs.148.6.1115.
- Guillocheau, F. D. Rouby, C. Robin, C. Helm, N. Rolland, C. Le Carlier de Veslud, and J. Braun (2012), Quantification and causes of the terrigenous sediment budget at the scale of a continental margin: A new method applied to the Namibia–South Africa margin, *Basin Res.*, 24(1), 3–30, doi:10.1111/j.1365-2117.2011.00511.x.
- Guillou-Frottier, L. E. Burov, S. Cloetingh, E. Le Goff, Y. Deschamps, B. Huet, and V. Bouchot (2012), Plume-induced dynamic instabilities near cratonic blocks: Implications for P–T paths and metallogeny, *Global Planet. Change*, 90, 37–50, doi:10.1016/j.gloplacha.2011.10.007.
- Guiraud, R. and J. C. Maurin (1992), Early Cretaceous rifts of Western and Central Africa: An overview, *Tectonophysics*, 213(1), 153–168, doi:10.1016/0040-1951(92)90256-6.
- Gunnell, Y. K. Gallagher, A. Carter, M. Widdowson, and A. J. Hurford (2003), Denudation history of the continental margin of western peninsular India since the early Mesozoic—Reconciling apatite fission-track data with geomorphology, *Earth Planet. Sci. Lett.*, 215(1), 187–201, doi:10.1016/s0012-821x(03)00380-7.
- Gurnis, M., J. X. Mitrovica, J. Ritsema, and H. J. van Heijst (2000), Constraining mantle density structure using geological evidence of surface uplift rates: The case of the African superplume, *Geophys. Geosyst.*, 1(7), 1020, doi:10.1029/1999GC000035.
- Gutzmer, J. and N. J. Beukes (2000), Asbestiform manjiroite and todorokite from the Kalahari manganese field, South Africa, *S. Afr. J. Geol.*, 103(3–4), 163–174, doi:10.2113/1030163.
- Hansen, K. and P. W. Reiners (2006), Low temperature thermochronology of the southern East Greenland continental margin: Evidence from apatite (U–Th)/He and fission track analysis and implications for intermethod calibration, *Lithos*, 92(1), 117–136, doi:10.1016/j.lithos.2006.03.039.
- Hanson, E. K. J. M. Moore, E. M. Bordy, J. S. Marsh, G. Howarth, and J. V. A. Robey (2009), Cretaceous erosion in central South Africa: Evidence from upper-crustal xenoliths in kimberlite diatremes, *S. Afr. J. Geol.*, 112, 125–140, doi:10.2113/gssaig.112.2.125.
- Hartley, R. A. B. Watts, and J. D. Fairhead (1996), Isostasy of Africa, *Earth Planet. Sci. Lett.*, 137(1), 1–18, doi:10.1016/0012-821x(95)00185-f.
- Hartwig, A. Z. Anka, and R. di Primio (2012), Evidence of a widespread paleo-pockmarked field in the Orange Basin: An indication of an early Eocene massive fluid escape event offshore South Africa, *Mar. Geol.*, 332, 222–234, doi:10.1016/j.margeo.2012.07.012.
- Haughton, S. H. (1931), On a collection of fossil frogs from the clays at Banke, *Trans. R. Soc. S. Afr.*, 19(3), 233–249, doi:10.1080/00359193109518836.
- Heine, C. J. Zoethout, and R. D. Müller (2013), Kinematics of the South Atlantic rift, *Solid Earth*, 4, 215–253, doi:10.5194/se-4-215-2013.
- Hendriks, B. W. H. and T. F. Redfield (2005), Apatite fission track and (U–Th)/He data from Fennoscandia: An example of underestimation of fission track annealing in apatite, *Earth Planet. Sci. Lett.*, 236(1), 443–458, doi:10.1016/j.epsl.2005.05.027.
- Hirsch, K. K. M. Scheck-Wenderoth, J. D. van Wees, G. Kuhlmann, and D. A. Paton (2010), Tectonic subsidence history and thermal evolution of the Orange Basin, *Mar. Pet. Geol.*, 27(3), 565–584, doi:10.1016/j.marpetgeo.2009.06.009.
- Holford, S. P. A. K. Tuitt, R. R. Hillis, P. F. Green, M. S. Stoker, I. R. Duddy, M. Sandiford, and D. R. Tassone (2014), Cenozoic deformation in the Otway Basin, southern Australian margin: Implications for the origin and nature of post-breakup compression at rifted margins, *Basin Res.*, 26(1), 10–37, doi:10.1111/bre.12035.
- House, M. A. B. P. Wernicke, K. A. Farley, and T. A. Dumitru (1997), Cenozoic thermal evolution of the central Sierra Nevada, California, from (UTh)/He thermochronometry, *Earth Planet. Sci. Lett.*, 151(3), 167–179, doi:10.1016/s0012-821x(97)81846-8.
- Huismans, R. S. and C. Beaumont (2014), Rifted continental margins: The case for depth-dependent extension, *Earth Planet. Sci. Lett.*, 407, 148–162, doi:10.1016/j.epsl.2014.09.032.
- Hurford, A. J. and P. F. Green (1982), A users' guide to fission track dating calibration, *Earth Planet. Sci. Lett.*, 59(2), 343–354, doi:10.1016/0012-821x(82)90136-4.
- Jackson, M. C. Cramez, and J. M. Fonck (2000), Role of subaerial volcanic rocks and mantle plumes in creation of South Atlantic margins: Implications for salt tectonics and source rocks, *Mar. Pet. Geol.*, 17(4), 477–498, doi:10.1016/s0264-8172(00)00006-4.
- Jacobs, J. R. J. Thomas, and K. Weber (1993), Accretion and indentation tectonics at the southern edge of the Kaapvaal craton during the Kibaran (Grenville) orogeny, *Geology*, 21(3), 203–206, doi:10.1130/0091-7613(1993)021<0203:aaitat>2.3.co;2.
- Janney, P. E. S. B. Shirey, R. W. Carlson, D. G. Pearson, D. R. Bell, A. P. Le Roex, A. Ishikawa, P. H. Nixon, and F. R. Boyd (2010), Age, composition and thermal characteristics of South African off-craton mantle lithosphere: Evidence for a multi-stage history, *J. Petrol.*, doi:10.1093/petrology/egq041.
- Jelsma, H. W. Barnett, S. Richards, and G. Lister (2009), Tectonic setting of kimberlites, *Lithos*, 112, 155–165, doi:10.1016/j.lithos.2009.06.030.
- Johnson, M. R. C. R. Anhaeusser, and R. J. Thomas (2006), *The Geology of South Africa*, Geol. Soc. of S. Afr., Pretoria, South Africa.
- Jones, E. J. W. S. C. Cande, and F. Spathopoulos (1995), Evolution of a major oceanographic pathway: The equatorial Atlantic, *Geol. Soc. London Spec. Publ.*, 90(1), 199–213, doi:10.1144/gsl.sp.1995.090.01.12.
- Jones, M. Q. W. (1987), Heat flow and heat production in the Namaqua mobile belt, South Africa, *J. Geophys. Res.*, 92, 6273–6289, doi:10.1029/JB092iB07p06273.
- Jourdan, F. G. Féraud, H. Bertrand, A. B. Kampunzu, G. Tshoso, M. K. Watkeys, and B. Le Gall (2005), Karoo large igneous province: Brevity, origin, and relation to mass extinction questioned by new <sup>40</sup>Ar/<sup>39</sup>Ar age data, *Geology*, 33(9), 745–748, doi:10.1130/g21632.1.



- Jourdan, F. G. Féraud, H. Bertrand, and M. K. Watkeys (2007), From flood basalts to the inception of oceanization: Example from the 40Ar/39Ar high-resolution picture of the Karoo large igneous province, *Geochim. Geophys. Geosyst.*, 8, Q02002, doi:10.1029/2006GC001392.
- Jungslager, E. H. (1999), Petroleum habitats of the Atlantic margin of South Africa, *Geol. Soc. London Spec. Publ.*, 153(1), 153–168, doi:10.1144/gsl.sp.1999.153.01.10.
- Karl, M. U. A. Glasmacher, S. Kollenz, A. O. Franco-Magalhaes, D. F. Stockli, and P. C. Hackspacher (2013), Evolution of the South Atlantic passive continental margin in southern Brazil derived from zircon and apatite (U–Th–Sm)/He and fission-track data, *Tectonophysics*, 604, 224–244, doi:10.1016/j.tecto.2013.06.017.
- Kennett, B. L. N. and G. Iaffaldano (2013), Role of lithosphere in intra-continental deformation: Central Australia, *Gondwana Res.*, 24(3), 958–968, doi:10.1016/j.gr.2012.10.010.
- Ketcham, R. A. (2005), The role of crystallographic angle in characterizing and modeling apatite fission-track length data, *Radiat. Meas.*, 39(6), 595–601, doi:10.1016/j.radmeas.2004.07.008.
- Ketcham, R. A. A. Carter, R. A. Donelick, J. Barbarand, and A. J. Hurford (2007), Improved modeling of fission-track annealing in apatite, *Am. Mineral.*, 92(5–6), 799–810, doi:10.2138/am.2007.2281.
- Kooi, H. and C. Beaumont (1994), Escarpment evolution on high-elevation rifted margins: Insights derived from a surface processes model that combines diffusion, advection, and reaction, *J. Geophys. Res.*, 99, 12,191–12,209, doi:10.1029/94JB00047.
- Koopmann, H. D. Franke, B. Schreckenberger, H. Schulz, A. Hartwig, H. Stollhofen, and R. di Primio (2014), Segmentation and volcano-tectonic characteristics along the SW African continental margin, South Atlantic, as derived from multichannel seismic and potential field data, *Mar. Pet. Geol.*, 50, 22–39, doi:10.1016/j.marpetgeo.2013.10.016.
- Koptev, A. E. Calais, E. Burov, S. Leroy, and T. Gerya (2015), Dual continental rift systems generated by plume-lithosphere interaction, *Nat. Geosci.*, 8(5), 388–392, doi:10.1038/ngeo2401.
- Kounov, A. S. Niedermann, M. J. de Wit, G. Viola, M. Andreoli, and J. Erzinger (2007), Present denudation rates at selected sections of the South African escarpment and the elevated continental interior based on cosmogenic <sup>3</sup>He and <sup>21</sup>Ne, *S. Afr. J. Geol.*, 110(2–3), 235–248, doi:10.2113/gssajg.110.2-3.235.
- Kounov, A. G. Viola, M. De Wit, and M. A. G. Andreoli (2009), Denudation along the Atlantic passive margin: New insights from apatite fission-track analysis on the western coast of South Africa, *Geol. Soc. London Spec. Publ.*, 324(1), 287–306, doi:10.1144/sp324.19.
- Kounov, A. G. Viola, I. Dunkl, and H. E. Frimmel (2013), Southern African perspectives on the long-term morpho-tectonic evolution of cratonic interiors, *Tectonophysics*, 601, 177–191, doi:10.1016/j.tecto.2013.05.009.
- Kounov, A. S. Niedermann, M. J. de Wit, A. T. Codilean, G. Viola, M. Andreoli, and M. Christl (2015), Cosmogenic <sup>21</sup>Ne and <sup>10</sup>Be reveal a more than 2 ma alluvial fan flanking the Cape Mountains, South Africa, *S. Afr. J. Geol.*, 118(2), 129–144, doi:10.2113/gssajg.118.2.129.
- Ksienzyk, A. K. I. Dunkl, J. Jacobs, H. Fossen, and F. Kohlmann (2014), From orogen to passive margin: Constraints from fission track and (U–Th)/He analyses on Mesozoic uplift and fault reactivation in SW Norway, *Geol. Soc. London Spec. Publ.*, 390, 679–702, doi:10.1144/sp390.27.
- Kuhlmann, G. S. Adams, C. Campher, D. van der Spuy, R. di Primio, and B. Horsfield (2010), Passive margin evolution and its controls on natural gas leakage in the southern Orange Basin, blocks 3/4, offshore South Africa, *Mar. Pet. Geol.*, 27(4), 973–992, doi:10.1016/j.marpetgeo.2010.01.010.
- Kuszniir, N. J., G. Marsden, and S. S. Egan (1991), A flexural-cantilever simple-shear/pure shear model of continental lithosphere extension: Applications to the Jeanne d'Arc basin, Grand Banks and Viking Graben, North sea, in *The Geometry of Normal Faults, Spec. Publ.*, vol. 56, edited by A. M. Roberts, G. Yielding, and B. Freeman, pp. 41–60, Geol. Soc., London, doi:10.1144/gsl.sp.1991.056.01.04.
- Labails, C. T. H. Torsvik, C. Gaina, and R. M. Cocks (2009), Global plate polygons 2009. SPLates Model (version 2.0), Tech. Rep. 2009.047, NGU, Trondheim. [Available at <http://www.ngu.no/en-gb/>]
- Leprêtre, R. Y. Missenard, J. Barbarand, C. Gautheron, O. Saddiqi, and R. Pinna-Jamme (2015), Post-rift history of the eastern Central Atlantic passive margin: Insights from the Saharan region of South Morocco, *J. Geophys. Res. Solid Earth*, 120, 4645–4666, doi:10.1002/2014JB011549.
- Lister, G. S. M. A. Etheridge, and P. A. Symonds (1991), Detachment models for the formation of passive continental margins, *Tectonics*, 10, 1038–1064, doi:10.1029/90TC01007.
- Lithgow-Bertelloni, C. and P. G. Silver (1998), Dynamic topography, plate driving forces and the African superswell, *Nature*, 395(6699), 269–272, doi:10.1038/26212.
- Loule, J. P. and L. Pospisil (2013), Geophysical evidence of Cretaceous volcanics in Logone Birni Basin (Northern Cameroon), Central Africa, and consequences for the West and Central African Rift System, *Tectonophysics*, 583, 88–100, doi:10.1016/j.tecto.2012.10.021.
- Lundin, E. R. and A. G. Doré (2011), Hyperextension, serpentinization, and weakening: A new paradigm for rifted margin compressional deformation, *Geology*, 39(4), 347–350, doi:10.1130/g31499.1.
- Macey, P. H. P. Siegfried, H. Minnaar, J. Almond, and P. M. W. Botha (2011), *The Geology of the Loeriesfontein Area. Explanation of 1:250,000-Scale Loeriesfontein*, Council for Geosci., South Africa.
- Marais, J. A. H. A. L. D. Agenbacht, M. Prinsloo, and W. A. Basson (2001), *The Geology of the Springbok Area. Explanation of 1:250 000-Scale 2916 Loeriesfontein*, Council for Geosci., South Africa.
- Masini, E. G. Manatschal, and G. Mohn (2013), The Alpine Tethys rifted margins: Reconciling old and new ideas to understand the stratigraphic architecture of magma-poor rifted margins, *Sedimentology*, 60(1), 174–196, doi:10.1111/sed.12017.
- Mbongo-Djimbi, D. C. Gautheron, J. Roques, L. Tassan-Got, C. Gerin, and E. Simoni (2015), Impact of apatite chemical composition on (U–Th)/He thermochronometry: An atomistic point of view, *Geochim. Cosmochim. Acta*, 167, 162–176, doi:10.1016/j.gca.2015.06.017.
- McMillan, I. K. (2003), Foraminiferally defined biostratigraphic episodes and sedimentation pattern of the Cretaceous drift succession (Early Barremian to Late Maastrichtian) in seven basins on the South African and southern Namibian continental margin, *S. Afr. J. Sci.*, 99(11 & 12), 537–576.
- Meesters, A. G. C. A. and T. J. Dunai (2002a), Solving the production–diffusion equation for finite diffusion domains of various shapes: Part I. Implications for low-temperature (U–Th)/He thermochronology, *Chem. Geol.*, 186(3), 333–344, doi:10.1016/s0009-2541(01)00422-3.
- Meesters, A. G. C. A. and T. J. Dunai (2002b), Solving the production–diffusion equation for finite diffusion domains of various shapes: Part II. Application to cases with  $\alpha$ -ejection and nonhomogeneous distribution of the source, *Chem. Geol.*, 186(3), 347–363, doi:10.1016/s0009-2541(02)00073-6.
- Molnar, P. P. C. England, and C. H. Jones (2015), Mantle dynamics, isostasy, and the support of high terrain, *J. Geophys. Res. Solid Earth*, 120, 1932–1957, doi:10.1002/2014JB011724.
- Moore, A. T. Blenkinsop, and F. W. Cotterill (2008), Controls on post-Gondwana alkaline volcanism in Southern Africa, *Earth Planet. Sci. Lett.*, 268(1), 151–164, doi:10.1016/j.epsl.2008.01.007.
- Moore, A. E. and W. J. Verwoerd (1985), The olivine melilitite–kimberlite–carbonatite suite of Namaqualand and Bushmanland, South Africa, *S. Afr. J. Geol.*, 88(2), 281–294.
- Moucha, R. and A. M. Forte (2011), Changes in African topography driven by mantle convection, *Nat. Geosci.*, 4(10), 707–712, doi:10.1038/ngeo1235.



- Moucha, R. A. M. Forte, J. X. Mitrovica, D. B. Rowley, S. Quéré, N. A. Simmons, and S. P. Grand (2008), Dynamic topography and long-term sea-level variations: There is no such thing as a stable continental platform, *Earth Planet. Sci. Lett.*, *271*(1), 101–108, doi:10.1016/j.epsl.2008.03.056.
- Moulin, M. D. Aslanian, and P. Unternehr (2010), A new starting point for the South and Equatorial Atlantic Ocean, *Earth Sci. Rev.*, *98*(1), 1–37, doi:10.1016/j.earscirev.2009.08.001.
- Moulin, M. F. Fluteau, V. Courtillot, J. Marsh, G. Delpech, X. Quidelleur, M. Gerard, and A. E. Jay (2011), An attempt to constrain the age, duration, and eruptive history of the Karoo flood basalt: Naude's Nek section (South Africa), *J. Geophys. Res.*, *116*, B07403, doi:10.1029/2011JB008210.
- Müller, R. D. M. Sclorlias, C. Gaina, and W. R. Roest (2008), Age, spreading rates, and spreading asymmetry of the world's ocean crust, *Geochim. Geophys. Geosyst.*, *9*, Q04006, doi:10.1029/2007GC001743.
- Muntingh, A. and L. F. Brown Jr. (1993), Recent applications of siliciclastic sequence stratigraphy, sequence stratigraphy of petroleum plays, post-rift cretaceous rocks (Lower Aptian to Upper Maastrichtian), Orange Basin, Western Offshore, South Africa, in *Siliciclastic Sequence Stratigraphy: Recent Developments and Applications*, edited by P. Weimer and H. Posamentier, chap. 4, American Association of Petroleum Geologists, doi:10.1306/M58581.
- Naliboff, J. and S. J. Buiter (2015), Rift reactivation and migration during multiphase extension, *Earth Planet. Sci. Lett.*, *421*, 58–67, doi:10.1016/j.epsl.2015.03.050.
- Nürnberg, D. and R. D. Müller (1991), The tectonic evolution of the South Atlantic from Late Jurassic to present, *Tectonophysics*, *191*(1), 27–53, doi:10.1016/0040-1951(91)90231-g.
- Nyblade, A. A., and N. H. Sleep (2003), Long lasting epeirogenic uplift from mantle plumes and the origin of the Southern African Plateau, *Geochim. Geophys. Geosyst.*, *4*(12), 1105, doi:10.1029/2003GC000573.
- Ollier, C. D. and C. F. Pain (1997), Equating the basal unconformity with the palaeoplain: A model for passive margins, *Geomorphology*, *19*(1), 1–15, doi:10.1016/S0169-555X(96)00048-7.
- Partridge, T. C. and R. R. Maud (1987), Geomorphic evolution of southern Africa since the Mesozoic, *S. Afr. J. Geol.*, *90*(2), 179–208.
- Paton, D. (2012), Post-rift deformation of the North East and South Atlantic margins: Are "Passive Margins" really passive?, in *Tectonics of Sedimentary Basins: Recent Advances*, pp. 249–269, West Sussex, U. K., doi:10.1002/9781444347166.ch12.
- Paton, D. A. R. Di Primio, G. Kuhlmann, D. Van Der Spuy, and B. Horsfield (2007), Insights into the petroleum system evolution of the southern Orange Basin, South Africa, *S. Afr. J. Geol.*, *110*(2–3), 261–274, doi:10.2113/gssajg.110.2-3.261.
- Paton, D. A. D. van der Spuy, R. di Primio, and B. Horsfield (2008), Tectonically induced adjustment of passive-margin accommodation space; influence on the hydrocarbon potential of the Orange Basin, South Africa, *AAPG Bull.*, *92*(5), 589–609, doi:10.1306/12280707023.
- Paul, J. D. G. G. Roberts, and N. White (2014), The African landscape through space and time, *Tectonics*, *33*, 898–935, doi:10.1002/2013TC003479.
- Pérez-Díaz, L. and G. Eagles (2014), Constraining South Atlantic growth with seafloor spreading data, *Tectonics*, *33*, 1848–1873, doi:10.1002/2014TC003644.
- Pérez-Gussinyé, M. A. R. Lowry, and A. B. Watts (2007), Effective elastic thickness of South America and its implications for intracontinental deformation, *Geochim. Geophys. Geosyst.*, *8*, Q05009, doi:10.1029/2006GC001511.
- Péron-Pinvidic, G. and G. Manatschal (2009), The final rifting evolution at deep magma-poor passive margins from Iberia-Newfoundland: A new point of view, *Int. J. Earth Sci.*, *98*(7), 1581–1597, doi:10.1007/s00531-008-0337-9.
- Péron-Pinvidic, G. G. Manatschal, and P. T. Osmundsen (2013), Structural comparison of archetypal Atlantic rifted margins: A review of observations and concepts, *Mar. Pet. Geol.*, *43*, 21–47, doi:10.1016/j.marpetgeo.2013.02.002.
- Persano, C. F. M. Stuart, P. Bishop, and D. N. Barfod (2002), Apatite (U–Th)/He age constraints on the development of the Great Escarpment on the southeastern Australian passive margin, *Earth Planet. Sci. Lett.*, *200*(1), 79–90, doi:10.1016/S0012-821X(02)00614-3.
- Persano, C. F. M. Stuart, P. Bishop, and T. J. Dempster (2005), Deciphering continental breakup in eastern Australia using low-temperature thermochronometers, *J. Geophys. Res.*, *110*, B12405, doi:10.1029/2004JB003325.
- Phillips, D. G. B. Kiviets, M. G. Biddulph, and M. K. Madav (2000), Cenozoic volcanism, in *The Cenozoic of Southern Africa*, edited by T. C. Partridge and R. R. Maud, pp. 182–197, Oxford Univ. Press, Oxford, U. K.
- Pickford, M. and B. Senut (1999), *Geology and Palaeobiology of the Namib Desert Southwest Africa, Mem.*, vol. 18, 155 pp., Geol. Surv. of Namibia, Windhoek, Namibia.
- Raab, M. J. R. W. Brown, K. Gallagher, A. Carter, and K. Weber (2002), Late Cretaceous reactivation of major crustal shear zones in northern Namibia: Constraints from apatite fission track analysis, *Tectonophysics*, *349*(1), 75–92, doi:10.1016/S0040-1951(02)00047-1.
- Redfield, T. F. and P. T. Osmundsen (2013), The long-term topographic response of a continent adjacent to a hyperextended margin: A case study from Scandinavia, *Geol. Soc. Am. Bull.*, *125*(1–2), 184–200, doi:10.1130/b30691.1.
- Redfield, T. F. P. T. Osmundsen, and B. W. H. Hendriks (2005), The role of fault reactivation and growth in the uplift of western Fennoscandia, *J. Geol. Soc.*, *162*(6), 1013–1030, doi:10.1144/0016-764904-149.
- Reid, D. L. (1990), The Cape Peninsula dolerite dyke swarm, South Africa, in *Mafic Dikes and Emplacement Mechanisms*, edited by A. J. Parker, P. C. Rickwood, and D. H. Tucker, pp. 325–334, Balkema, Rotterdam, Netherlands.
- Reid, D. L. and D. C. Rex (1994), Cretaceous dykes associated with the opening of the South Atlantic: The Mehlberg Dyke, northern Richtersveld, *S. Afr. J. Geol.*, *97*(2), 135–145.
- Reid, D. L. A. F. Cooper, D. C. Rex, and R. E. Harmer (1990), Timing of post-Karoo alkaline volcanism in southern Namibia, *Geol. Mag.*, *127*(5), 427–433, doi:10.1017/S001675680001517x.
- Reid, D. L. A. J. Erlank, and D. C. Rex (1991), Age and correlation of the False Bay dolerite dyke swarm, south-western Cape, Cape Province, *S. Afr. J. Geol.*, *94*(2–3), 155–158, doi:10.2113/gssajg.114.3-4.335.
- Reiners, P. W. and K. A. Farley (2001), Influence of crystal size on apatite (U–Th)/He thermochronology: An example from the Bighorn Mountains, Wyoming, *Earth Planet. Sci. Lett.*, *188*(3), 413–420, doi:10.1016/S0012-821X(01)00341-7.
- Reston, T. J. (2005), Polyphase faulting during the development of the west Galicia rifted margin, *Earth Planet. Sci. Lett.*, *237*(3), 561–576, doi:10.1016/j.epsl.2005.06.019.
- Roberts, D. L. G. A. Botha, R. R. Maud, and J. Pether (2006), Coastal cenozoic deposits, in *The Geology of South Africa*, edited by M. R. Johnson, C. R. Anhaeusser, and R. J. Thomas, pp. 605–628, Geol. Soc. of S. Afr, Pretoria, South Africa.
- Roberts, G. G. and N. White (2010), Estimating uplift rate histories from river profiles using African examples, *J. Geophys. Res.*, *115*, B02406, doi:10.1029/2009JB006692.
- Rouby, D. S. Bonnet, F. Guillocheau, K. Gallagher, C. Robin, F. Biancotto, O. Dauteuil, and J. Braun (2009), Sediment supply to the Orange sedimentary system over the last 150 My: An evaluation from sedimentation/denudation balance, *Mar. Pet. Geol.*, *26*(6), 782–794, doi:10.1016/j.marpetgeo.2008.08.004.
- Rudge, J. F. G. G. Roberts, N. White, and C. N. Richardson (2015), Uplift histories of Africa and Australia from linear inverse modeling of drainage inventories, *J. Geophys. Res. Earth Surf.*, *120*, 894–914, doi:10.1002/2014JF003297.

- Rust, D. J. and M. A. Summerfield (1990), Isopach and borehole data as indicators of rifted margin evolution in southwestern Africa, *Mar. Pet. Geol.*, 7(3), 277–287, doi:10.1016/0264-8172(90)90005-2.
- Saintot, A. M. B. Stephens, G. Viola, and Ø. Nordgulen (2011), Brittle tectonic evolution and paleostress field reconstruction in the southwestern part of the Fennoscandian Shield, Forsmark, Sweden, *Tectonics*, 30, TC4002, doi:10.1029/2010TC002781.
- Salomon, E. D. Koehn, C. Passchier, P. C. Hackspacher, and U. A. Glasmacher (2014), Contrasting stress fields on correlating margins of the South Atlantic, *Gondwana Res.*, 28(3), 1152–1167, doi:10.1016/j.jgr.2014.09.006.
- Salomon, E. D. Koehn, and C. Passchier (2015), Brittle reactivation of ductile shear zones in NW Namibia in relation to South Atlantic rifting, *Tectonics*, 34, 70–85, doi:10.1002/2014TC003728.
- Sambridge, M. K. Gallagher, A. Jackson, and P. Rickwood (2006), Trans-dimensional inverse problems, model comparison and the evidence, *Geophys. J. Int.*, 167(2), 528–542, doi:10.1111/j.1365-246x.2006.03155.x.
- Scharf, T. E. A. T. Codilean, M. de Wit, J. D. Jansen, and P. W. Kubik (2013), Strong rocks sustain ancient postorogenic topography in southern Africa, *Geology*, 41(3), 331–334, doi:10.1130/g33806.1.
- Scholtz, A. (1985), *The Palynology of the Upper Lacustrine Sediments of the Arnot Pipe, Banke, Namaqualand*, vol. 95, 109 pp., The S. Afr. Mus., Cape Town, South Africa.
- Senut, B. M. Pickford, and D. Wessels (1997), Panafrican distribution of lower Miocene Hominoidea, *C. R. Acad. Sci., Ser. IIA: Sci. Terre Planetes*, 325(9), 741–746, doi:10.1016/s1251-8050(97)89119-7.
- Séranne, M. and Z. Anka (2005), South Atlantic continental margins of Africa: A comparison of the tectonic vs climate interplay on the evolution of equatorial west Africa and SW Africa margins, *J. Afr. Earth Sci.*, 43(1), 283–300, doi:10.1016/j.jafrearsci.2005.07.010.
- Sibson, R. H. (1985), A note on fault reactivation, *J. Struct. Geol.*, 7(6), 751–754, doi:10.1016/0191-8141(85)90150-6.
- Sobel, E. R. and D. Seward (2010), Influence of etching conditions on apatite fission-track etch pit diameter, *Chem. Geol.*, 271(1), 59–69, doi:10.1016/j.chemgeo.2009.12.012.
- Spiegel, C. B. Kohn, D. Belton, Z. Berner, and A. Gleadow (2009), Apatite (U–Th–Sm)/He thermochronology of rapidly cooled samples: The effect of He implantation, *Earth Planet. Sci. Lett.*, 285(1), 105–114, doi:10.1016/j.epsl.2009.05.045.
- Stanley, J. R. R. M. Flowers, and D. R. Bell (2013), Kimberlite (U–Th)/He dating links surface erosion with lithospheric heating, thinning, and metasomatism in the southern African Plateau, *Geology*, 41(12), 1243–1246, doi:10.1130/g34797.1.
- Stanley, J. R. R. M. Flowers, and D. R. Bell (2015), Erosion patterns and mantle sources of topographic change across the southern African Plateau derived from the shallow and deep records of kimberlites, *Geochim. Geophys. Geosyst.*, 16, 3235–3256, doi:10.1002/2015GC005969.
- Stevenson, I. R. and I. K. McMillan (2004), Incised valley fill stratigraphy of the Upper Cretaceous succession, proximal Orange Basin, Atlantic margin of southern Africa, *J. Geol. Soc.*, 161(2), 185–208, doi:10.1144/0016-764902-003.
- Stockli, D. F. K. A. Farley, and T. A. Dumitru (2000), Calibration of the apatite (U–Th)/He thermochronometer on an exhumed fault block, White Mountains, California, *Geology*, 28(11), 983–986, doi:10.1130/0091-7613(2000)28<983:cotaht>2.0.co;2.
- Summerfield, M. A. (1985), Plate tectonics and landscape development on the African continent, in *Tectonic Geomorphology*, edited by M. Morisawa and J. T. Hack, pp. 27–51, Allan and Unwin, Boston, Mass.
- Svensen, H. F. Corfu, S. Polteau, Ø. Hammer, and S. Planke (2012), Rapid magma emplacement in the Karoo large igneous province, *Earth Planet. Sci. Lett.*, 325, 1–9, doi:10.1016/j.epsl.2012.01.015.
- Sykes, L. R. (1978), Intraplate seismicity, reactivation of preexisting zones of weakness, alkaline magmatism, and other tectonism postdating continental fragmentation, *Rev. Geophys.*, 16, 621–688, doi:10.1029/RG016i004p00621.
- Tankard, A. H. Welsink, P. Aukes, R. Newton, and E. Stettler (2009), Tectonic evolution of the Cape and Karoo basins of South Africa, *Mar. Pet. Geol.*, 26(8), 1379–1412, doi:10.1016/j.marpetgeo.2009.01.022.
- Tankard, A. J. S. C. Eriksson, D. R. Hunter, M. P. A. Jackson, D. K. Hobday, and W. E. L. Minter (1982), *Crustal Evolution of Southern Africa: 3.8 Billion Years of Earth History*, 523 pp., Springer, New York.
- Thomas, R. J. A. L. D. Agenbacht, D. H. Cornell, and J. M. Moore (1994), The Kibaran of southern Africa: Tectonic evolution and metallogeny, *Ore Geol. Rev.*, 9(2), 131–160, doi:10.1016/0169-1368(94)90025-6.
- Tinker, J. M. de Wit, and R. Brown (2008a), Mesozoic exhumation of the Southern Cape, South Africa, quantified using apatite fission track thermochronology, *Tectonophysics*, 455(1), 77–93, doi:10.1016/j.tecto.2007.10.009.
- Tinker, J. M. de Wit, and R. Brown (2008b), Linking source and sink: Evaluating the balance between onshore erosion and offshore sediment accumulation since Gondwana break-up, South Africa, *Tectonophysics*, 455(1), 94–103, doi:10.1016/j.tecto.2007.11.040.
- Torsvik, T. H. S. Rousse, C. Labails, and M. A. Smethurst (2009), A new scheme for the opening of the South Atlantic Ocean and the dissection of an Aptian salt basin, *Geophys. J. Int.*, 177(3), 1315–1333, doi:10.1111/j.1365-246x.2009.04137.x.
- Trumbull, R. B. D. L. Reid, C. de Beer, D. Van Acken, and R. L. Romer (2007), Magmatism and continental breakup at the west margin of southern Africa: A geochemical comparison of dolerite dikes from northwestern Namibia and the Western Cape, *S. Afr. J. Geol.*, 110(2–3), 477–502, doi:10.2113/gssajg.110.2-3.477.
- Turner, J. P. and G. A. Williams (2004), Sedimentary basin inversion and intra-plate shortening, *Earth Sci. Rev.*, 65(3), 277–304, doi:10.1016/j.earscirev.2003.10.002.
- van der Beek, P., M. A. Summerfield, J. Braun, R. W. Brown, and A. Fleming (2002), Modeling postbreakup landscape development and denudational history across the southeast African (Drakensberg Escarpment) margin, *J. Geophys. Res.*, 107(B12), 2351, doi:10.1029/2001JB000744.
- van der Merwe, R. and J. Fouche (1992), Inversion tectonics in the Bredasdorp basin, offshore South Africa, in *Inversion Tectonics of the Cape Fold Belt, Karoo and Cretaceous Basins of Southern Africa*, edited by M. J. de Wit and I. G. D. Ransome, pp. 49–59, A.A. Balkema, Cape Town, South Africa.
- van der Wateren, F. M. and T. J. Dunai (2001), Late Neogene passive margin denudation history—Cosmogenic isotope measurements from the central Namib desert, *Global Planet. Change*, 30(3), 271–307, doi:10.1016/s0921-8181(01)00104-7.
- Vermeesch, P. (2008), Three new ways to calculate average (U–Th)/He ages, *Chem. Geol.*, 249(3), 339–347, doi:10.1016/j.chemgeo.2008.01.027.
- Vermeesch, P. D. Seward, C. Latkoczy, M. Wipf, D. Günther, and H. Baur (2007),  $\alpha$ -emitting mineral inclusions in apatite, their effect on (U–Th)/He ages, and how to reduce it, *Geochim. Cosmochim. Acta*, 71(7), 1737–1746, doi:10.1016/j.gca.2006.09.020.
- Viola, G. M. Andreoli, Z. Ben-Avraham, I. Stengel, and M. Reshet (2005), Offshore mud volcanoes and onland faulting in southwestern Africa: Neotectonic implications and constraints on the regional stress field, *Earth Planet. Sci. Lett.*, 231(1), 147–160, doi:10.1016/j.epsl.2004.12.001.
- Viola, G. A. Kounov, M. A. G. Andreoli, and J. Mattila (2012), Brittle tectonic evolution along the western margin of South Africa: More than 500Myr of continued reactivation, *Tectonophysics*, 514, 93–114, doi:10.1016/j.tecto.2011.10.009.
- Visser, J. N. J. (1983), Submarine debris flow deposits from the Upper Carboniferous Dwyka tillite formation in the Kalahari Basin, South Africa, *Sedimentology*, 30(4), 511–523, doi:10.1111/j.1365-3091.1983.tb00689.x.
- Visser, J. N. J. (1987), The palaeogeography of part of southwestern Gondwana during the Permo–Carboniferous glaciation, *Palaeogeogr. Palaeoclimatol. Palaeoecol.*, 61, 205–219, doi:10.1016/0031-0182(87)90050-2.

- Visser, J. N. J. (1989), The Permo-Carboniferous Dwyka Formation of southern Africa: Deposition by a predominantly subpolar marine ice sheet, *Palaeogeogr. Palaeoclimatol. Palaeoecol.*, *70*(4), 377–391, doi:10.1016/0031-0182(89)90115-6.
- Visser, J. N. J. (1990), Glacial bedforms at the base of the Permo-Carboniferous Dwyka Formation along the western margin of the Karoo Basin, South Africa, *Sedimentology*, *37*(2), 231–245, doi:10.1111/j.1365-3091.1990.tb00957.x.
- Voordouw, R. J. and H. M. Rajesh (2012), Granitoids from the Margate Terrane and their implications for tectono-magmatic models of the Natal Metamorphic Province (South Africa), *S. Afr. J. Geol.*, *115*(1), 47–64, doi:10.2113/gssajg.115.1.47.
- Waters, D. J. (1989), Metamorphic evidence for the heating and cooling path of Namaqualand granulites, *Geol. Soc. London Spec. Publ.*, *43*(1), 357–363, doi:10.1144/gsl.sp.1989.043.01.31.
- Wernicke, B. and G. J. Axen (1988), On the role of isostasy in the evolution of normal fault systems, *Geology*, *16*(9), 848–851, doi:10.1130/0091-7613(1988)016<0848:otroii>2.3.co;2.
- White, S. H. Stollhofen, I. G. Stanistreet, and V. Lorenz (2009), Pleistocene to recent rejuvenation of the Hebron Fault, SW Namibia, *Geol. Soc. London Spec. Publ.*, *316*(1), 293–317, doi:10.1144/sp316.18.
- Wildman, M. R. Brown, R. Watkins, A. Carter, A. Gleadow, and M. Summerfield (2015), Post break-up tectonic inversion across the southwestern cape of South Africa: New insights from apatite and zircon fission track thermochronometry, *Tectonophysics*, *654*, 30–55, doi:10.1016/j.tecto.2015.04.012.
- Will, T. M. and H. E. Frimmel (2013), The influence of inherited structures on Dike emplacement during Gondwana breakup in Southwestern Africa, *J. Geol.*, *121*(5), 455–474, doi:10.1086/671398.
- Willett, S. D. (1999), Orogeny and orography: The effects of erosion on the structure of mountain belts, *J. Geophys. Res.*, *104*, 28,957–28,981, doi:10.1029/1999JB900248.
- Ziegler, P. A. and S. Cloetingh (2004), Dynamic processes controlling evolution of rifted basins, *Earth Sci. Rev.*, *64*(1), 1–50, doi:10.1016/s0012-8252(03)00041-2.